
Rotational Motions in Seismology, Theory and Application

Dissertation
der Fakultät Für Geowissenschaften
der Ludwig–Maximilians–Universität München

vorgelegt von
Wiwit Suryanto

am 21. Dezember 2006

Erstgutachter: Prof. Dr. Heiner Igel

Zweitgutachter: Prof. Dr. Ing. habil Ulrich Schreiber

Tag der mündlichen Prüfung: 21. Juni 2007

Contents

Zusammenfassung	xiii
Zusammenfassung	xiii
Summary	xviii
1. Introduction	1
1.1. Objectives	5
1.2. Structure of the Thesis	5
Nomenclature	1
2. Rotational ground motion	7
2.1. Rotation due to a double couple point source: analytical study	7
2.2. Rotational sensors	18
2.2.1. Parallel seismograph	18
2.2.2. Solid state sensor	20
2.2.3. Ring laser gyroscope	22
2.3. Applications	26
2.3.1. Geodesy, Earth rotation, polar motion	26
2.3.2. Geodynamics, static rotation	28
2.3.3. Seismology and earthquake engineering	28
2.4. Observations	30
2.5. Conclusion	30
3. Array experiment, deriving rotational rate from array data	32
3.1. Introduction	32

3.2. The array experiment	33
3.3. Data and data processing	36
3.4. Deriving rotation from seismic array data	40
3.5. Test on synthetic data	41
3.6. Various factors affecting the derivation of rotation rate	45
3.6.1. Synthetic noise	45
3.6.2. Real noise	48
3.6.3. Uncertainty in seismometers' position	48
3.6.4. The effect of local soil condition and phase	50
3.7. Real data	52
3.8. Array-derived rotation rate versus transverse acceleration	52
3.9. Discussion and conclusions	57
4. Love-wave dispersion from collocated measurements of rotation and translations	60
4.1. Introduction	60
4.2. Surface-wave Phase velocity determination	63
4.2.1. Rotation rate and transverse acceleration	65
4.3. Phase velocity determination in the time domain	66
4.3.1. Observations and data analysis	71
4.3.2. Point measurements	72
4.4. Conclusion	78
5. Horizontal components of rotation or tilt	80
5.1. Introduction	80
5.2. The tiltmeter	83
5.3. Tilt and horizontal accelerations	84
5.4. Array-derived horizontal components of rotations	89
5.4.1. Synthetic study of array derived tilt rate	89
5.4.2. Array-derived tilt rate from observed data	91
5.5. Rayleigh-Wave Phase velocity from collocated measurements	94
5.6. Tilt-corrected ring laser data	99
5.7. Conclusion	105

6. Conclusions and Outlook	107
6.1. Conclusions	107
6.2. Outlook	108
A. Contents of the Attached DVDs	110
References	117
Acknowledgments	118
Lebenslauf	119

List of Figures

1.1.	Various rotational effect on tombstone induced by earthquake. Top figure: Overturned tombstone after South-central Illinois earthquake November 9, 1968 (Gordon <i>et al.</i> , 1970). Top left: Clockwise rotated tombstone at Campground Cemetery. Top right: Counterclockwise rotated tombstone at Rector Cemetery. Bottom figures: Rotated tombstone after M7.0 Miyagi-Oki earthquake of May 26, 2003 (Photo Courtesy of The Disaster Control Research Center, Graduate School of Engineering, Tohoku University).	2
2.1.	Cartesian and spherical polar coordinates for analysis of radial, and transverse components of displacement as well as rotation caused by a shear dislocation of area A and average slip $\langle \Delta u(t) \rangle$	8
2.2.	Far field P-wave radiation pattern in x_1, x_3 plane for radial component of displacement due to a double couple in plane x_1, x_2 . . .	10
2.3.	Radiation pattern of the transverse component of displacement due to a double couple. The blue arrow shows the sense of shear dislocation. The arrow in each lobe represent the direction of particle displacement associated with the lobe.	10
2.4.	Radiation pattern of the transverse component of rotation due to a double couple point source. The arrow in each lobe represents the rotation of grains adjacent to the internal slip planes.	11
2.5.	Normalized translational (black) and rotational (red) motions at seismometers located in various directions.	12

List of Figures

2.6. Simulation setup for showing the peak ground velocity and peak ground rotation. The spherical coordinate was used as in Figure 2.1. x and y represent the direction in x offset and y offset respectively.	13
2.7. Contour plot of numerically computed peak ground velocity and peak ground rotation rate for 10 km deep double-couple point source of 10^{24} dyne. cm in an infinite homogeneous medium. . . .	14
2.8. Cross section plot of peak ground velocity and peak ground rotation rate for an 10 km deep double-couple point source of 10^{20} dyne. cm in an infinite homogeneous medium.	15
2.9. Contour plot of numerically computed static displacement and static rotation for an 10 km deep double-couple point source of 10^{24} dyne.cm in an infinite homogeneous medium.	16
2.10. Cross section plot of static displacement and static rotation for an 10 km deep double-couple point source of M5.5 in an infinite homogeneous medium.	17
2.11. Two antiparallel seismographs developed in the Institute of Geophysics, Polish Academy of Science (Solarz <i>et al.</i> , 2004)	18
2.12. Solid state GyroChip schematic diagram. It contains a vibrating quartz tuning fork to sense rate, and acting as a Coriolis sensor, coupled to a similar tines as a pickup to produce the rotation rate output signal.	21
2.13. Ring laser measurement principle. Two counter-rotating laser beam interfere to generate a beating when the system rotates with respect to the normal. The beating frequency is directly proportional to rotation rate.	22
2.14. "G" ring laser installed at Wettzell.	24
2.15. Block diagram of the principal structure of the GEOsensor	25
2.16. "Geosensor" Ring laser installed in Wettzell, Germany	27
2.17. Building damage after a strong earthquake, that may be caused by rotational motion. Left photo is courtesy of the Geological Survey of Canada. Right photo Edwards, 1999.	29

3.1. Location of the array experiment. The ring laser and GRSN (German Regional Seismic Network) broadband station (WET) are located at the center of the array marked by a triangles. The ring laser and the broadband seismometer are separated by approximately 250 m.	34
3.2. Station S1 located near a farm with the sensor was buried with a bottom depth about 50 cm.	35
3.3. Station S4 is located on outcropping large igneous rock boulders. .	36
3.4. Comparison of normalized velocity seismograms for the M6.4 Al Hoceima Morocco earthquake recorded by S1 and broadband station. Significant change of wavefrom after corrected for the instrument response is clearly shown. All the seismograms are bandpass filtered from 0.03 Hz to 0.3 Hz.	38
3.5. True amplitude velocity seismograms for the M6.4 Al Hoceima Morocco earthquake of February 24, 2004, recorded by the array. A superposition of all seismograms in a 2-minute time window is shown in the lower part. All the seismograms, including the broadband seismogram (WET, top), are corrected for the instrument response and bandpass filtered from 0.03 Hz to 0.5 Hz.	39
3.6. Synthetic velocity seismograms for the M6.4 Al Hoceima Morocco earthquake of February 24, 2004, for all the array's station as well as the central station (WET), calculated for a 3D mantle model (Ritsema & Van Heijst, 2000) and a recent crustal model (Bassin <i>et al.</i> , 2000). The seismograms, calculated using the spectral element method (Komatitsch & Tromp, 2002a,b), have been lowpass filtered (< 0.05 Hz).	42
3.7. Synthetic test of uniformity of rotation rate across the array. Four pairs of the vertical component of rotation rate at the array center (black line) and array-derived rotation rate (gray line) calculated using three stations. Top right: stations WET, S5 and S8; bottom right: stations WET, S7 and S8; bottom left: stations WET, S6 and S7; top left: stations WET, S6 and S5. The normalized correlation coefficients are given for each trace pair.	43

3.8. Non uniformity of array-derived rotation rate across the array for different triangles for real data. Top right: stations WET, S5 and S8; bottom right: stations WET, S7 and S8; bottom left: stations WET, S6 and S7; top left: stations WET, S6 and S5. The normalized correlation coefficients are given for each trace pair. . .	44
3.9. Non uniformity of array-derived rotation rate across the array for different triangles for synthetic data with a single phase-disturbed station (S8) and 3% of random noise added for all stations. a) Four pairs of the vertical component of ring laser data (black line) superimposed with array-derived rotation rate (gray line) calculated using three stations. Top right: stations WET, S5 and S8; bottom right: stations WET, S7 and S8; bottom left: stations WET, S6 and S7; top left: stations WET, S6 and S5. b) The vertical component of array-derived rotation rate (gray) is calculated from all eight stations (S1-S8) with WET station as reference. The normalized correlation coefficients are given for each trace pair. . .	46
3.10. Vertical component of array-derived rotation rate from synthetic data with Gaussian random noise (with 25 noise realizations) (gray line), superimposed with the noise-free synthetic rotation rate (black line). The amount of noise is 10%, 5% and 1%, from top to bottom.	47
3.11. a) Vertical component of array-derived rotation rate from synthetic data with real noise taken from the observed seismograms several minutes before the event started; b) The effects of a ± 30 m error in seismometer position on the derivation of rotation rate for 25 realizations).	49
3.12. Vertical component of array-derived rotation rate for synthetic data with amplitude uncertainty of 10%, 5%, and 1% (top to bottom), from 25 realizations (gray lines) superimposed with synthetic rotation rate (black line).	50

3.14. Vertical component of array-derived rotation rate from real array data set (gray line) superimposed with ring laser data (black line). Nine stations including the broadband data are used to calculate the array-derived rotational signal. Both traces are bandpass filtered from 0.03 Hz to 0.3 Hz	53
3.15. Horizontal component of the velocity recorded by the array seismometer for the December 26, 2003, Bam, Iran earthquake. The data from station S2, S5, S6 and broadband are used to derive the rotations. a)The East-West components, b) The North-South components.	54
3.16. Horizontal component of the velocity recorded by the array seismometer for the 7 February 2004 Papua, Irian Jaya Indonesia earthquake. The data from station S2, S5, S6 and broadband are used to derive the rotations. a)The East-West components, b) The North-South components.	55
3.17. Comparison of collocated transverse acceleration (red lines) observed by GRSN broadband seismometer with array derived rotation rate (black lines) for the Bam, Iran earthquake.	56
3.18. Comparison of collocated transverse acceleration (red lines) observed by GRSN broadband seismometer with array derived rotation rate (black lines) for the Papua, Indonesia earthquake.	57
4.1. Rotational motion induced by Love and Rayleigh waves. Love-wave will trigger a vertical component of rotation, while a Rayleigh wave will induced a horizontal component of rotation on a rotation sensor.	63
4.2. The dependence of the dispersion of surface waves on the velocity gradient in the vertical direction. A stronger vertical velocity gradient causes greater dispersion (Modified from Lay & Wallace (1995)).	65

4.3. Point measurement analysis for synthetic data for Al Hoceima events (Figure 3.6). The transverse acceleration and rotation rate about a vertical axis in the reference station is plotted in the first upper figure, following by the estimated back azimuth and the phase velocity estimates. The actual back azimuth is represented by red line.	68
4.4. Phase velocity estimation of synthetic data for Papua, Irian Jaya events. The transverse acceleration and rotation rate about a vertical axis in the reference station is plotted in the first upper figure, following by the estimated back azimuth and the phase velocity estimates. The actual back azimuth is represented by red line. . .	69
4.5. Phase velocity estimation of synthetic data for Hokkaido events. The transverse acceleration and rotation rate about a vertical axis in the reference station is plotted in the first upper figure, following by the estimated back azimuth and the phase velocity estimates. The actual back azimuth is represented by red line.	70
4.6. Upper trace: Transverse acceleration (gray, left axis) and rotation rate about the vertical axis (black, right axis) for the Greece event, M6.3, 14 August 2003. Bottom trace: Best-fitting horizontal phase velocities as a function of time in a 10 s sliding window.	73
4.7. Upper trace: Transverse acceleration (gray, left axis) and rotation rate about the vertical axis (black, right axis) for the Siberia event, M6.7, 1 October 2003. Bottom trace: Best-fitting horizontal phase velocities as a function of time in a 10 s sliding window.	74
4.8. Frequency-dependent Love wave phase velocities from spectral ratios of synthetic seismograms calculated for the Gibraltar, Papua and Hokkaido events (see text for details) shown as mean values with variances as Gaussian uncertainties. The dashed lines indicate the theoretical fundamental- (lowest dashed line) and higher-mode Love-waves phase velocities (upper dashed lines) obtained for the ak135 Earth model.	76

4.9. Love waves phase velocities derived from observed data shown as mean values (black) and associated uncertainties using grey shading (see text for details) for all event listed in Table 1. The dashed lines indicate fundamental- and higher-mode Love-waves phase velocities obtained for the ak135 Earth model.	77
5.1. Three components of torsional motions in aeronautics are known as Pitch, Roll and Yaw.	81
5.2. Bubble-tube tiltmeter in horizontal state.	83
5.3. Bubble-tube tiltmeter in inclined state.	84
5.4. Three components of rotation from Al Hoceima earthquake event. Left side is for synthetic data and Right side is observed. See text for more details	85
5.5. Superimposed plot between tilt and acceleration divided by a factor of g in x and y component.	86
5.6. Superimposed plot between tilt and acceleration in x and y component low pass filtered at various cut off frequencies. The first upper figure is unfiltered, followed by cut off period of 1 s, 10 s, 20 s, 30 s, and 40 s.	87
5.7. Similar than Figure 5.6 but with cut off frequencies of 50 s, 60 s, 70 s, 80 s, 90 s, and 100 s.	88
5.8. The array station setup. WET is the reference station located at the center of the array.	90
5.9. Three components of rotation from Gibraltar synthetic data. The red line is synthetic rotation calculated in the array center (WET) using nine stations including the reference station and the black line is array-derived rotation.	90
5.10. Three components of rotation from Synthetic Hokkaido data. The red line is synthetic rotation calculated in the array center (WET) using nine stations including the reference station and black line is array-derived rotation.	91

5.11. Three components of rotation from Synthetic Papua Irian Jaya data. The red line is synthetic rotation calculated in the array center (WET) using nine stations including the reference station and black line is array-derived rotation.	92
5.12. The horizontal components of rotation from Bam, Iran event. Left: The array-derived rotation (black). Right: Observed tilt recorded by the tiltmeter (red).	93
5.13. Superimposed plot of radial component of acceleration (blue line) versus transverse array-derived tilt (green line) for Bam, Iran event.	94
5.14. Three components of rotation from Irian Jaya event. Left: The array-derived rotation (black). Right: Observed tilt recorded by the tiltmeter (red).	95
5.15. Superimposed plot of radial component of acceleration (blue line) versus transverse array-derived tilt (green line) for Papua, Irian Jaya earthquake.	95
5.16. Superposition of radial acceleration (black) and transverse tilt (red) and determination of rayleigh wave phase velocities as a function of dominant period after narrow-band filtering (see text for details). The phase velocities given for each trace pair were determined by dividing the peak radial acceleration by the peak tilt rate (and corrected for the factor of the cut off period). Synthetic event in Gibraltar, M6.3, 24 February, 2004.	97
5.17. Superposition of radial acceleration (black) and transverse tilt (red) and determination of rayleigh wave phase velocities as a function of dominant period after narrow-band filtering (see text for details). The phase velocities given for each trace pair were determined by dividing the peak radial acceleration by the peak tilt rate (and corrected for the factor of the cut off period). Synthetic event in Irian Jaya, M7.1, 07 February, 2004.	98

5.18. Superposition of radial acceleration (black) and transverse tilt (red) and determination of rayleigh wave phase velocities as a function of dominant period after narrow-band filtering (see text for details). The phase velocities given for each trace pair were determined by dividing the peak radial acceleration by the peak tilt rate (and corrected for the factor of the cut off period). Synthetic event in Hokkaido, M8.3, 25 September, 2003.	100
5.19. Superposition of radial acceleration (black) and transverse tilt(red) and determination of Rayleigh wave phase velocities as a function of dominant period after narrow-band filtering (see text for details). Al Hoceima event, M6.3, 24 February 2004.	101
5.20. Superposition of radial acceleration (black) and transverse tilt(red) and determination of Rayleigh wave phase velocities as a function of dominant period after narrow-band filtering (see text for details). Papua, Irian Jaya event, M7.3, 7 February 2004.	102
5.21. Superposition of radial acceleration (black) and transverse tilt(red) and determination of Rayleigh wave phase velocities as a function of dominant period after narrow-band filtering (see text for details). Bam, Iran event, M6.3, 26 December 2003.	103
5.22. Tilt correction for Hokkaido synthetic event. Upper plot: tilt correction assumed tilt rate was obtained with tiltmeter, lower part: tilt correction using pure tilting rate.	104
5.23. Tilt correction for Irian Jaya synthetic event. Upper plot: tilt correction assumed tilt rate was obtained with tiltmeter, lower part: tilt correction using pure tilting rate.	105

Zusammenfassung

Die seismischen Wellen, die sich vom Erdbebenherd durch die gesamte Erde ausbreiten, werden durch ein Seismometer mit seinen drei orthogonalen Komponenten (Z (vertikal), N (Nord-Süd) und E (Ost-West)) gemessen. Jedoch besteht eine komplette Beschreibung der durch Erdbeben verursachten Bodenbewegung nicht nur aus den drei translatorischen Anteilen, sondern auch aus drei Komponenten der Drehbewegung (Rotationen) sowie sechs weiteren Komponenten der Dehnung. Obwohl theoretische Seismologen auf den möglichen Nutzen der Messung der Drehbewegung schon lange hingewiesen haben, wurde diese erst von Kurzem verwirklicht. Die Ursache dafür war hauptsächlich das Fehlen präziser Instrumente zur Messung der Drehbewegung.

In der Seismologie ist die Messung dieser durch Erdbeben verursachte Rotationen verhältnismäßig neu. Nach meinen besten Kenntnissen wurde das erste Experiment zur Messung der Rotationsbodenbewegung durch einen Rotationssensor von Nigbor (1994) durchgeführt. Er maß erfolgreich mit einem dreiachsigen Beschleunigungsaufnehmer und einem Festkörperrotationssensor die Bodenverschiebung und Rotationsbewegung während eines unterirdischen chemischen Explosionsexperimentes im Nevada Versuchsgelände. Die gleiche Art Sensor wurde auch von Takeo (1998) für die Beobachtung eines Erdbebenschwarmes auf der Izu Halbinsel in Japan benutzt. Jedoch war man aufgrund der Beschränkung der Instrumentempfindlichkeit diese Sensoren nur in der Lage, Rotationsbewegung zu messen, die nahe der Erdbebenherde oder anderer künstlicher Quellen auftreten.

Eine andere Art eines Rotationssensors wurde durch zwei entgegengesetzt orientierte Seismometer verwirklicht (z.B., Moriya & Marumo, 1998; Solarz *et al.*, 2004; Teisseyre *et al.*, 2003). Diese Methode ist prinzipiell möglich, weil die Rotationskomponente der Bodenbewegungen zu den horizontalen Gradienten Bodengeschwindigkeit proportional ist. Dieser Sensortyp wurde intensiv von der

Seismologiegruppe am Institut für Geophysik der polnischen Akademie der Wissenschaften erforscht und entwickelt. Jedoch berichteten die dortigen Forscher über mehrere Probleme besonders wegen der kleinen ungewollten Unterschiede in der Empfindlichkeit des Seismometers. Wie bei den Festkörperrotationssensoren war diese Sensor darauf beschränkt, Rotationsbewegungen nahe der seismischen Quellen zu messen.

Die Ausnutzung des sogenannten Sagnac-Effektes für die Messung der Trägheitsumdrehung mittels optischer Vorrichtungen wurde seit der Erfindung des Laser in den Sechzigern Jahren des 20. Jahrhunderts intensiv erforscht. Jedoch wurde von der Anwendung eines Ringlasers als Drehbewegungssensor in der Seismologie zum ersten Mal von Stedman u.a. (1995) berichtet.

Völlig konsistente Drehbewegungen wurden mit Hilfe eines Ringlasers an der Fundamentalstation Wettzell, Deutschland aufgezeichnet (Igel u.a., 2005). Die Autoren zeigen, dass die Rotationsbewegungen sowohl in Amplitude als auch in Phase mit den Aufzeichnungen der Transversalbeschleunigung durch ein Standardseismometer übereinstimmen. Sie merken auch an, daß Standard-Rotationssensoren mit ausreichender Auflösung in der nahen Zukunft verwirklicht werden können. Vergleichbar mit anderen Arten von Rotationssensoren scheinen Ringlaser zuverlässiger in der seismischen Anwendung zu sein, da sie in der Lage sind, die Bodenrotation sowohl von lokalen als auch von teleseismischen Erdbeben aufzuzeichnen (Igel u.a., 2006).

Für das Erdbebeningenieurwesen kann die Beobachtung der Rotationskomponenten insofern von Interesse sein, da diese Art von Bewegung zur Gesamtbewegung eines Gebäudes beiträgt, welches letzteres durch ein Erdbeben erleidet. Ein Großteil der Bodenrotationsmessungen in der Ingenieursseismologie werden bis jetzt hauptsächlich durch indirekte Messungen (d.h. mittels Array-Techniken) ausgeführt. Dies ist möglich, da die Rotationskomponente der Bewegung eine Linearkombination der Ableitungen des horizontalen Anteils der Translationsbewegungen ist. Dennoch ist nach unserer Kenntnis noch kein Vergleich zwischen direkten (Rotationssensor) und indirekten Messungen (Array-Technik) durchgeführt worden.

Die Hauptaufgabe dieser Doktorarbeit ist daher, die Effekte von seismischem Rauschen und zahlreicher Unsicherheitsfaktoren bei der Bestimmung der Rota-

tionsrate mittels Array-Techniken herauszuarbeiten und die Ergebnisse direkt mit Ringlaserdaten zu vergleichen. In dieser Arbeit wird erstmals gezeigt, dass beide Methoden (direkt und indirekt) ein beinahe gleiches Resultat (Korrelationskoeffizient von 93 %) liefern. Allerdings ist zu beachten, dass mehr als nur drei Seismometer wegen der Störerräuschempfindlichkeit verwendet werden müssen, um ein besseres und zuverlässigeres Ergebnis zu erhalten. Da die Array-Technik im Dauerbetrieb mit zu großen Wartungsarbeiten verbunden ist, bleibt der Ringlaser als präziser und handlicher Rotationssensor das Instrument der Wahl in der Seismologie.

Dies Gesamtheit der Aspekte des Nutzen der Bestimmung der Rotationsbewegung die Seismologie ist noch Gegenstand der Forschung. Die Rotationsbewegungen stellen ausführliche Daten für die Ankunftszeiten der SH-Wellen zur Verfügung; und möglicherweise in dem näherem Bereich des Erdbebenherdes auch genauere Information der Bruchprozesse von Erdbeben. Außerdem konnten die Drehbewegungen auch verwendet werden, um Schätzungen der statischen Verschiebung von den seismischen Messungen zu verbessern, da die vollständige Beschreibung der Bodenbewegung auch eine Rotationskomponente beinhaltet.

Vor kurzem stellte Igel u.a. (2005) eine Methode für die Abschätzung der horizontalen Phasengeschwindigkeit mittels Kombination von Ringlaserdaten sowie Standard- (d.h. Translations-) Seismometer-Daten vor. Im Gegensatz dazu verwendet das Standardverfahren für die Bestimmung der Phasengeschwindigkeit (aufwändigere) Array-Messungen.

Der einfache Zusammenhang zwischen der Translationsbeschleunigung und der Rotationsrate (um die vertikale Achse) zeigt, daß beide Signale in ihrem Verhältnis zur horizontalen Phasengeschwindigkeit proportional sind. Der Vergleich mit simulierten Seismogramme (Rotationen und Verschiebungen) und den in der gleichen Weise bestimmten Phasengeschwindigkeiten zeigte eine gute Übereinstimmung mit den Beobachtungen.

Ein weiteres Ziel dieser Doktorarbeit ist die Untersuchung der Genauigkeit der Phasengeschwindigkeitsbestimmung mittels gemeinsamer Messungen der Rotations- und Translationsbewegungen sowie die Ableitung von Dispersionskurven von Love-Wellen mit Hilfe des spektralen Verhältnisses sowohl für simulierte als auch für

real beobachtete Daten. Ob die Genauigkeit der so abgeleiteten Dispersionskurven mit der in dieser Doktorarbeit vorgestellten Methode für die tomographischen Zwecke ausreicht, bedarf noch weiteren speziellen Studien.

Nichtsdestotrotz ergibt sich aus den gezeigten Ergebnissen, dass durch zusätzliche Messungen des genauen Rotationssignals Wellenfeldinformationen zu Tage treten, die sonst nur durch Array-Messungen ermittelbar wären.

Allerdings, um diese Methodik für die Seismologie praktisch nutzbar zu machen, ist die Entwicklung eines passenden hochauflösenden Sechskomponent-Breitband-sensors nötig. Es gibt bereits Bemühungen, solche Entwicklungen auf internationaler Ebene zu koordinieren (Evans u.a., 2006)

Ein letzter Schwerpunkt dieser Arbeit liegt auf der *Neigung* (Tilt) des Bodens durch Erdbeben wellen. Sie ist im Allgemeinen klein aber in der Seismologie nicht unwesentlich, besonders bei starken Erdbeben. Es ist weithin bekannt, daß das Neigungssignal besonders in den horizontalen Komponenten des Seismometers zu beobachten ist. Ignoriert man den Neigungseffekt, so führt dies zu unzuverlässigen Resultaten, besonders in der Berechnung der dauerhaften Bodenverschiebungen und der langperiodischen Bewegungen. Ein weiteres interessantes Ergebnis im Rahmen der Untersuchung der Bodenneigung ist die Ableitungsmöglichkeit der Phasengeschwindigkeit sowie der Dispersionskurve von Rayleighwellen mittels kombinierter Messungen der Neigungsrate und der translatorischen Bodenbewegung. Eine Studie anhand von Simulationen zeigt, daß es eine frequenzabhängige Phasengeschwindigkeit aus der Radialbeschleunigung und der Querneigung an einem Ort berechnet werden kann. Die selbe theoretische Studie zeigt aber, daß bei Verwendung der Neigungsdaten eines Tiltmeters zur Korrektur der Ringlaserdaten im Vergleich zum wirklichen Neigungssignal etwa 100-fach zu hohe Korrekturen angewendet werden. Dies läßt sich damit erklären, daß das Tiltmeter ein pendelartiger Sensor ist, der für horizontale Beschleunigungen anfällig ist.

Diese Arbeit umfasst vier Kapitel.

Im ersten Kapitel wird das Grundprinzip der Rotationsbewegungen dargestellt, sowie auf zahlreiche heute verfügbare Sensortypen sowie Anwendungen von Rotationsmessungen eingegangen.

Das nächste Kapitel widmet sich dem ersten Aspekt dieser Arbeit. In ihm wird kurz auf Array-Experimente und den Einfluss verschiedener Unsicherheiten dieser Experimente eingegangen. Dann wird erstmals ein direkter Vergleich zwischen Rotationsbewegungen die mit Array-Messungen bestimmt wurden und solchen, die mit der Ring-Laser Technik gemessen wurden, gezeigt.

Im dritten Kapitel wird der nächste Aspekt dieser Arbeit behandelt, nämlich der Kombination von Rotationsdaten mit Translationsdaten zur Bestimmung der Phasengeschwindigkeit und der Einfallsrichtung von Wellen. Dies war bisher nur mit Array-Techniken möglich.

Im letzten Kapitel wird dann auf den Aspekt der Neigungsmessung mittels Arrays eingegangen und mögliche Anwendungen von Neigungsdaten diskutiert.

Summary

The seismic waves that spread out from the earthquake source to the entire Earth are usually measured at the ground surface by a seismometer which consists of three orthogonal components (Z (vertical), N (north-south), and E (east-west) or R (radial), T (transversal), and Z (vertical)). However, a complete representation of the ground motion induced by earthquakes consists not only of those three components of translational motion, but also three components of rotational motion plus six components of strain. Although theoretical seismologists have pointed out the potential benefits of measurements of rotational ground motion, they were not made until quite recently. This was mainly because precise instruments to measure ground rotational motion were not available.

The measurement of rotational motion induced by earthquakes is relatively new in the field of seismology. To the best of our knowledge, the first experiment to measure ground rotational motion using rotational sensor was done by (Nigbor, 1994). He successfully measured translational and rotational ground motion during an underground chemical explosion experiment at the Nevada Test Site using a triaxial translational accelerometer and a solid-state rotational velocity sensor. The same type of sensor was also used by Takeo (1998) for recording an earthquake swarm on Izu peninsula, Japan. However, because of the limitation of the instrument sensitivity, this kind of sensor was only able to sensing the rotational ground motion near the earthquake sources of other artificial sources. Another type of rotational sensor was assembled using two oppositely oriented seismometers. This is possible since in principle the rotational component of the ground motions is equal to half the curl of the ground velocity. This kind of sensor was intensively researched and developed by the seismology group in Institute of geophysics, Polish Academy of Sciences. However, they report several problems especially due to the small differences in the seismometer's response

function. Like the solid state rotational sensors, this sensor was only able to measure rotational motion near the seismic sources.

The application of the Sagnac effect for sensing the inertial rotation using optical devices were intensively investigated, since the advent of lasers in the sixties. However, the first application of a ring laser gyroscope as a rotational sensor applied in the field of seismology was reported by Stedman *et al.* (1995). Fully consistent rotational motions were recorded by a ring laser gyro installed at the fundamental station Wettzell, Germany (Igel *et al.*, 2005). They showed that the rotational motions were compatible with collocated recordings of transverse acceleration by a standard seismometer, both in amplitude and phase. They mentioned that "standard" rotational sensors with sufficient resolution may be possible in the near future. Among the other type of rotational sensor, ring lasers seem more reliable in seismic applications since it has been provenable to sensing the ground rotational motion from near source as well as teleseismic earthquake events with a broad magnitude range (Igel *et al.*, 2007).

In earthquake engineering, observations of rotational components of seismic strong motions may be of interest as this type of motion may contribute to the response of structures to earthquake-induced ground shaking. Most of rotational/torsional studies of ground motion in earthquake engineering are so far still carried out by indirect measurements. It can be done since the rotational component of motion is a linear combination of the space derivatives of the horizontal component of the motion. However, to the best of our knowledge, there are no comparison of array-derived rotation rate and direct measurement from rotational sensors mentioned in the literature.

The first objective of my thesis is to study the effect of noise and various uncertainties to the derivation of rotation rate and to compare directly the result with the ring laser data. Here we present for the first time a comparison of rotational ground motions derived from seismic array with those observed directly with ring laser. Our study suggest that – given accurate measurements of translational motions in an array of appropriate size and number of stations – the array-derived rotation rate may be very close to the "true" rotational signal that would be measured at the center of the array (or the specific reference station). However, it is important to note that it may be dangerous to use only the minimally required

three stations as even relatively small noise levels may deteriorate the rotation estimates. Furthermore, it is clear that the logistic effort to determine rotations from array is considerably larger than direct measurements. In the light of this, the necessity to develop field-deployable rotational sensors with the appropriate resolution for use in local and regional seismology remains an outstanding issue.

More recently, Igel *et al.* (2005) introduced a method to estimate the horizontal phase velocity by using collocated measurements from a ring laser and seismometer. A simple relationship between transverse acceleration and rotation rate (around a vertical axis) shows that both signals should be in phase and their ratio proportional to horizontal phase velocity. Comparison with synthetic traces (rotations and translations) and phase velocities determined in the same way showed good agreement with the observations.

The second objective of my thesis is to study the accuracy of phase velocity determination using collocated measurement of rotational and translational motion and derive the Love wave dispersion curve using spectral ratio for both synthetic and real observed data. Whether the accuracy of the dispersion curves derived with the approach presented in this thesis is enough for tomographic purposes remains to be evaluated. Nevertheless, the results shown here indicate that through additional measurements of accurate rotational signals, wavefield information is accessible that otherwise requires seismic array data. However, to make this methodology practically useful for seismology will require the development of an appropriate high-resolution six-component broadband sensor. Efforts are underway to coordinate such developments on an international scale (Evans *et al.*, 2006).

The ground tilt is generally small but not negligible in seismology, especially in the strong-motion earthquake. It is well known that the tilt signal is most noticeable in the horizontal components of the seismometer. Ignoring the tilt effects leads to unreliable results, especially in calculation of permanent displacements and long-period calculations.

The third objective of my thesis is to study the array-derived tilt, a further application of measuring tilt. An interesting result concerning tilt study based on a synthetic study is the possibility to derive the Rayleigh wave phase velocity as well as Rayleigh wave dispersion curve from collocated measurement of tilt rate

and translational motions. The synthetic study shows that there is a frequency dependent phase velocity from collocated radial acceleration and transverse tilt.

There is a normal procedure to correct the orientation change of the ring laser by using a tiltmeter during measurements. However, since a tiltmeter is measuring not only the real tilt signal, but also the horizontal accelerations, it will overestimate the correction value. Based on the synthetic study, it is found that such correction will lead to values about 100 times higher than the correction with true tilt signal.

This thesis contains four chapters. In the first chapter I discuss the basic principle of rotational motions, various rotational sensors available recently and several applications of measuring rotational ground motions. The first objective of my thesis is described in the second chapter. In this chapter, I briefly describe the array experiment, the effect of several uncertainties and show the first ever direct comparison of array-derived ground rotational motions with the ring laser data. The second objective of my thesis is explained in the third chapter. We discuss the application of rotational in addition with translational data to derive the phase velocity and the direction of wave propagation previously only possible using array techniques or additional strain measurements. In the fourth chapter I discuss the array-derived tilt and possible application of tilt data. The last chapter is a general conclusion.

1. Introduction

”Perfectly general motion would also involve rotations about three perpendicular axes, and three more instruments for these. Theory indicates, and observation confirms, that such rotations are negligible.”

(Richter, 1958)

The effect of the rotational ground motion has attracted the consideration of only very few seismologists in the last decades. Although several classical textbooks (e.g., Davidson, 1927; Gutenberg, 1959; Hobbs, 1907; Imamura, 1937) have mentioned that the effect of rotational motion induced by earthquakes can be observed on the ground surface and some structures, the instrument for measuring ground rotational motion has not yet met the accuracy needed in seismological applications. In earthquake engineering, the rotational ground motion effect has also been recognized for causing structural damage especially for long structures such as bridges and pipelines or transmission systems (e.g., Hart *et al.*, 1975; Zerva & Zhang, 1997). In the beginning, those effects were supposed to be due to the asymmetry of the structure or building. Yet, recent studies show that even symmetrical buildings would also be excited into rotational modes about a vertical axis (e.g., Awad & Humar, 1984; Li *et al.*, 2001; Newmark, 1969). Figure 1.1 shows various effects of rotational motions induced by earthquakes on tombstones induced by South-central Illinois earthquake November 9, 1968 (Top figures) and M7.0 Miyagi-Oki earthquake of May 26, 2003 (Bottom figures).

Bouchon & Aki (1982) simulated rotational ground motion near earthquake faults buried in homogeneous layered media for strike-slip and dip-slip fault mod-



Figure 1.1: Various rotational effect on tombstone induced by earthquake. Top figure: Overturned tombstone after South-central Illinois earthquake November 9, 1968 (Gordon et al., 1970). Top left: Clockwise rotated tombstone at Campground Cemetery. Top right: Counter-clockwise rotated tombstone at Rector Cemetery. Bottom figures: Rotated tombstone after M7.0 Miyagi-Oki earthquake of May 26, 2003 (Photo Courtesy of The Disaster Control Research Center, Graduate School of Engineering, Tohoku University).

els. They showed that the maximum rotational velocity produced by a buried 30 km long strike-slip fault with slip of 1 m is 1.5×10^{-3} rad/s. This value is indeed small compared with the amplitude of the translational motion, but in the sense of rotational motions induced by earthquakes, it is not negligible. They also conclude based on this simulation that rotation, strain and tilt are closely related to ground velocity and the phase velocities associated with strong ground motion are controlled by the rupture velocity and the basement rock shear wave velocity.

Although rotational sensors were available in the last years (especially for navigation purposes), such instruments with appropriate precision for geophysical applications were not available until quite recently (Nigbor, 1994). The application of the Sagnac effect for sensing the inertial rotation using optical devices was intensively investigated, since the advent of lasers in sixties (Post, 1967). There are two approaches to apply the Sagnac effect for rotational measurements, namely active techniques, as in ring laser gyroscopes, and passive techniques, as in fiber-optic interferometers (Sanders *et al.*, 1981). The first application of a ring laser gyroscope as a rotational sensor in seismology was reported by Stedman *et al.* (1995). Furthermore, McLeod *et al.* (1998) gave a detailed analysis of observations with the ring laser CI, installed in the Cashmere cavern, Christchurch, New Zealand. They reported that the phase of rotation determined by CI is partly consistent with that of a collocated standard seismometer record, during the $M_L 5.3$ Kaikoura event on 5 September 1996. Pancha *et al.* (2000) analyzed the horizontal and vertical components of teleseismic surface and body waves recorded by larger ring laser gyroscopes (CII and G0) caused by M7.0 and M7.3 events at distances of 31° and 42.6° , respectively. Apart from amplitudes of rotation rates larger than expected, they showed that the sensors provided sufficient accuracy to record seismic rotations. Fully consistent rotational motions were recorded by a ring laser gyro installed at the fundamental station Wettzell, Germany (Igel *et al.*, 2005). They showed that the rotational motions induced by the teleseismic event was compatible with collocated recordings of transverse acceleration by a standard seismometer, both in amplitude and phase.

In earthquake engineering, observations of rotational components of seismic strong motions may be of interest as this type of motion may contribute to the

response of structures to earthquake-induced ground shaking (Li *et al.*, 2001). Rotational motions can be derived from measuring translational motion in several locations (array). Most of rotational/torsional studies of ground motion in earthquake engineering are so far still carried out by indirect measurements. Indirect measurements of rotational motions using a seismo(accelero)meter array have been studied by several investigators (e.g., Bodin *et al.*, 1997; Huang, 2003; Li *et al.*, 2001; Niazi, 1986; Oliveira & Bolt, 1989; Singh *et al.*, 1997; Spudich *et al.*, 1995). However, a comparison of array-derived rotation rate and direct measurement from rotational sensors has never been mentioned in the literature, as no appropriate sensor was available.

The full benefits of the determination of rotational motion in seismology are still under investigation. Recent result suggest that the horizontal phase velocity can be estimated by analyzing a collocated recording of rotation and translation ground motion data (Igel *et al.*, 2005). The conventional procedure to estimate the phase velocity is by using array measurements. Using this technique, it would be more cost efficient since it only needs one three component seismometer and a rotational sensor. With array measurements, other properties such as the direction of wave propagation (back azimuth) and the dispersion curve can be derived. If these properties can also be computed from collocated recordings of rotation and translational ground motions, then it may have implication for sparse networks or situations where extremely few or even single-station observations are taken (e.g. in remote areas or planetary seismology).

In the past years, the contribution of rotational motion to the translational ground motion recording has been recognized (e.g., Trifunac & Todorvska, 2001). Especially the horizontal component of rotation (tilt) significantly affects the horizontal component of the transverse recording. These effects can be neglected in some far-field measurements, but must be included in the near-field studies. So far, this effect is usually removed by filtering the seimogram, since it can remove the long-period components partially introduced by tilting. However, by filtering the seimogram, the tilt effect still can not be fully removed (Graizer, 2005).

Graizer (2005) suggests to measure three components of rotational motion including tilt in order to fully remove the tilt effect in the translational recording. Although there are several kinds of tiltmeters available for this application, such

instruments may be sensitive to meteorological and local disturbances or to horizontal accelerations.

1.1. Objectives

There are three main objectives of this thesis. First, we want to demonstrate that rotational motion derived from several translational records (seismometer array) or indirect method is possible and provide the first ever comparison with direct measurements. We will further study the effect of noise and other "unwanted" signal contaminated in the data and their relevance to the derivation of rotation. We will first present a synthetic study, in which we investigate the influence of various effects on array derived rotation rate. These effects are (1) unwanted signals (i.e., noise) in the horizontal components of translation, (2) uncertainty in seismometer calibration, and (3) uncertainty in station coordinates. Finally, we show the direct comparison of the vertical component of array-derived rotation rate with the ring laser gyroscope as well as collocated transverse acceleration record from broadband station. On the other hand, this comparison will also provide information about the performance of the rotational sensor (ring laser) itself.

The second objective is, to determine the phase velocity and direction of wave propagation (back azimuth) as well as determining the Love wave dispersion curve from collocated rotational and translational sensor and compare with array-derived estimates. This is a novel approach since the standard way to derive the phase velocity is by analysis from seismic arrays. This point measurement will open in principle the possibilities for structural inversion.

The third objective in this thesis is to derive the horizontal rotation (tilt) from array data. Possible application of tilt data for deriving Rayleigh wave dispersion will be presented and the problem of tilt correction on ring laser data is revisited.

1.2. Structure of the Thesis

This thesis is structured as follows:

Chapter 1, *Introduction*, is the overview of the thesis.

Chapter 2, *Rotational ground motion*, I summarize all general aspect of rotational motion including basic theory, rotational motions instrumentation, applications and some observations. In the beginning rotational ground motion's behavior due to a double couple point source is analyzed based on the elastic theory. The behavior under investigation is the peak ground rotation rate and the static rotation.

Chapter 3, *Array experiment, deriving rotational rate from array data*, I show the comparison between array derived-rotation rate with rotation rate directly measured by a ring laser. The goal of this study is to discuss the effect of noise and uncertainties in the array observations and their relevance to the derivation of rotation. We restrict ourselves on analyzing only the vertical component of rotation rate.

Chapter 4, *Displacement, rotation, tilt: comparing seismic array observation with point measurements*, I present the application of rotational data, in addition with transverse component of the ground motion to derive the phase velocity and a possibility to determine the Love wave dispersion curve. The derivation of tilt data (horizontal component of rotation) are discussed briefly in the last Chapter.

Chapter 5, *Horizontal component of rotation or tilt*, I review the tilt measurements, instrumentations, and show the array-derived tilt.

Chapter 6, *Discussion and conclusion*, I give some concluding remarks and discuss further perspectives of rotational ground motion measurements.

2. Rotational ground motion

*“... , but as of this writing
seismology still awaits a suitable
instrument for making such
measurements.”*

(Aki & Richards, 2002)

In this chapter I will review the theory of rotational ground motions including the analytical study of rotation due to a double couple point source in infinite media, instrumental and observational aspects of rotational motions ¹.

2.1. Rotation due to a double couple point source: analytical study

For a homogeneous medium, rotational motions can be modelled analytically. As the Earth can be assumed to behave like an elastic material, especially under the application of small transient forces, we derive the rotational expression in the framework of classical elasticity theory. Assuming infinitesimal deformations, the displacement of a point x related to a new point $x + \delta x$ by (e.g. Aki & Richards (2002)) is

$$\begin{aligned}u(x + \delta x) &= u(x) + G\delta x \\ &= u(x) + \epsilon\delta x + \Omega\delta x \\ &= u(x) + \epsilon\delta x + \omega \times \delta x,\end{aligned}\tag{2.1}$$

¹This chapter is partly based on Cochard *et al.* (2006)

2.1 Rotation due to a double couple point source: analytical study

where G , ϵ , Ω are the gradient, strain, and rotation second order tensor, respectively, and the rigid body rotation is defined by

$$\omega = \frac{1}{2} \nabla \times u(x), \quad (2.2)$$

with $\nabla \times$ being the nabla operator. This shows that it is necessary to have three components of translation, six components of strain, and three components of rotation to fully characterize the change in the medium around point x .

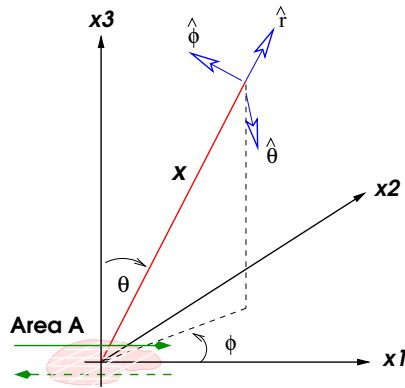


Figure 2.1: Cartesian and spherical polar coordinates for analysis of radial, and transverse components of displacement as well as rotation caused by a shear dislocation of area A and average slip $\langle \Delta u(t) \rangle$.

A point double-couple shear dislocation is the most successful model for earthquake sources. Assume a shear dislocation located in the center of a cartesian coordinate system x_1, x_2, x_3 , so that the fault lies in the (x_1, x_2) plane (Figure 2.1). In addition, we define polar coordinates r, θ, ϕ as specified in Figure 2.1. The slip direction is along the x_1 axis. Thus, the corresponding displacement field, $u(x, t)$ using the time dependent seismic moment $M_0(t) = \mu \langle \Delta u(t) \rangle A$, associated with a shear dislocation (Figure 2.1) parallel to a fault surface with area A , shear

2.1 Rotation due to a double couple point source: analytical study

modulus μ , and average slip $\langle \Delta u(t) \rangle$ across the fault is (Aki & Richards (2002)):

$$\begin{aligned}
 \bar{u}(x, t) = & \frac{1}{4\pi\rho} A^N \frac{1}{r^4} \int_{\frac{r}{v_s}}^{\frac{r}{v_p}} \tau M_0(t, \tau) d\tau \\
 & + \frac{1}{4\pi\rho v_p^2} A^{IP} \frac{1}{r^2} M_0\left(t - \frac{r}{v_p}\right) \\
 & + \frac{1}{4\pi\rho v_s^2} A^{IS} \frac{1}{r^2} M_0\left(t - \frac{r}{v_s}\right) \\
 & + \frac{1}{4\pi\rho v_p^3} A^{FP} \frac{1}{r} \dot{M}_0\left(t - \frac{r}{v_p}\right) \\
 & + \frac{1}{4\pi\rho v_s^3} A^{FS} \frac{1}{r} \dot{M}_0\left(t - \frac{r}{v_s}\right).
 \end{aligned} \tag{2.3}$$

The functions A in each term represent the radiation pattern given by

$$\begin{aligned}
 A^N &= 9 \sin 2\theta \cos \phi \hat{r} - 6(\cos 2\theta \cos \phi \hat{\theta} - \cos \theta \sin \phi \hat{\phi}), \\
 A^{IP} &= 4 \sin 2\theta \cos \phi \hat{r} - 2(\cos 2\theta \cos \phi \hat{\theta} - \cos \theta \sin \phi \hat{\phi}), \\
 A^{IS} &= -3 \sin 2\theta \cos \phi \hat{r} + 3(\cos 2\theta \cos \phi \hat{\theta} - \cos \theta \sin \phi \hat{\phi}), \\
 A^{FP} &= \sin 2\theta \cos \phi \hat{r}, \\
 A^{FS} &= \cos 2\theta \cos \phi \hat{\theta} - \cos \theta \sin \phi \hat{\phi},
 \end{aligned}$$

where \hat{r} , $\hat{\theta}$, and $\hat{\phi}$ are unit direction vectors in a spherical polar coordinate system for the source receiver geometry (Figure 2.1). Note that the superscripts N , I , and F are related to near field, intermediate, and far field terms respectively, while P and S denote P and S waves, respectively. In the far field, the radiation pattern consists of a radial component, proportional to $\sin 2\theta \cos \phi \hat{r}$ (Figure 2.2), and a transverse component, proportional to $\cos 2\theta \cos \phi \hat{\theta} - \cos \theta \sin \phi \hat{\phi}$ (Figure 2.3).

The positive sign in the far field P-wave radiation pattern shown in Figure 2.2 means that the dipole is directed outwards from the source and results in a compressional P-wave motion. The negative sign means the dipole is directed towards the source, resulting in a dilatational P-wave motion. The compressional and dilatational motions manifest themselves as upward and downward motion in the seimograms respectively. The central pair of arrows shows the sense of the shear dislocation. The strongest P-wave motion is expected in the middle of the four quadrants, at 45° angles to the fault plane (x_1, x_2) (Figure 2.1).

The far field S-wave radiation pattern follows the geometry shown in Figure 2.3. The central pair of arrows shows the sense of shear dislocation and the arrows

2.1 Rotation due to a double couple point source: analytical study

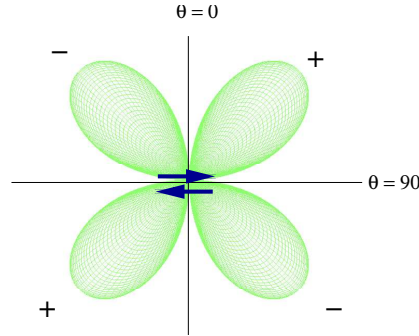


Figure 2.2: Far field P-wave radiation pattern in x_1, x_3 plane for radial component of displacement due to a double couple in plane x_1, x_2 .

on each lobe show the sense of direction of particle displacement associated with the lobe. The far field P and S-wave radiation patterns are rotated by 45° with respect to one another. The radiation pattern for intermediate and near field displacement involve both radial and transverse components. From Equation 2.3,

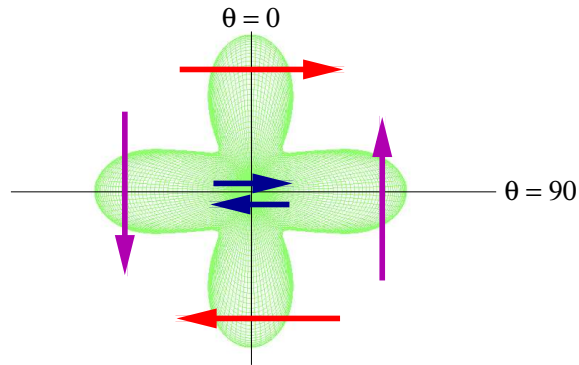


Figure 2.3: Radiation pattern of the transverse component of displacement due to a double couple. The blue arrow shows the sense of shear dislocation. The arrow in each lobe represent the direction of particle displacement associated with the lobe.

we can calculate the final static displacement field for a shear dislocation M_0 . This can be calculated by taking the limit of $\dot{M}_0(t-\tau)$, $M_0(t-\tau)$, and $\int_{\frac{r}{v_p}}^{\frac{r}{v_s}} \tau M_0(t-\tau) d\tau$

2.1 Rotation due to a double couple point source: analytical study

as $t \rightarrow \infty$, assuming that the seismic moment has a final constant value, $M_0(\infty)$. The result is (Aki & Richards (2002), p. 82)

$$u(x, \infty) = \frac{M_0(\infty)}{4\pi\rho r^2} \left[A^N \left(\frac{1}{2v_s^2} - \frac{1}{2v_p^2} \right) + \frac{A^{IP}}{v_p^2} + \frac{A^{IS}}{v_s^2} \right] \quad (2.4)$$

The rigid body rotation, then can be calculated by applying Equation 2.3 to Equation 2.2. We find

$$\begin{aligned} \omega(x, t) &= \frac{1}{2} \nabla \times u(x, t) \\ &= \frac{-A^R}{8\pi\rho} \left[\frac{3}{v_s^2 r^3} M_0 \left(t - \frac{r}{v_s} \right) + \frac{3}{v_s^3 r^2} \dot{M}_0 \left(t - \frac{r}{v_s} \right) + \frac{1}{v_s^4 r} \ddot{M}_0 \left(t - \frac{r}{v_s} \right) \right], \end{aligned} \quad (2.5)$$

where $A^R = \cos\theta \sin\phi\hat{\theta} + \cos\phi \cos 2\theta\hat{\phi}$ is the radiation pattern of the three components of rotation (the radial component is zero). The radiation pattern for transverse component of rotation is shown in Figure 2.4. The central pair of

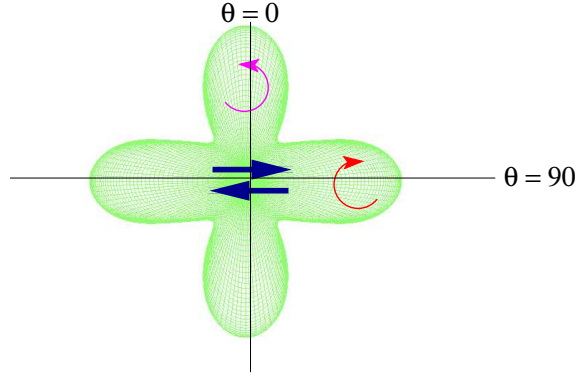


Figure 2.4: Radiation pattern of the transverse component of rotation due to a double couple point source. The arrow in each lobe represents the rotation of grains adjacent to the internal slip planes.

arrows shows the sense of shear dislocation, and arrows on the each lobe show the direction of particle rotation.

Based on Equation 2.3 and Equation 2.5 we can sketch the first motion on the seismogram and rotational sensor for any different location from a dislocation source (Figure 2.5). The first motion is the simplest way to study the geometry

2.1 Rotation due to a double couple point source: analytical study

of faulting during an earthquake, since the pattern of radiated seismic waves depends on the fault geometry. For this purpose we generate the seismogram based on equation 2.3 and 2.5 using a source signal defined as:

$$M_0(t) = \frac{1}{2} \operatorname{erf} \left(\frac{t - T_0}{T_0} \right) M_W \quad (2.6)$$

Note that M_0 is a function of time t and T_0 is the rise time. The parameter M_W is a measure of the size of an earthquake caused by fault slip. This value has a broad range from 10^{12} dyne-cm for microearthquakes to around 10^{30} dyne-cm for big earthquakes (Aki & Richards (2002)). The density of the medium is $\rho=2800$ kg/m³, the S and P wave velocities are $\beta=3000$ m/s and $\alpha = \sqrt{3}\beta$. The source is located at 10 km depth in the center of the study area.

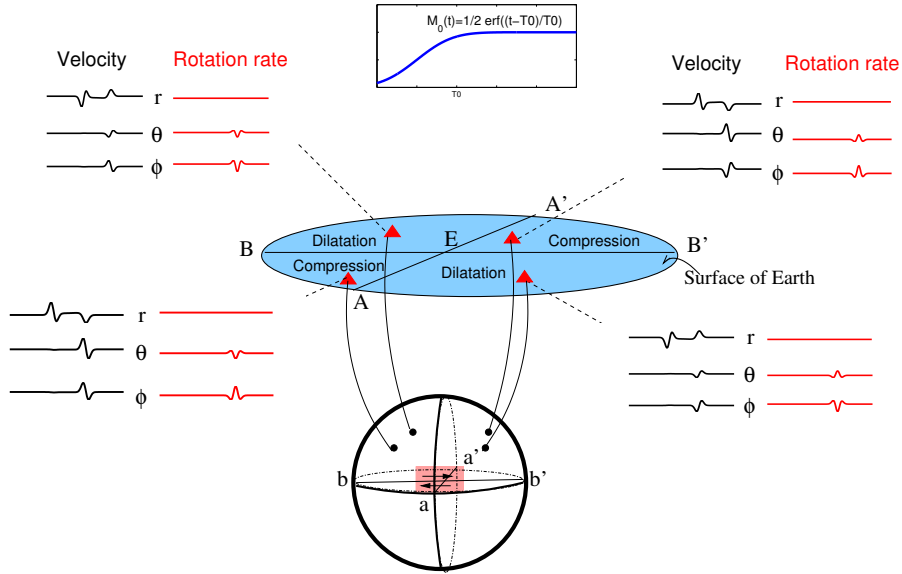


Figure 2.5: Normalized translational (black) and rotational (red) motions at seismometers located in various directions.

It should be noted that the upward motion of the P-wave is compressional and downward motion is dilatational. The rotations are zero at the P-wave front, and only start at the S-wave arrival and have no radial component. As in the translational component, this sketch shows that the first motion of rotational component can be used to determine the fault plane geometry.

2.1 Rotation due to a double couple point source: analytical study

For strong motion study, it is worth to represent the amplitude of the ground velocity in a peak ground motion map. It is used to derive the hazard map on a seismically-active area. In the next paragraph we will show the peak ground velocity as well as peak ground rotation rate calculated from Equation 2.3 and Equation 2.5. Again, the dislocation is in the x_1, x_2 plane as shown in Figure 2.1, and the source time function is in the form $M_0(t) = \frac{1}{2} \text{erf} \left(\frac{t-T_0}{T_0} \right) M_W$ with a moment $M_W = 3.2 \times 10^{20} \text{ dyne.cm}$ ($M \approx 3.0$) (Figure 2.6). The density of the medium is $\rho=2800 \text{ kg/m}^3$, the S and P wave velocities are $\beta=3000 \text{ m/s}$ and $\alpha = \sqrt{3}\beta$ respectively. The source is located at 10 km depth in the center of the study area.

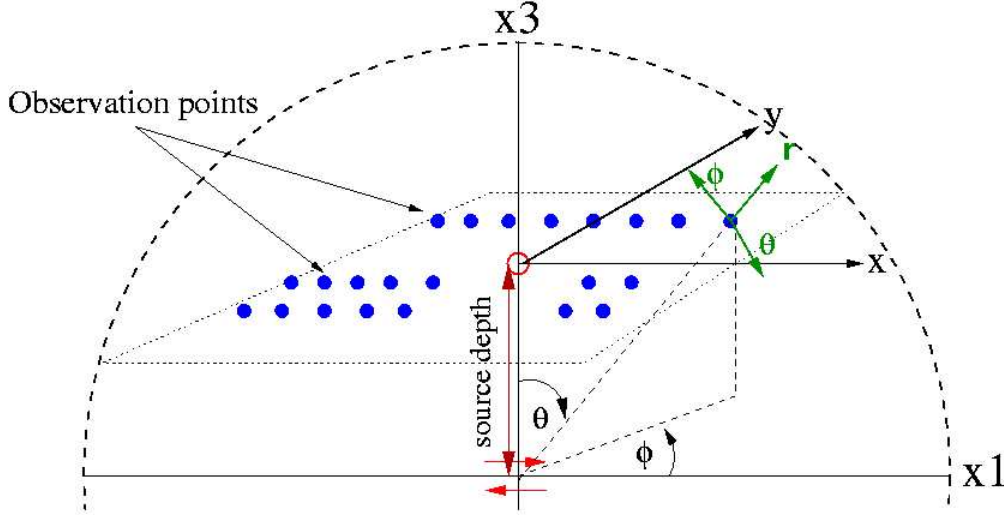


Figure 2.6: Simulation setup for showing the peak ground velocity and peak ground rotation. The spherical coordinate was used as in Figure 2.1. x and y represent the direction in x offset and y offset respectively.

In Figure 2.7, we show the contour plot of peak ground velocity (first row) and peak ground rotation rate (second row). We observe that the maximum of peak ground rotation rate is about $1.5 \times 10^{-9} \text{ rad/s}$ for the transverse component. This value seems quite small compared with the transverse component of translational motion which is about $2 \times 10^{-4} \text{ cm/s}$. However, as will be discussed in Chapter 4, rotations are proportional to acceleration divided by the phase velocity, thus, when we have smaller velocities, rotations became larger. Therefore,

2.1 Rotation due to a double couple point source: analytical study

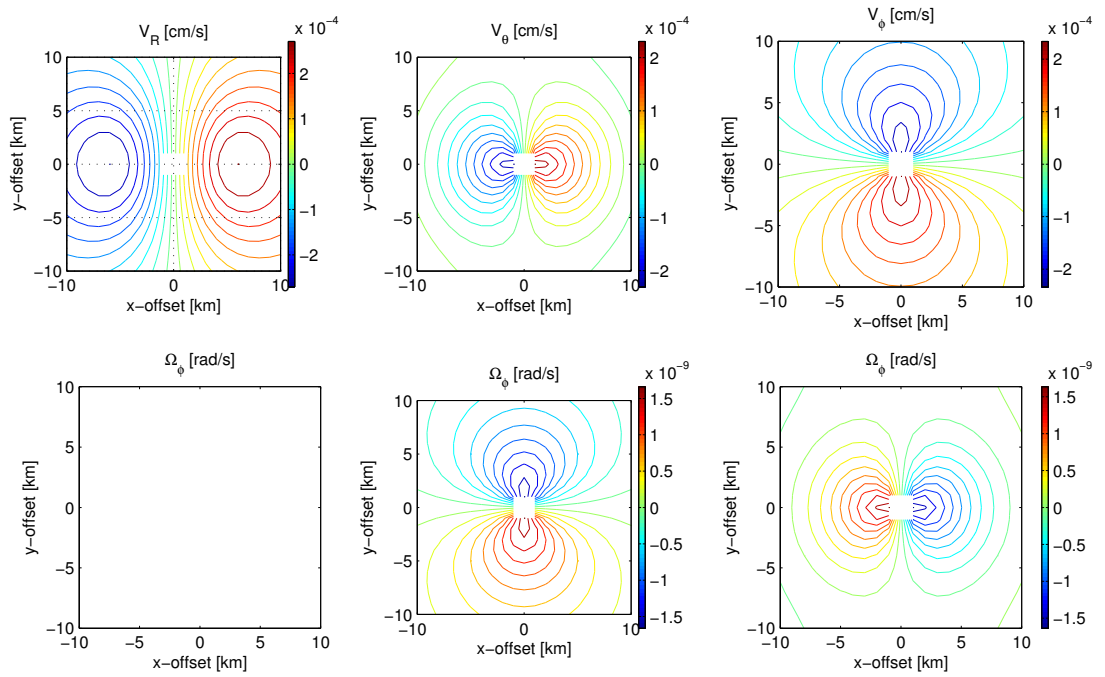


Figure 2.7: Contour plot of numerically computed peak ground velocity and peak ground rotation rate for 10 km deep double-couple point source of 10^{24} dyne. cm in an infinite homogeneous medium.

2.1 Rotation due to a double couple point source: analytical study

in case of a soft or unconsolidated sedimentary or fluid-infiltrated porous media, where the wave speed is low, the rotation may be large and could be responsible or contribute to structural damages.

The peak ground velocity and peak ground rotation rate (which is basically the cross section of Figure 2.7) are shown in Figure 2.8.

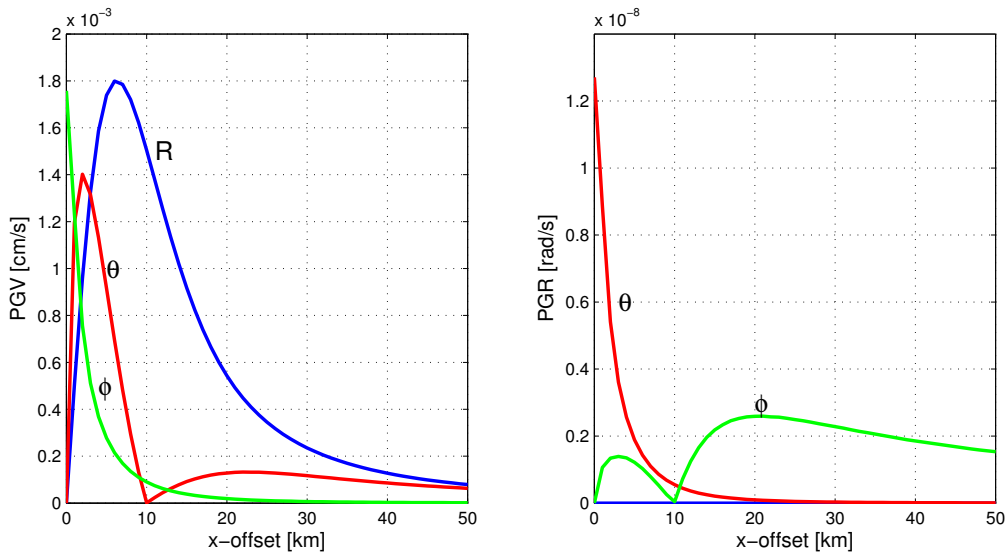


Figure 2.8: Cross section plot of peak ground velocity and peak ground rotation rate for an 10 km deep double-couple point source of 10^{20} dyne. cm in an infinite homogeneous medium.

Another important parameter especially for strong motion and crustal deformation study is static deformation and static rotation. From Equation 2.5, we can also calculate the final static rotation for a shear dislocation M_0 . In analogy with the static displacement case, it is calculated by taking the limit of $\dot{M}_0(t - \tau)$, $M_0(t - \tau)$, assuming that the seismic moment has a final constant value, $M_0(\infty)$. The result is

$$\begin{aligned} \omega(x, \infty) &= \frac{-A^R M_0(\infty)}{8\pi\rho r^3} \left(\frac{3}{v_s^2} \right) \\ &= \frac{M_0(\infty)}{8\pi\rho r^3} \left[-\frac{3}{v_s^2} \left(\cos\theta \sin\phi \hat{\theta} + \cos\phi \cos 2\theta \hat{\phi} \right) \right], \end{aligned} \quad (2.7)$$

2.1 Rotation due to a double couple point source: analytical study

which attenuates along any given direction(θ, ϕ) as r^{-3} . From Equation 2.4 and 2.7, we can plot the static displacement and static rotation map as a function of distance from the epicenter (Figure 2.9 and 2.10). In those figures, we plot numerically computed static displacement and static rotation for 10 km deep double-couple point source of 10^{24} dyne. cm in an infinite homogeneous medium. The maximum static deformation (0.1 cm) occurs in the radial component. The

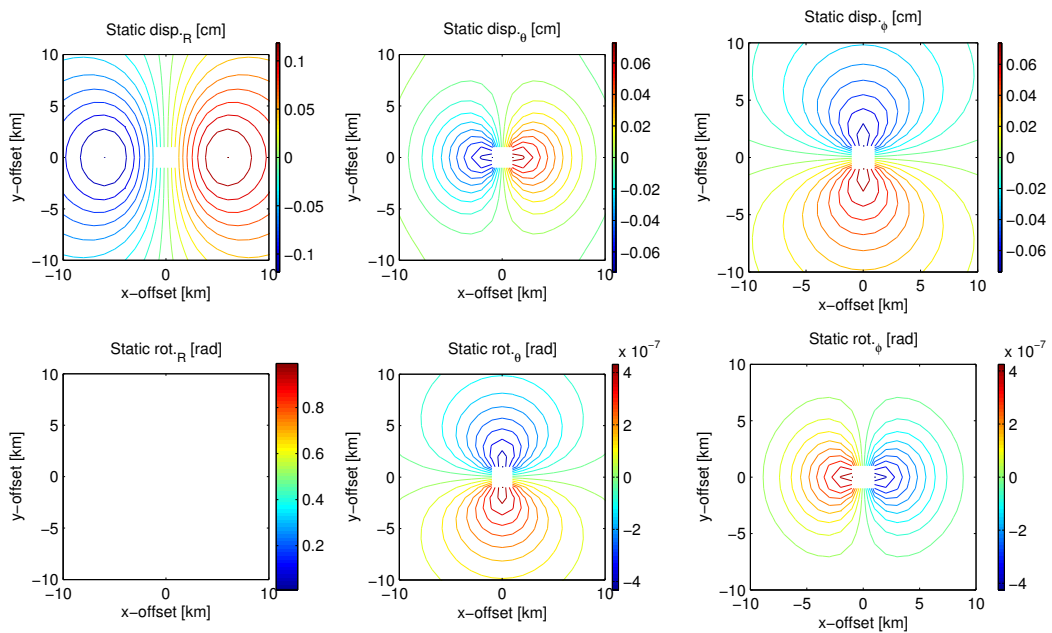


Figure 2.9: Contour plot of numerically computed static displacement and static rotation for an 10 km deep double-couple point source of 10^{24} dyne.cm in an infinite homogeneous medium.

static rotation is about 4×10^{-7} radians in both transverse and longitudinal components. The cross section of static displacement and rotation as a function of distance from the earthquake source is shown in Figure 2.10.

Further exercise for various magnitude and source depth including the strike slip double-couple point source or arbitrary configuration can be done by utilizing the analytical solution script (in matlab) that can be found in the DVD-ROM attached with this thesis.

2.1 Rotation due to a double couple point source: analytical study

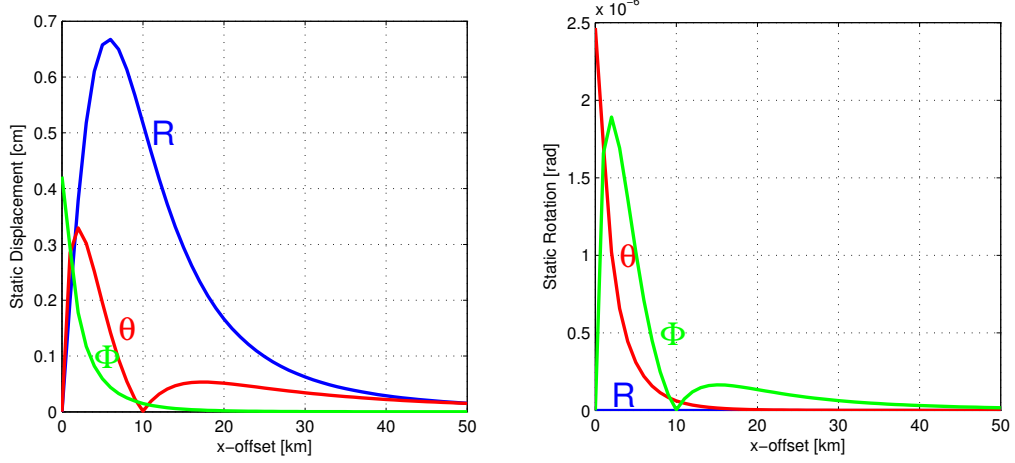


Figure 2.10: Cross section plot of static displacement and static rotation for an 10 km deep double-couple point source of M5.5 in an infinite homogeneous medium.

When analyzing the stress strain relation at the free surface, using a x_1, x_2, x_3 coordinate system, an important constraint is that the vertical component of the traction is zero. It implies that $\sigma_{i3} = \sigma_{3i} = 0$ and direct application of Hooke's law in a homogeneous, isotropic medium leads to

$$\frac{\partial u_x}{\partial z} = -\frac{\partial u_z}{\partial x}; \frac{\partial u_y}{\partial z} = -\frac{\partial u_z}{\partial y}; \frac{\partial u_z}{\partial x} = -\frac{\lambda}{\lambda + 2\mu} \left(\frac{\partial u_x}{\partial x} + \frac{\partial u_y}{\partial y} \right), \quad (2.8)$$

where λ and μ are the Lamé parameters.

Applying Equation 2.8 to Equation 2.2 we find that

$$\omega_x = \frac{\partial u_z}{\partial y}; \omega_y = -\frac{\partial u_z}{\partial x}. \quad (2.9)$$

Equation 2.9 shows that at the Earth's surface, the horizontal components of rotation correspond to tilt.

As a consequence, P waves generate horizontal rotation at the surface whereas they are irrotational in the bulk. There is an additional contribution to horizontal rotation due to P-to-SV converted waves at the surface (also due to the free surface boundary condition). It is still an open question what technology is best suitable for the various components of rotation. For the vertical component, the results presented here and in other studies suggest that the optical devices are the

way to go. Those optical devices could be advantageous compared to classical tiltmeters for the horizontal components as well (regardless of meteorological characteristics accuracy, sensitivity, etc. which remain to be assessed): indeed, classical tiltmeters measure a change of angle with respect to the local vertical, determined by gravity; thus they cannot discriminate between true rotation and a pure change in the local gravity (e.g., due to mass redistribution).

2.2. Rotational sensors

In this section we briefly discuss various rotational sensors that have been used especially for geophysical applications.

2.2.1. Parallel seismograph

This measuring system consists of two antiparallel pendulum seismometers (TAPS) situated at a common vertical axis, one after the other with the distance L between the suspension axes (e.g., Moriya & Marumo, 1998; Solarz *et al.*, 2004; Teisseyre *et al.*, 2003). Intensive studies about this kind of rotational sensor was conducted by the Institute of Geophysics, Polish Academy of Science.

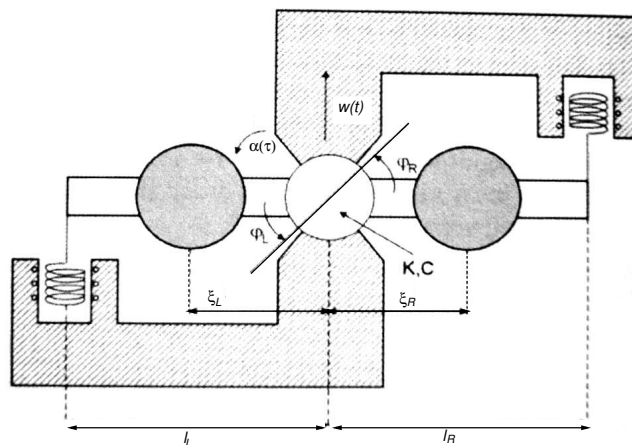


Figure 2.11: Two antiparallel seismographs developed in the Institute of Geophysics, Polish Academy of Science (Solarz *et al.*, 2004)

2.2 Rotational sensors

The schematic diagram of this system is shown in Figure 2.11. The symbol $w(t)$ and $\alpha(t)$ denote translation and rotation of the seismometer's bodies. The $\dot{w}(t)$ and $\dot{\alpha}(t)$ are obtained by convolving the recorded electromotive forces with the response functions of the seismometer. The basic principle of this system is explained below. Each single pendulum seismometer records the displacement velocity u , the displacement velocity derivative multiplied by the pendulum length ($l\dot{\partial}u/\partial y$), and the proper rotation $l\omega$. Thus those two opposite seismometer systems records simultaneously the two fields

$$u_L = u + l \left(\frac{\partial u}{\partial y} + \omega \right), u_R = u - l \left(\frac{\partial u}{\partial y} + \omega \right). \quad (2.10)$$

Teisseyre *et al.* (2003) define a new quantity called micro-displacement velocity tensor as a sum of the derivative of displacement velocity and the appropriate component of the tensor of real rotation as

$$\phi_{ik} = \frac{\partial u_i}{\partial x_k} + \omega_{ik}. \quad (2.11)$$

Therefore, the micro-displacement velocity tensor is related to the difference of records between the two opposite sensors (Equation 2.10) divided by $2l$

$$\phi_{ik} = \frac{\Delta u_i}{2l} = \frac{\partial u_i}{\partial x_k} + \omega_{ik}. \quad (2.12)$$

Thus, by knowing the displacement recorded by each seismograph the rotational component could be deduced by applying Equation 2.2.

The last relation is only valid when those two seismometer are equivalent (concerning the instrument response function). However, reliable rotation record can be obtained when the following condition is valid (Teisseyre *et al.*, 2003):

$$2l\Omega * R \gg \dot{U} * \Delta R + n. \quad (2.13)$$

Here R is the response function, the same for both seismometers, ΔR is the difference of those response functions, \dot{U} is the translational component of the ground motion, Ω is the rotation rate, l is the length of the pendulum and n is the noise from wave propagation and measurement. More comprehensive explanation about this system and further signal processing technique to improve the performance of this system can be found in Solarz *et al.* (2004).

This system has been tested by recording several seismic events Observed in Ojcow Observatory, Poland and L'Aquila Observatory, Italy. For the Silesian seismic event (11 July 2001, 18:50), recorded at a distance of about 60 km with magnitude about M1.5 the maximum rotation rate amplitude is about $3.5 \times 10^{-8} rad/s$ (Teisseyre *et al.*, 2003).

However, this sensor still needs to be compared with the other type of rotation sensors or with the transverse acceleration at collocated position to study performance and limitation.

2.2.2. Solid state sensor

The second type of rotational sensor is a solid state rotation sensor which consists of a microminiature double-ended quartz tuning fork and supporting structure (GyroChip). This GyroChip was fabricated chemically from a single wafer of monocrystalline piezoelectric quartz (similar to quartz watch crystals). It uses vibrating quartz tuning forks to sense rate, and acting as a Coriolis sensor, coupled to a similar tines as a pickup to produce the rotation rate output signal. The concept of using a vibrating element to measure rotational velocity based on the Coriolis² principle has also been recognized a few decades ago. The GyroChip along with their support flexure and frames are batch fabricated from thin wafers of single-crystal piezoelectric quartz.

The piezoelectric drive tines are driven by an oscillator to vibrate at a precise amplitude, causing the forks to move toward and away from one another at a high frequency. This vibration causes the drive fork to become sensitive to angular rate about an axis parallel to its tines, defining the true input axis of the sensor (Figure 2.12). By using the Coriolis effect, a rotational motion about the sensor's longitudinal axis produces a DC voltage proportional to the rate of rotation. The use of piezoelectric quartz material simplifies the active element, resulting in exceptional stability over temperature and time. The drive tines, which constitute the active portion of the sensor, are driven by an oscillator circuit at a precise amplitude that causes the tines to move toward and away from one another at a

²The Coriolis effect is named for the French physicist and mathematician Gustave Gaspard de Coriolis (1792-1843)

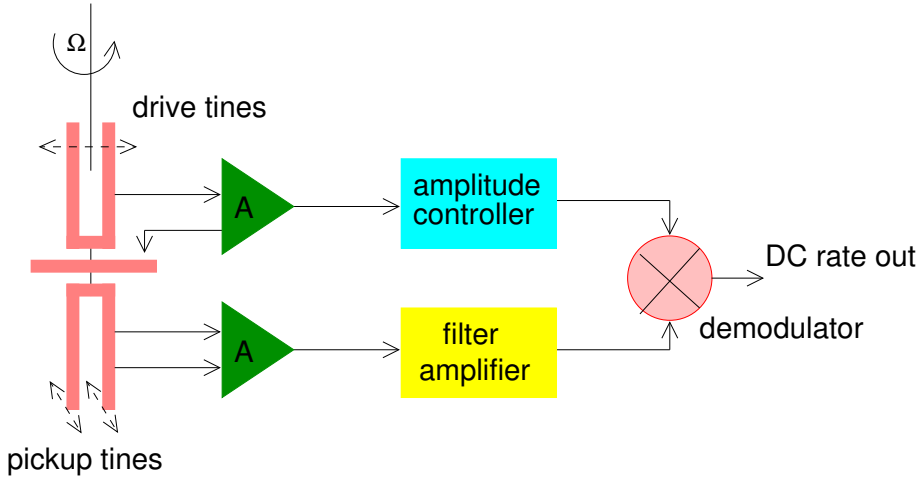


Figure 2.12: Solid state GyroChip schematic diagram. It contains a vibrating quartz tuning fork to sense rate, and acting as a Coriolis sensor, coupled to a similar tines as a pickup to produce the rotation rate output signal.

high frequency (see Figure 2.12). Each tine will have a Coriolis force acting on it of:

$$F_{Coriolis} = 2m(v_r \times \Omega_i), \quad (2.14)$$

where m is tine mass, v_r is instantaneous radial velocity, Ω_i is input rate. This force is perpendicular to both the input rate and the instantaneous radial velocity.

The two drive tines move in opposite directions; the resultant forces are perpendicular to the plane of the fork assembly and in opposite directions as well. This produces a torque that is proportional to the input rotational rate.

The pickup tines, being the sensing part of the sensor, respond to the oscillating torque by moving into and out of plane, producing a signal at the pickup amplifier. After amplification, those signals are demodulated into a DC signal proportional to the sensor's rotation.

This sensor is broadly used as stabilization and navigation system. It has been used as instrument in cars, satellites, air planes and other land vehicles. However, for a geophysical application, this sensor is limited to measuring large ground rotational motion close to the earthquake source (e.g., Nigbor, 1994; Takeo, 1998).

As an example, the Gyro Chip (QRS14-Type solid state Micromachined Angular Rate Sensor) has a resolution about 0.04 deg per second. It used as a platform stabilisation, damping/control system, GPS augmentation, camera stabilisation, robotics and autonomous vehicle control.

2.2.3. Ring laser gyroscope

The third type of rotation sensor is a ring laser gyroscope. A ring-laser gyro, in the original design, contains a ring-shaped cavity. Other types of cavity shape are triangular or square-shaped. The cavity is filled with a mixed gas, with circulating light beams generated by a laser. It measures the Sagnac beat frequency of two counter-propagating beams (Stedman, 1997) (See Figure 2.13). This beat frequency δf is directly proportional to the rotation rate Ω around the surface normal \hat{n} of the ring laser system as given by the Sagnac equation

$$\delta f = \frac{4A}{\lambda P} \hat{n} \cdot \Omega, \quad (2.15)$$

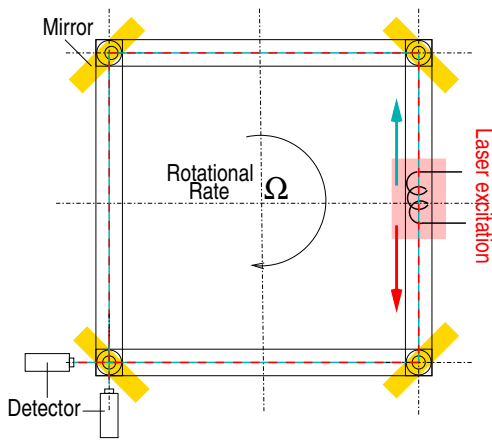


Figure 2.13: Ring laser measurement principle. Two counter-rotating laser beam interfere to generate a beating when the system rotates with respect to the normal. The beating frequency is directly proportional to rotation rate.

where Ω is the full rotation velocity, including the Earth rotation rate and local ground rotation, P is the perimeter of the ring, A the area, and λ is the laser wavelength. It is clear from Equation 2.15, that the ring laser is not sensitive to translational motion, but sensitive to deformation, since A , P and λ are influenced by the deformation. A ring is also sensitive to the projection of Ω onto \hat{n} . The sensitivity of a ring laser is proportional to the physical dimension (perimeter, area) and also depend on mirror quality. For seismological applications, this scaling factor $(4A/\lambda L)$ must be made much larger than

for commercial ring lasers. For example, the 4 by 4 meters square ring laser "G" installed in Wettzell, Germany has a resolution for the measurement of rotation

rates of $\delta f = 9 \times 10^{-11} \text{rad/s}$. This very high sensitivity is good enough for detecting both small near-field and teleseismic earthquake events.

The ring laser gyroscope was developed in the 60s and 70s for commercial, space and military navigation purposes. Commercial aircrafts are using this instrument because it provides a higher accuracy and reliability than other mechanical and fiber optic gyroscope technologies, and the fact that they do not need any moving mechanical parts. Since a ring laser is an active interferometer in which the sensitivity of this instrument arises from the dependency of the laser frequency from the cavity length, the important requirement for this device is the mechanical stability (Schreiber *et al.*, 2005). In order to operate in the monomode lasing regime, the variations of the cavity length must not exceed one wavelength (633 nm), which sets very high demands to the rigidity of the laser beam contour. As the fluctuation of temperature and pressure must affect the cavity length, therefore the environmental conditions at the location of the ring laser must kept within tight limits (temperature variation less than 0.5 degree and pressure change less than 10 hPa).

Several types of ring laser gyroscopes have been developed mainly for Earth science applications in the past years. The first generation of ring laser (named "C-I") was installed in the Department of Physics University of Canterbury, New Zealand during 1988-1990. This ring laser system has a nearly square optical cavity with an area of 0.7547 m^2 and a perimeter of 3.477 m. It uses a Helium-Neon gas mixture to fill the cavity and has two modes lasing at 633.0 nm with frequency of 473.6 THz. The performance of this kind of ring laser is reported by Stedman *et al.* (1995).

The ring laser "C-II", was the second generation of the ring laser gyro installed in the Cashmere Cavern in 1997 as part of a collaboration between The Bundesamt für Kartographie und Geodäsie, Frankfurt and Forschungseinrichtung Satelliten Geodäsie Wettzell, Technische Universität München, University of Canterbury, Christchurch, New Zealand and Marsden Fund of the Royal Society of New Zealand. It has a monolithic construction, as for an aircraft gyro, within a solid piece of Zerodur $1.2 \text{ m} \times 1.2 \text{ m} \times 0.18 \text{ m}$. It has an optical cavity with an area of 1.0 m^2 with new engineering improvement including ultra-high vacuum bonding between metal flanges and Zerodur (Stedman, 1997, Schreiber,

2.2 Rotational sensors

1997,1998). Zerodur is a glass ceramic with an extremely low thermal expansion coefficient ($\alpha \sim 5 \times 10^{-9} K^{-1}$). The cavity contains a He-Ne gas mixture and has one mode in each direction lasing at 633.0 nm. It now routinely delivers Earth rotation measurements at several parts per billion precision. The Ring laser "G", was a very large and the most precise ring laser which was installed at Wettzell, 150 km north of Munich, Germany during September 1998 to July 2001. It has a $16 m^2$ area with 16 m perimeter and is stably engineered in Zerodur (Figure 2.14). "G" has been installed inside a pressure vessel in a purpose-built laboratory 5



Figure 2.14: "G" ring laser installed at Wettzell.

metres underground. The Ring laser "UG-1" is the largest active ring laser gyroscope in the world installed in Cashmere Cavern, Christchurch New Zealand. The laser cavity has perimeter 77 m and area $367 m^2$. The He-Ne laser operates with 633 nm wavelength. It is much more sensitive to detect the rotational effects from earthquakes and from other sources.

Table 2.1 shows the range of sensitivity afforded by the most sensitive existing large Ring laser gyros (RLGs). Ring laser gyros can be used as the stable elements

2.2 Rotational sensors

Table 2.1: Sensitivity of various ring laser gyroscope.

Ring laser	Area [m ²]	Sensitivity [$\frac{rad}{s\sqrt{Hz}}$]	rel. error [$\frac{1}{day}$]	Drift [$\frac{o}{h}$]
C-II	1	7.2×10^{-10}	7.5×10^{-6}	$< 4.5 \times 10^{-5}$
G	16	9.1×10^{-11}	5.6×10^{-8}	$< 1.8 \times 10^{-6}$
UG1	367	7.3×10^{-12}	6.6×10^{-7}	$< 1.5 \times 10^{-3}$

(for one degree of freedom each) in an inertial reference system. The advantage of using a RLG is that there are no moving parts. Compared to the conventional spinning gyro, this means there is no friction, which in turn means there will be no inherent drift terms. Additionally, the entire unit is compact, lightweight and virtually indestructible, meaning it can be used in aircraft. Unlike a mechanical gyroscope, the device does not resist changes to its orientation.

A special ring laser system named "Geosensor" has been developed mainly for seismological applications in Wettzell, Germany (Figure 2.16). Figure 2.15 shows a block diagram of the principal structure of the GEOsensor.

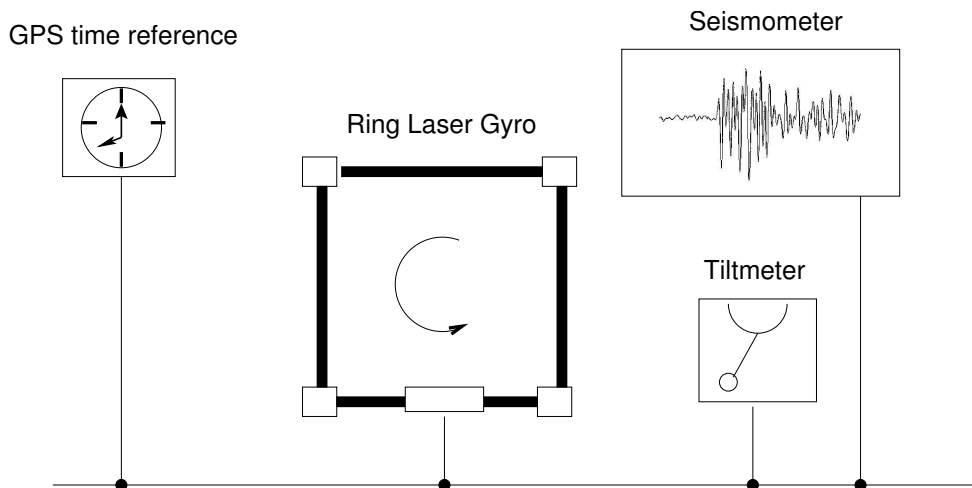


Figure 2.15: Block diagram of the principal structure of the GEOsensor

It is equipped with additional major instruments, (1) three components of

broadband seismometer for the measurement of linear displacements, (2) tiltmeter for monitoring the changes in the ring laser orientation (3) GPS for the data acquisition timing systems. It samples with 20 Hz sampling rate using a frequency demodulation technique.

Several seismic events have been recorded by this sensor ranging from hundred km of distance to several thousand of km distance (e.g., Igel *et al.*, 2007; Schreiber *et al.*, 2005). The performance of this sensor for seismological application can be tested by comparing them with array-derived rotation rate and the transverse acceleration. In principle, based on Equation 2.2, the rotation rate could also be derived from translational component recorded at several locations (seismic array).

This will be discussed in more detail in Chapter 3. Moreover, the transverse acceleration should be in phase with rotation rate for a certain earthquake event. More explanation about the rotation vs transverse acceleration relationship can be found in Chapter 4.

Among the other rotation sensors, ring laser is the state of the art in rotational sensor. However, ring laser instruments have limitations, i.e. they are sensitive to local disturbance (for example noise, temperature, pressure).

2.3. Applications

2.3.1. Geodesy, Earth rotation, polar motion

The measurement of the Earth's rotation by using the very-long-baseline interferometry (VLBI) has been recognized as the most powerful geodetic technique since last two decades. The VLBI measures the time differences in the arrival of microwave signals from extragalactic radio sources received at two or more radio observatories. The advantages of using VLBI technique, compared with other techniques such as satellite-laser-ranging (SLR) or Global Positioning System (GPS), is the unique strength of being able to observe the geometrical orientation of the rotating Earth relative to the inertial space. the VLBI data contain the information of:

1. The rotational speed, free from uncertainties suffered by satellite techniques due to their orbit drifts. These data yield the length-of-day (LOD) variation (used conveniently when the temporal sampling is longer than 1 day) or the universal-time (UT) variation (for sub-daily sampling where LOD loses its meaning.)
2. The rotational axis orientation, in both nutation and polar motion. In conventional terminology, nutation (including precession) are variations of the axis orientation relative to the inertial space, while polar motion is that relative to the terrestrial frame. Satellite techniques are unable to see nutation as can VLBI (because VLBI refers to the celestial frame), whereas VLBI can see polar motion as can satellite techniques (as the VLBI antennas are fixed on the terrestrial frame.)



Figure 2.16: "Geosensor" Ring laser installed in Wettzell, Germany

In the beginning, ring lasers were developed for measuring the Earth's rotation and tide. As we can see from Equation 2.15, the beat frequency between two counter circulating laser beam is directly proportional to total rotational velocity. Therefore, rotational motion due to Earth's rotation is always included in the measurements. Comparing with the commonly used method (VLBI), the use of ring lasers will be more practical since it doesn't need a global network.

An Earth tide signal at the lunar tidal period of 12 hours 25 min has been detected in the Sagnac frequency record of the C-II ring laser 30 m underground at Christchurch, New Zealand (Schreiber *et al.*, 2003). Its amplitude, one part per million of the Earth rotation signal, is much greater than the value of 40 parts per billion expected. Tiltmeter records show that a substantial part of this amplification is geophysical, the lunar component of tilt having an amplitude of

the order of 0.1–0.2 μrad , principally because of ocean loading of Banks Peninsula. The joint records also show effects on the Sagnac frequency associated with cavern deformation under ambient pressure and temperature change and with long-period waves in cavern tilt.

2.3.2. Geodynamics, static rotation

In the past years, the monitoring of Earth crust movement as well as fault creep is carried out with Interferometric Synthetic Aperture Radar (InSAR), GPS network measurement or broad band seismic network (e.g., Bennett *et al.*, 1996; Lyons & Sandwell, 2003; Trampert *et al.*, 2003). However, as mentioned in the previous section, to fully characterize the ground displacement, we need a six degree of freedom ground motion, including rotational component. Although the effect of rotational motion induced by earthquakes is small, for a long time duration, or in a case of in the near the earthquake source, this value will give significant contribution to overall ground deformations.

Hudnut *et al.* (2004) have combined the Global Positioning System (GPS) and Inertial Measurement Unit (IMU) as an earthquake early warning system. The IMU includes the rotational sensor for monitoring the rotation rate as well as static rotation induced by earthquakes. The GPS/IMU system can provide direct Damage Map and will be useful for autonomous, robust and real-time reliable structural health monitoring for large buildings and other engineered structures.

2.3.3. Seismology and earthquake engineering

Rotational (or torsional) motions play an important role in earthquake engineering studies especially in connection with the building response. Spatially varying multiple ground excitations produce both lateral and rotational (torsional) structure responses (Newmark, 1969). The lateral and torsional modes are uncoupled for symmetric building and the torsional mode is excited only because of the nonuniform ground motions (Hao & Duan, 1995). The lateral and torsional modes are coupled if the structure is asymmetric, that is center of stiffness differ from centers of floor mass. In addition, the local rotational motion may appear to be due to wave propagation in heterogeneous soil layers at the site. By knowing

the complete translational and rotational motion at such a site it can help to better understand the effects of the complete ground motion on structures. The effects of torsional response and or coupling of motions may remarkably change the site amplification characteristics at the site. Therefore, it is an important task to investigate the site amplification characteristics for both translation and rotations. Furthermore, knowledge of directional dependence of site response may aid in the design of critical facilities and predicting the dominant direction of damage at the site.

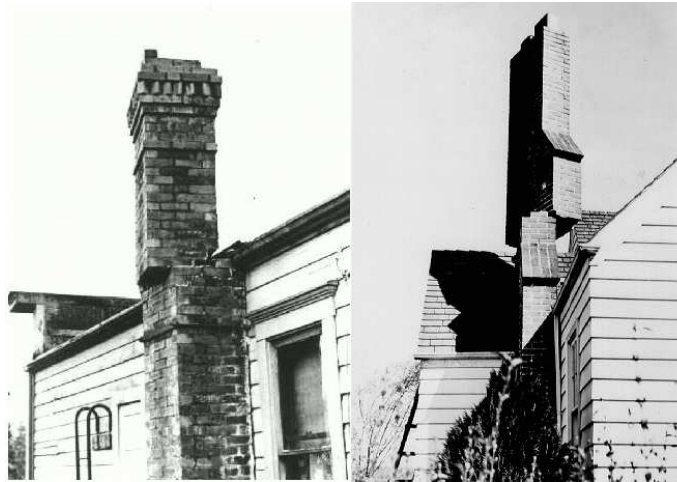


Figure 2.17: Building damage after a strong earthquake, that may be caused by rotational motion. Left photo is courtesy of the Geological Survey of Canada. Right photo Edwards, 1999.

The rotational effect of earthquakes to structural damage is an interesting research topic in earthquake engineering. In earthquake engineering, the rotational component of the ground motion is derived by applying array measurement techniques.

Rotational motion as well as horizontal ground motion coupling affects the calculation of site effect response. Ghayamghamian & Matosaka (2003) studied the effects of rotational motion to site effect response. They showed that rotational motion was responsible for the splitting of peaks in their resonance frequencies and low amplification values. However, the rotational motion is observed us-

ing indirect method (array technique). Therefore, direct recording of rotational motions using rotation sensors will help to estimate this effect more accurately.

Legrand (2003) showed that the representation of a finite source in the earthquake source modeling is more informative by including the rotational part that may derived from rotational motions. He also mentioned that the description of the finite source via seismic moment tensor is neglecting the rotational part that actually must be taking into account.

2.4. Observations

During the last decades, ground rotational motions have been observed by rotational sensors. Nigbor (1994) reported the successful recording of ground rotational motion induced by a non-proliferation experiment at the Nevada Test Site using a solid state rotation sensor. A maximum peak rotational velocity was reported about $2.2^\circ/s$ (0.038 rad/s). The amplitude of ground rotational motion ($0.1^\circ/s$ was observed during M3.5 event centered about 8 km from the site. With the same type of sensor, Takeo succeeded in measuring ground rotational motion during an earthquake swarm at March 1997 in offshore Ito in Izu Peninsula, Japan. The maximum rotational velocity was reported to be about $2.6 \times 10^{-2} \text{ rad/s}$. Rotational ground motions induced by teleseismic event have been reported by several investigators (e.g., Igel *et al.*, 2005; McLeod *et al.*, 1998; Pancha *et al.*, 2000; Stedman *et al.*, 1995) using ring laser technology.

2.5. Conclusion

The rotational part of earthquake-induced ground motion has basically been ignored in the past decades, compared to the substantial research in observing, processing and inverting translational ground motions, even though there are theoretical considerations that suggest that the observation of such motions may indeed be useful and provide additional information.

As in the translational component, the rotational component of ground motion can be modelled both analytically (for a simple case) or numerically. Numerical calculations can be done by extending the translational code inserting the

calculation of the curl of displacement or velocity that is usually done in the evolution subroutine for finite difference methods. Furthermore, this modeling could be used to explore rotational ground motion characteristics as well as study the earthquake source process.

The solid state rotation sensor and parallel-type seismograph have been used for recording ground rotation motion. However, they can only measure the ground rotational motion near the earthquake source. Furthermore, those sensor should be tested by comparing with other kind of rotation sensor or by comparing with transverse acceleration to test their consistency. Therefore, sensor developments in the past years focused on the development and refinement of optical instruments, particular using laser technology. The ring laser has been proven to have consistent rotation result and the capacity to measure the earthquake ranging from several hundred of kilometers distance to some thousand kilometers with a broad range of magnitude. Their consistency has been verified by comparing with the transverse acceleration. Nowadays, the ring laser gyroscope is the state of the art in rotational sensor. It provides several advantages and high resolution compared with other rotational sensors.

Even though the full benefits of the determination of rotational motion in Earth science are still under investigation, recent analysis suggest that it may increase the understanding of earthquake source process and refine the understanding of the Earth structure.

3. Array experiment, deriving rotational rate from array data

"A bigger problem has been the difficulty of deciding whether an instrument is making useful measurements or not, and more particularly how to compare the results from one instrument to those from another."

(Agnew, 1986)

In this chapter I present for the first time a comparison of rotational ground motions derived from array data with those observed directly with a ring laser³. The goal of this study is to discuss the effect of noise and uncertainties in the array observations and their relevance to the derivation of rotation. We restrict ourselves on analyzing only the vertical component of rotation rate as this is the only component we are currently measuring with ring laser technologies. Other component (ie. horizontal) are discussed in Chapter 5.

3.1. Introduction

With the availability of rotational data from a ring laser instrument, the question of direct vs. array-type of measurements becomes of interest in seismology, earthquake physics and geodesy. Study about array-derived rotation rate have been done by several investigators since several years ago (e.g., Bodin *et al.*, 1997;

³This chapter based on Suryanto *et al.* (2006)

Huang, 2003; Spudich *et al.*, 1995). However, to the best of our knowledge, a special study to compare directly the array-derived rotation rate with rotation rate recorded by rotational sensor was never done before.

This study will have –at least– two important aspects. First, it will be the first study that show directly the comparison of array-derived rotation rate with direct measurement of rotation rate. Second, it also becomes the first ”performance test” for the ring laser in order to see whether this instrument consistently records seismogenic rotational ground motions in the required frequency band (frequencies up to 1 Hz for teleseismic wave fields).

Further, we investigate the influence of various effects on array-derived rotation rate using synthetic array data. We will first present a synthetic study, in which we investigate the influence of various effects on array derived rotation rate. These effects are (1) unwanted signals (i.e., noise) in the horizontal components of translation, (2) uncertainty in seismometer calibration, and (3) uncertainty in station coordinates. Finally, we show the direct comparison of the vertical component of array-derived rotation rate with the ring laser gyroscope record for the M 6.3 Al Hoceima, Morocco, earthquake of February 24, 2004.

3.2. The array experiment

Following the successful observation of fully consistent rotational motions (Igel *et al.*, 2005), a mobile seismic array experiment with eight stations (S1, S2, S3, S4, S5, S6, S7, and S8) was installed around the geodetic station Wettzell, Southeast Germany. A ninth station was located in the geodetic station itself ($12^{\circ}52'44''$ E, $49^{\circ}08'39''$ N), where a broadband seismometer (station WET, part of the German Regional Seismic Network, GRSN) is situated. The ring laser is located at a distance of approximately 250 m from the broadband seismometer. The radius of the seismic array is about 1.5 km, centered at station WET. The shallow subsurface structure consists of metamorphic rock basement superimposed by glacial till. The location of the array is shown in Figure 3.1.

Each seismic station consists of a three-component velocity sensor (Le3D-5s) having a flat response in ground velocity between 0.2 and 40 Hz, and a

3.2 The array experiment

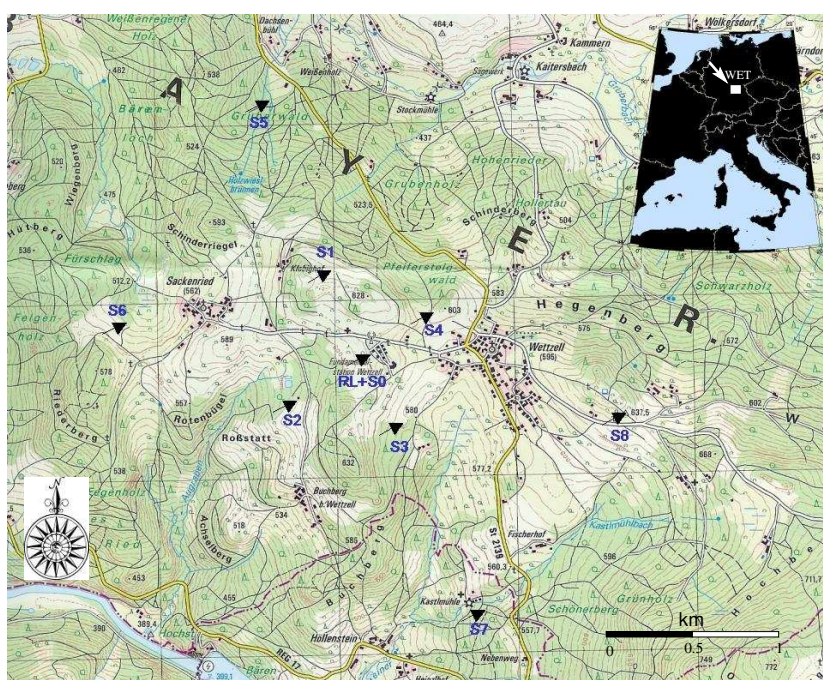


Figure 3.1: Location of the array experiment. The ring laser and GRSN (German Regional Seismic Network) broadband station (WET) are located at the center of the array marked by a triangles. The ring laser and the broadband seismometer are separated by approximately 250 m.

3.2 The array experiment

400V/m/s generator constant. A 24-bit three-channel digital recorder (Lennartz-Marslite/HD complemented by 3.5" removable SCSI hard drives) was used to record the data. The sampling rate was 62.5 Hz and GPS time synchronization was achieved every 15 minutes. The experiment was running from December 2003 until early March 2004. The seismometers were buried in soft forest ground (Figure 3.2) or they were deployed on outcropping large igneous rock boulders (Figure 3.3).



Figure 3.2: Station S1 located near a farm with the sensor was buried with a bottom depth about 50 cm.

The GRSN (WET) station is equipped with a STS-2 with a flat response of the ground velocity from 8.33 mHz (120 s) to 50 Hz, and a generator constant of $2 \times 750 \text{ V/m}/\sqrt{\text{s}}$. The data are recorded with a sampling rate of 80 Hz.

The ring laser instrument, called "G", consists of a He-Ne gas laser with a ultrahigh vacuum quality cavity enclosing an area of 16 m². The vertical component of rotation rate is recorded by this instrument with a sampling rate of 4 Hz. The G ring laser has a resolution of $9 \times 10^{-11} \text{ rad/s/Hz}$ (Schreiber *et al.*, 2003). Further information on the ring laser instrument is given in Schreiber *et al.* (2005).



Figure 3.3: Station S4 is located on outcropping large igneous rock boulders.

Several teleseismic earthquake events were observed during this experiment. The parameters of those events are given in Table 3.1. However, very few of these events were recorded with high signal to noise ratio by both the ring laser system and the seismic array. We focus here on the event with the highest signal-to-noise ratio.

3.3. Data and data processing

The continuously recorded data was converted to GSE format, segmented in 1-hour files, and archived on DVDs. The software package PITSA (Scherbaum & Johnson, 1992) was used to process the digital recorded data. Note that not all of those events are well recorded by the array's seismometers (Table 3.1).

Unfortunately the ring laser was not performing properly during some parts of the experiment, especially in December 2003.

Among those events, a specific one was selected for analysis, which happened on 24/02/2004 at 02:27:46.2 (GMT). According to news reports, the earthquake caused 628 casualties, and more than 2500 building collapsed. The epicenter

3.3 Data and data processing

Table 3.1: Parameters of the earthquakes recorded by the array during the experiment. Unfortunately the ring laser was not performing properly during December 2003.

Date	Time (UTC)	M_w	Lat.	Lon	Ring laser	Array
21.12.2003	07:40:45.8	6.6	00.769 S	20.601 W	X	noisy
22.12.2003	19:15:56.0	6.6	35.706 N	121.102 W	X	✓
25.12.2003	07:11:11.5	6.5	8.416 N	82.824 W	X	✓
26.12.2003	01:56:52.4	6.6	28.995 N	58.31 E	noisy	✓
26.12.2003	21:26:4.0	6.8	22.273 S	169.314 E	X	noisy
27.12.2003	16:01:0.0	7.3	22.015 S	169.766 E	X	✓
27.12.2003	22:38:1.8	6.7	21.672 S	169.835 E	X	noisy
05.02.2004	21:05:4.0	7.0	03.613 S	135.538 E	✓	noisy
07.02.2004	2:42:35.0	7.3	04.003 S	135.023 E	noisy	✓
21.02.2004	2:34:42.7	6.6	58.425 S	14.963 W	noisy	noisy
24.02.2004	2:27:46.2	6.4	35.142 N	3.997 W	✓	✓

3.3 Data and data processing

was located about 10 km south of Al Hoceima near the village of Aït Kamra (35.235° N, 3.963°W), about 295 km North-East from Rabat, Morocco. This earthquake occurred near the eastern end of the Rift mountain belt, which is part of the diffuse boundary between the African and Eurasian plates. The distance between the epicenter and the seismic network was about 2055 km (18.5 deg). The estimated rupture dimension was about $10 \times 10 \text{ km}^2$ with a moment magnitude of $M_w=6.2$ for the first event (Stich *et al.*, 2005). This earthquake was recorded simultaneously by the array stations S1-S8, the broadband station (WET) and the ring laser. The array and broadband data are corrected for the instrument response and deconvolved to a uniform seismometer with a corner frequency of 0.02 Hz. This is the most critical process during this experiment since we want to have true ground displacement value. The instrument response correction process significantly change the waveform of the recorded seismic signal especially from the Le3D sensor (Figure 3.4).

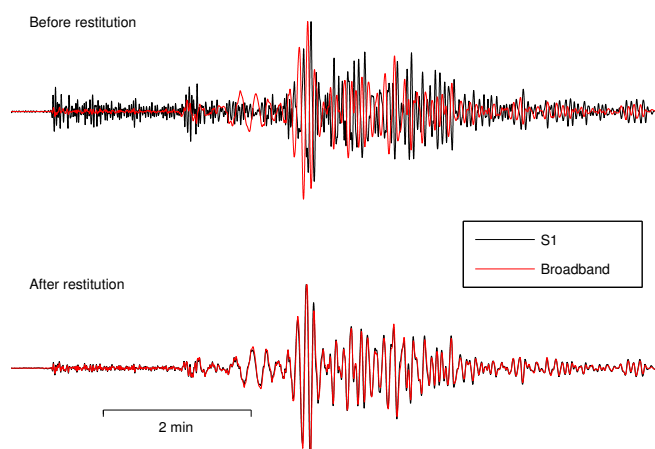


Figure 3.4: Comparison of normalized velocity seismograms for the M6.4 Al Hoceima Morocco earthquake recorded by S1 and broadband station. Significant change of waveform after corrected for the instrument response is clearly shown. All the seismograms are bandpass filtered from 0.03 Hz to 0.3 Hz.

Figure 3.5 shows the horizontal components of velocity seismograms after corrected for the instrument response, including broadband (WET) data for the Al

3.3 Data and data processing

Hoceima event. All the seismograms, including the broadband data are bandpass filtered from 0.03 to 0.5 Hz.

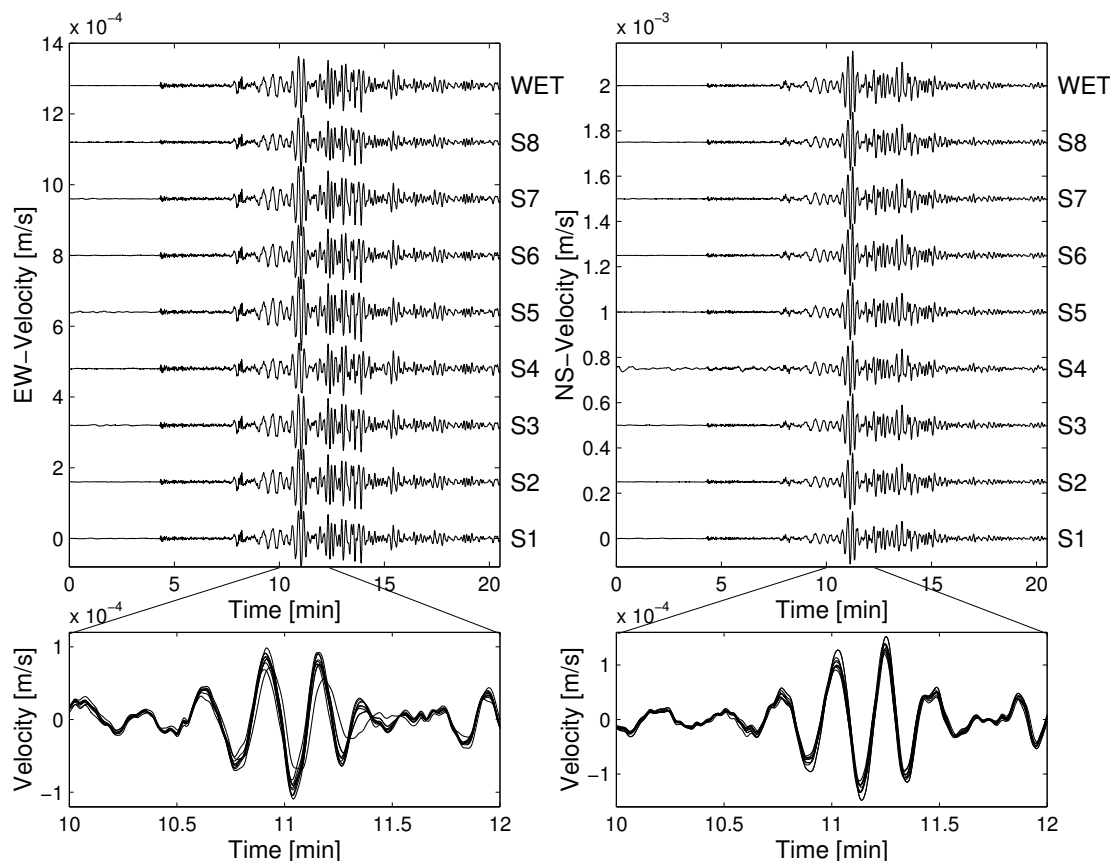


Figure 3.5: True amplitude velocity seismograms for the M6.4 Al Hoceima Morocco earthquake of February 24, 2004, recorded by the array. A superposition of all seismograms in a 2-minute time window is shown in the lower part. All the seismograms, including the broadband seismogram (WET, top), are corrected for the instrument response and bandpass filtered from 0.03 Hz to 0.5 Hz.

Note that, for this study, only the horizontal components from the array data were used. As expected, there is considerable match in amplitude and waveform between the array seismograph and the broadband sensor. The maximum amplitude of the velocity was about 0.8×10^{-4} and 1.2×10^{-4} m/s for East-West and North-South components, respectively.

3.4. Deriving rotation from seismic array data

The relation between rotational and translational motions is obtained through the application of the curl operator $\nabla \times$ to the seismic wave field $\vec{v}(x, y, z)$ by:

$$\begin{pmatrix} \omega_x \\ \omega_y \\ \omega_z \end{pmatrix} = \frac{1}{2} \nabla \times \vec{v} = \frac{1}{2} \begin{pmatrix} \partial_y v_z - \partial_z v_y \\ \partial_z v_x - \partial_x v_z \\ \partial_x v_y - \partial_y v_x \end{pmatrix}. \quad (3.1)$$

This implies that - in principle - the rotational component can be estimated if we are able to calculate the spatial derivative of ground velocity. As is well known from numerical mathematics, partial derivatives can be approximated introducing information from two or more points sampling the vector field and solving an approximate system of linear equations. In what follows, we will restrict ourselves to the vertical component of rotation, as it is the component the ring laser is measuring. The simplest method to approximate the derivatives of the horizontal components of motion is to subtract two recordings of ground displacement (velocities, acceleration) and divide by their distance (finite difference approximation). This can be done especially when the points are distributed regularly in an ideal cross shaped array (e.g., Huang, 2003). In this thesis we apply a standard geodetic method to estimate the static displacement for calculating the space derivatives. This has been previously used by Spudich *et al.* (1995) to study the dynamic deformation induced by the M7.4 Landers earthquake of June 28, 1992, derived from the UPSAR array in Parkfield, California. This method has also been used by Bodin *et al.* (1997) to study dynamic deformations of shallow sediments in the Mexico basin.

We briefly describe this method in the following. At the free surface boundary, with the assumption of spatially uniform displacement gradient it can be shown that the displacement gradient matrix G , at each time point, can be estimated from ground displacement u_i ($i = 1..N$) recorded at N stations by solving the set of equations:

$$d_i = GR_i$$

$$= \begin{pmatrix} \partial_x u_x & \partial_y u_x & \partial_z u_x \\ \partial_x u_y & \partial_y u_y & \partial_z u_y \\ \partial_z u_x & -\partial_z u_y & -\eta(\partial_x u_x + \partial_y u_y) \end{pmatrix} R_i, \quad (3.2)$$

where, $\eta = \lambda(\lambda + 2\mu)$, λ and μ are the Lamé parameters, $d_i = u_i - u_0$, $R_i = r_i - r_0$, u_i , r_i , and u_0 , r_0 , are the displacements at the coordinates of the i^{th} station and the reference station (subscript o) respectively. At least three stations have to be used to determine the displacement gradient using this method. Assuming the array stations were located at the same elevation, the vertical component of rotation rate can be obtained by solving the equation (3.2) using three stations (S_i, S_j, S_k):

$$\omega_z = \frac{1}{2A} ([b_i u_y^i + b_j u_y^j + b_k u_y^k] - [c_i u_x^i + c_j u_x^j + c_k u_x^k]), \quad (3.3)$$

where A is the area bounded by the station S_i , S_j and S_k , $b_i = (y_k - y_j)/2$, $c_i = (x_k - x_j)/2$, and b_j , c_j , etc., can be achieved by letting $i \rightarrow j \rightarrow k \rightarrow i$. Here (x_i, y_i) , (x_j, y_j) and (x_k, y_k) are coordinates of stations S_i , S_j and S_k , respectively.

When more than three stations are used, the equation (3.2) can be solved using a least - squares procedure. More detailed explanations about this method can be found in Spudich *et al.* (1995).

3.5. Test on synthetic data

One of the key questions in this study is to understand the effect of various sources of uncertainties in the array observations on the array-derived rotational ground motions. The method described above is therefore first tested against a synthetic array data set. Complete theoretical seismograms for translations and rotations were calculated for a recent 3-D global tomography model S20RTS (Ritsema & Van Heijst, 2000), and a global crust model CRUST2.0 (Bassin *et al.*, 2000) for a point-source approximation of the Al Hoceima event. Seismograms were calculated using the spectral-element method (Komatitsch & Tromp, 2002a,b) that was extended to allow outputting the curl of the velocity-wave field (i.e., rotation rate). The large-scale numerical simulation was carried out with a spatial and temporal resolution allowing an accurate wavefield down to periods of 20 seconds (Schuberth *et al.*, 2004). The receivers were located at the same positions as our array's seismometers. To include the instrument effects, we filtered the synthetic data with the instrument response of the Le3D-5s seismograph.

3.5 Test on synthetic data

Figure 3.6 shows the restituted time histories of the horizontal components of the synthetic ground velocity and superposition of all traces in a short time window. Due to the epicentral distance (~ 2000 km) and the considered spatial

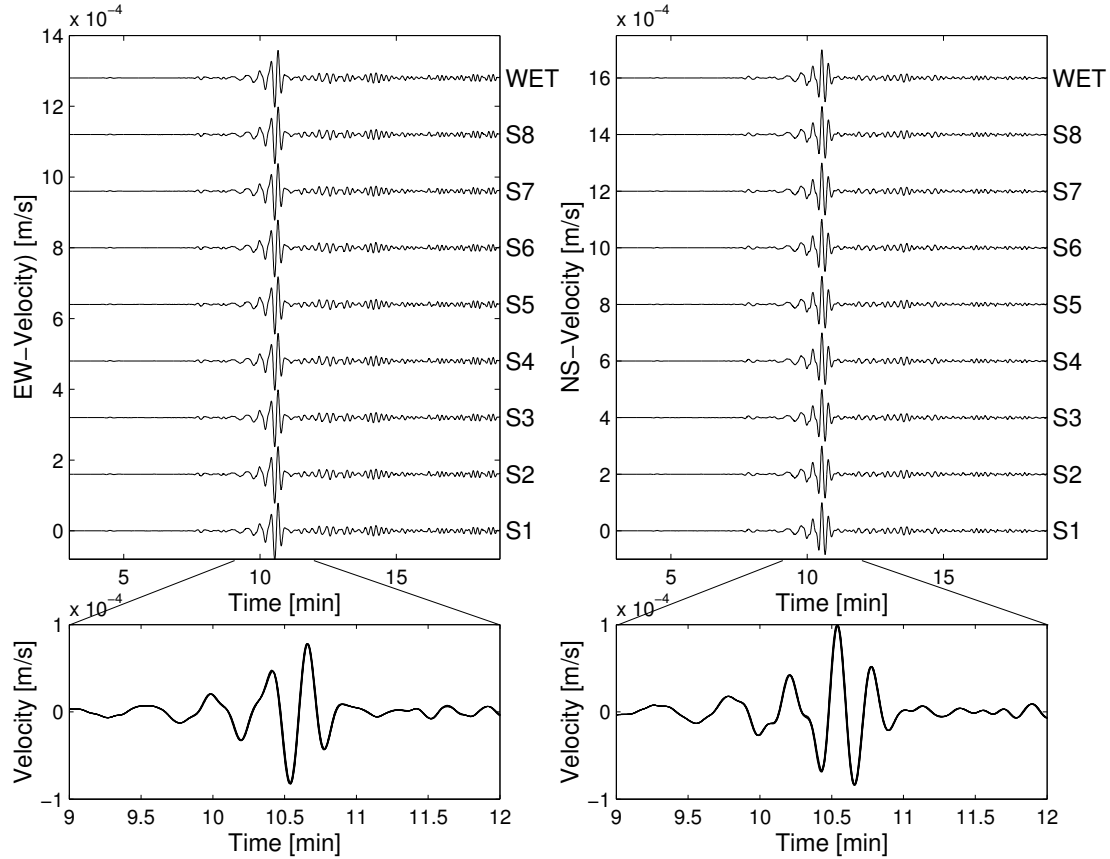


Figure 3.6: Synthetic velocity seismograms for the M6.4 Al Hoceima Morocco earthquake of February 24, 2004, for all the array's station as well as the central station (WET), calculated for a 3D mantle model (Ritsema & Van Heijst, 2000) and a recent crustal model (Bassin et al., 2000). The seismograms, calculated using the spectral element method (Komatitsch & Tromp, 2002a,b), have been lowpass filtered (< 0.05 Hz).

and temporal wavelengths, the waveforms are almost identical across the array. In the following we aim at investigating the effect of noise at some of the seismic stations. As the minimum number of stations to determine the spatial gradients

3.5 Test on synthetic data

is three, we choose to estimate rotations from (sub) triangular array section to investigate (1) the uniformity of the derived rotation and (2) to identify array sections with large uncertainties.

Figure 3.7 shows four pairs of the vertical component of array-derived rotation rate calculated using combinations of three stations of the outermost array stations (S5, S6, S7 and S8) with WET as the reference station (gray line) superimposed with synthetic rotation rate (black line) at the center of the array (WET). The normalized correlation coefficients (maxima) are given above the

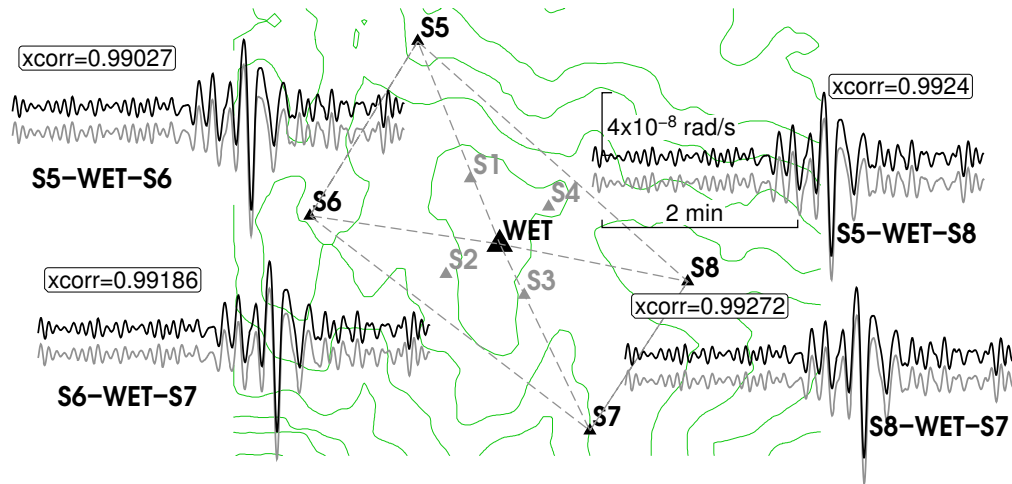


Figure 3.7: Synthetic test of uniformity of rotation rate across the array. Four pairs of the vertical component of rotation rate at the array center (black line) and array-derived rotation rate (gray line) calculated using three stations. Top right: stations WET, S5 and S8; bottom right: stations WET, S7 and S8; bottom left: stations WET, S6 and S7; top left: stations WET, S6 and S5. The normalized correlation coefficients are given for each trace pair.

trace pairs. The stations used to derive the vertical component of the array-derived rotation rate are given in the bottom of each trace pair. As expected with noise-free synthetics, the array-derived rotation rate matches almost exactly the rotation rate calculated at the central station WET (corr. coeff. > 0.99).

We now perform the same exercise with the observations of the Al Hoceima events. In Figure 3.8, the direct observations of rotation rate with the ring laser

3.5 Test on synthetic data

(black line) at the center of the array is compared with the array-derived rotation rate (gray line) using four different subtriangles. First, we observe that

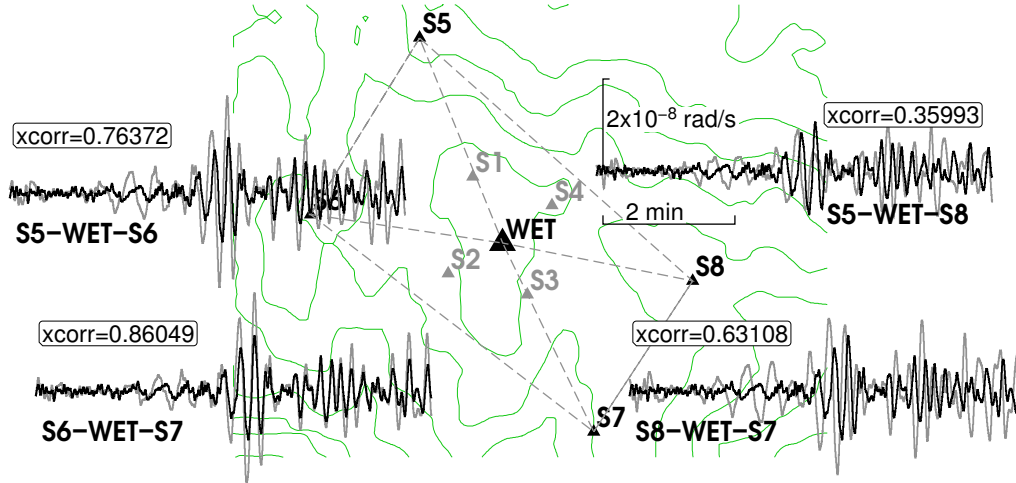


Figure 3.8: Non uniformity of array-derived rotation rate across the array for different triangles for real data. Top right: stations WET, S5 and S8; bottom right: stations WET, S7 and S8; bottom left: stations WET, S6 and S7; top left: stations WET, S6 and S5. The normalized correlation coefficients are given for each trace pair.

the array-derived rotation rate (using three stations only) varies substantially for the different triangles, suggesting considerable amount of noise, propagation, or site effects across the array. Second, in one subtriangle (S6-WET-S7) the phase match is quite good, but the amplitudes do not match well. In another one (S5-WET-S8) the amplitudes are closer to the direct measurements, but the phase match poorly in most parts of the seismogram. These observations suggest that different sources of noise (amplitude, phase, etc.) seem to affect the various array stations in our experiment.

Note that here we have deliberately decided to use only three (of nine possible) stations to determine rotations to highlight noise in the data. All stations are used in the final comparison. Before investigating specific noise effects more systematically, we demonstrate that - assuming random noise added to the synthetic array seismograms- we reproduce a behavior similar to what is seen in the

3.6 Various factors affecting the derivation of rotation rate

observations. To all seismograms we add 3% Gaussian white noise. Station 8, however is additionally perturbed by phase uncertainty in the E-W component. Phase uncertainty is introduced by perturbing each phase component randomly by up to 2% (of 2ϕ). The subtriangle determination of rotation rate with the phase-perturbed synthetics shown in Figure 3.9a now exhibits misfits similar to those of the observation in Figure 3.8. The subtriangle containing the phase perturbed seismometer (S8) compares poorly with the (noise-free) rotational signal at the center of the array. However, if we use all nine stations to determine the rotational signal, most of the random noise cancels out and the final array-derived rotation rate compares well with the (noise-free) rotational signal at the center of the array (Figure 3.9b). This indicates that random errors and /or systematic differences (randomly distributed) in parts of the array data may cancel out when sufficiently large number of stations is used. On the other hand using only three stations for array-derived rotations may considerably increase the uncertainties with respect to final rotation estimates.

3.6. Various factors affecting the derivation of rotation rate

In this section we will examine the effects of various levels of synthetic uncorrelated random noise, real background noise (extracted from observations), uncertainties in the position determinations and uncertainties in the seismometer gain on the array-derived rotation rate. The vertical component of rotation rate is calculated using all the data from the nine stations, as will be done when finally comparing with direct observations.

3.6.1. Synthetic noise

Clearly, intrinsic inhomogeneity of displacement gradient (e.g., due to topography, structural heterogeneity, etc.) might occur, but we restrict ourselves here to the study of random (nonsystematic) perturbations.

To study the effects of uncorrelated random noise in the array seismograms, we generate a Gaussian random signal with maximum amplitudes of 1%, 5%, and

3.6 Various factors affecting the derivation of rotation rate

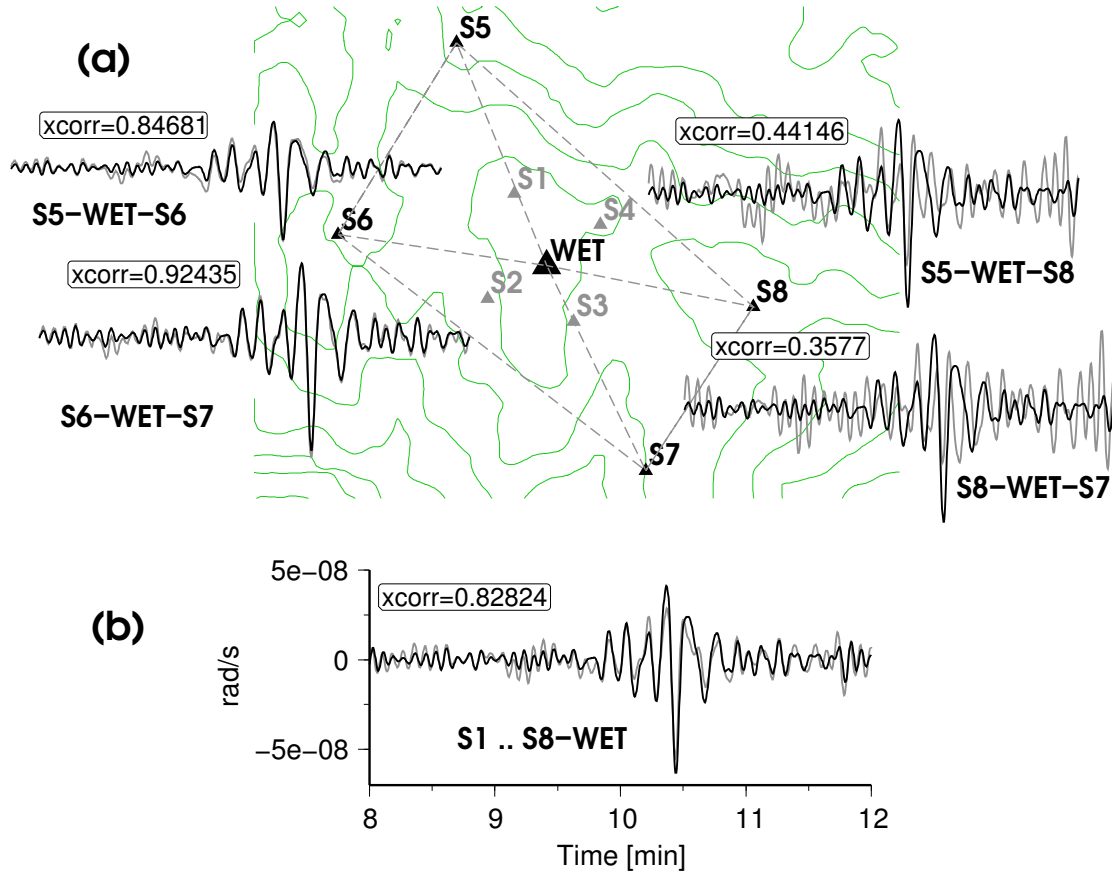


Figure 3.9: Non uniformity of array-derived rotation rate across the array for different triangles for synthetic data with a single phase-disturbed station (S8) and 3% of random noise added for all stations. a) Four pairs of the vertical component of ring laser data (black line) superimposed with array-derived rotation rate (gray line) calculated using three stations. Top right: stations WET, S5 and S8; bottom right: stations WET, S7 and S8; bottom left: stations WET, S6 and S7; top left: stations WET, S6 and S5. b) The vertical component of array-derived rotation rate (gray) is calculated from all eight stations (S1-S8) with WET station as reference. The normalized correlation coefficients are given for each trace pair.

3.6 Various factors affecting the derivation of rotation rate

10%, of the maximum amplitude of the horizontal component of the synthetic velocity seismograms. This random signal is added to the synthetic array data. The array-derived rotation rate from 25 random signal realizations is depicted in Figure 3.10 (gray) and compared with the noise-free exact rotation rate at the center of the array. The average root-mean-square (rms) difference of the array-derived rotation rate was 1.33%, 6.43%, and 12.87% for 1%, 5%, and 10% noise, respectively. With 10% noise the waveforms are severely distorted but the dominant phases are still well matched with peak amplitude errors similar to the noise percentage. With 5% noise the waveforms are affected by the low-frequency part of the random noise, while, with 1%, the differences between the curves is barely more than the thickness of the line.

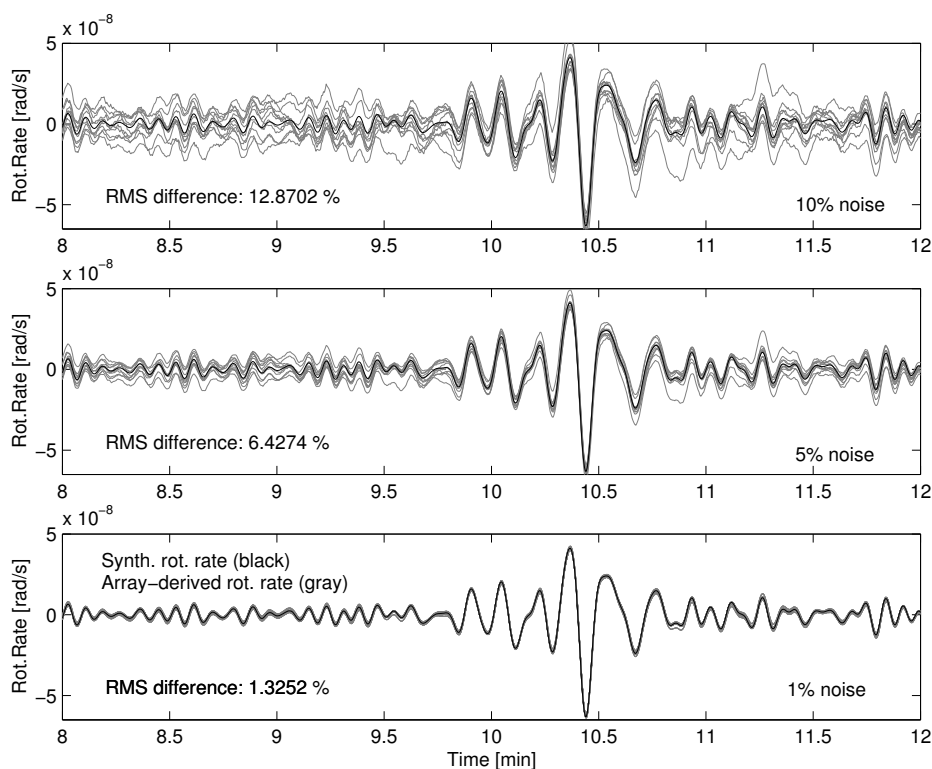


Figure 3.10: Vertical component of array-derived rotation rate from synthetic data with Gaussian random noise (with 25 noise realizations) (gray line), superimposed with the noise-free synthetic rotation rate (black line). The amount of noise is 10%, 5% and 1%, from top to bottom.

3.6.2. Real noise

The actual noise level in the observations can be estimated by taking signals prior to the first arriving energy of the event under investigation. In the following, noise signals are extracted from the observations some minutes before the first arriving energy for each of the nine stations. These signals are added to the synthetic array seismograms and the rotational signal is estimated and compared to the noise-free rotational signal at the center of the array. The background noise is on average about 3% of the peak amplitude of the velocity seismograms. The results are shown in Figure 3.11 (top). The rms-difference of the array-derived rotation rate with respect to the true signal is 3.58%. These results suggest that with the observed noise level – in the absence of other errors (e.g., systematic errors such as timing, filter problems, etc.) – it should be possible to derive the rotational signal from the array observations with similar certainty (within a few percent).

3.6.3. Uncertainty in seismometers' position

Array station coordinates are essential for the calculation of the array-derived rotational signal. In our experiment we use a portable GPS receiver for synchronizing the time and for the determination of the stations' coordinates. The problem with this kind of GPS is their low accuracy in position determination. In our experiment, the coordinate precision was affected by the nearby presence of buildings or trees. As a consequence, the uncertainty in seismometer's position in our experiment is several meters.

To estimate the effect of position uncertainties, we introduce random position errors from -30 to +30 meters in the x and y coordinates and calculate the rotation rate for 25 such realizations. The results are shown in Figure 3.11 (bottom). The average rms-difference of the array-derived rotation rate is 0.38%. From this we conclude that the uncertainties introduced through the GPS measurements are unlikely to deteriorate the final array-derived estimates of the rotational signal.

3.6 Various factors affecting the derivation of rotation rate

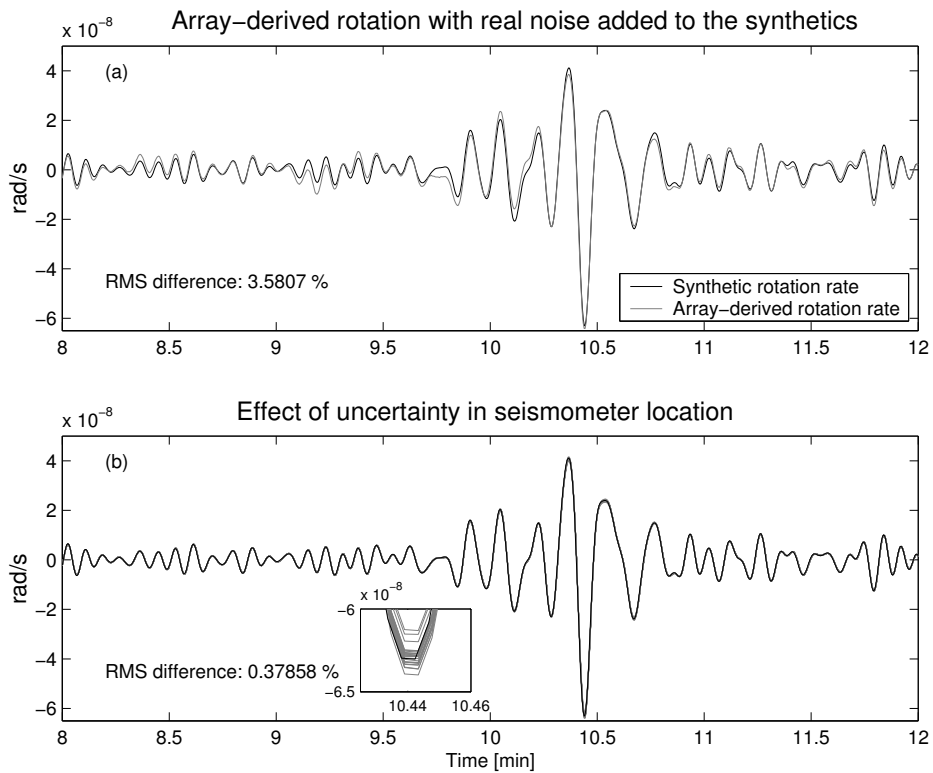


Figure 3.11: a) Vertical component of array-derived rotation rate from synthetic data with real noise taken from the observed seismograms several minutes before the event started; b) The effects of a ± 30 m error in seismometer position on the derivation of rotation rate for 25 realizations).

3.6.4. The effect of local soil condition and phase

The effect of local soil condition is playing an important role in the ground motion study. Near surface heterogeneities may introduce attenuation as well as amplification in the amplitude of the seismogram. To investigate the effects we randomly modify the overall amplitude of the synthetic data by a factor of 1%, 5%, and 10%. The calculated rotation rate from 25 realizations in each case is depicted in Figure 3.12. The rms-difference of the array-derived rotation rate is 1.14%, 3.67%, and 10.12%, for 1%, 5%, and 10% amplitude uncertainty in each of the array components, respectively. Even though this test is somewhat simplified, the results suggest that random (constant/static) amplitude errors are unlikely to alter the final results – given our array configuration – significantly.

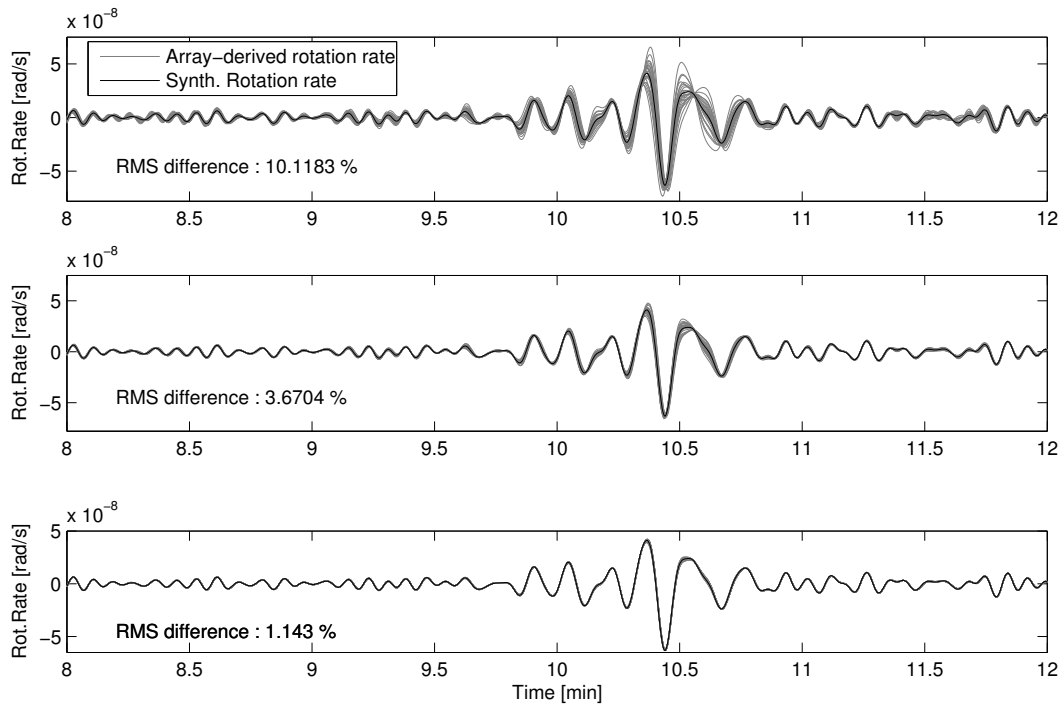


Figure 3.12: Vertical component of array-derived rotation rate for synthetic data with amplitude uncertainty of 10%, 5%, and 1% (top to bottom), from 25 realizations (gray lines) superimposed with synthetic rotation rate (black line).

3.6 Various factors affecting the derivation of rotation rate

Array-derived rotation rate assumes that the seismometers used in the experiment exhibit the same behavior (i.e. the same response function). The specific response function of the seismometers used here and the low frequencies considered here may potentially introduce phase uncertainties. In order to investigate this effect, we perturb the phase component of the all horizontal components of seismogram in the frequency domain by 0.5%, 1%, or 2% (with a percentage of 2π) of the phase components. The calculated rotation rate from 25 realizations in each case is depicted in Figure 3.13. The rms-difference of the array-derived rotation rate is 65.4%, 38.6%, and 15.5%, for 2%, 1%, and 0.5% phase uncertainty in each of the array components, respectively. Comparing with other noise effects, this uncertainty gives the most pronounced effects on the final results.

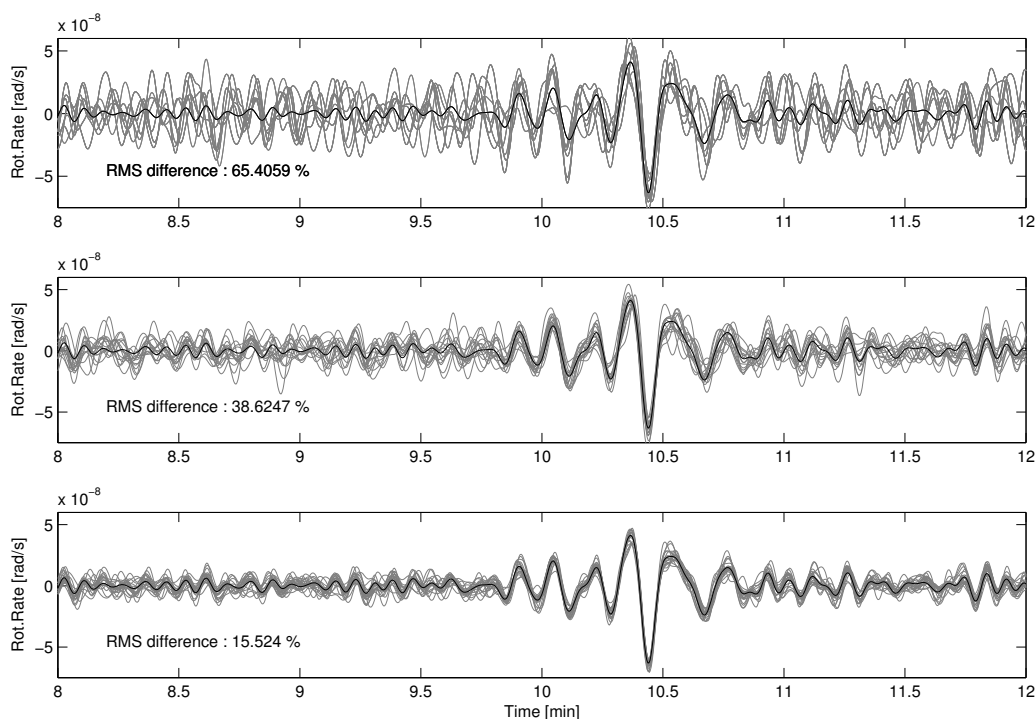


Figure 3.13: Vertical component of array-derived rotation rate for synthetic data with phase uncertainty of 10%, 5%, and 1% (top to bottom), from 25 realizations (gray lines) superimposed with synthetic rotation rate (black line).

3.7. Real data

Finally, we derive the array-derived rotation rate for the Al Hoceima event from the horizontal seismograms of all nine array stations (Figure 3.5). In Figure 3.14 we show the comparison between the array-derived rotation rate with ring-laser based direct measurements of the same wave field quantity. We stress here that the traces are compared with absolute amplitudes. The overall rms-difference is 3.72%. The maximum normalized correlation coefficients are given below each seismogram. The best correlation coefficient is 0.97 in the Love wave time window. In the early part of the seismogram, the fit is worse. This is probably due to the low amplitudes compared to the peak amplitudes of the Love wave train. In addition, this time window contains the highest frequencies and we expect the uncertainties to increase with frequency. The match between the direct and array-derived rotation rate is almost perfect in the three-minute time window containing the fundamental and higher mode Love waves with correlation coefficients above 0.95. The overall fit is worsening towards the end of the signal due to decreasing signal-to-noise ratio. The surprisingly good fit of those entirely different approaches to measuring the rotational part of the wave field confirms the quantitative results of the synthetic study, particularly the fact that the final similarity is obtained thanks to the relatively large number of seismic array stations given the observed noise levels.

3.8. Array-derived rotation rate versus transverse acceleration

It has been shown from Table 3.1, that during this experiment, only the data Al Hoceima event were available both from ring laser and from array. However, there are other events that were recorded relatively good signal-to-noise ratio with the array seismometer but not the ring laser instrument. Those events are the M6.6 Bam, Iran event at 26 December 2003 (Figure 3.15) and 7.3 Papua, Irian Jaya, Indonesia event at 07 February 2004 (Figure 3.16).

Even though, not all station records those event with a good signal-to-noise ratio, fortunately the station S2, S5, and S6 record those event quite well. With

3.8 Array-derived rotation rate versus transverse acceleration

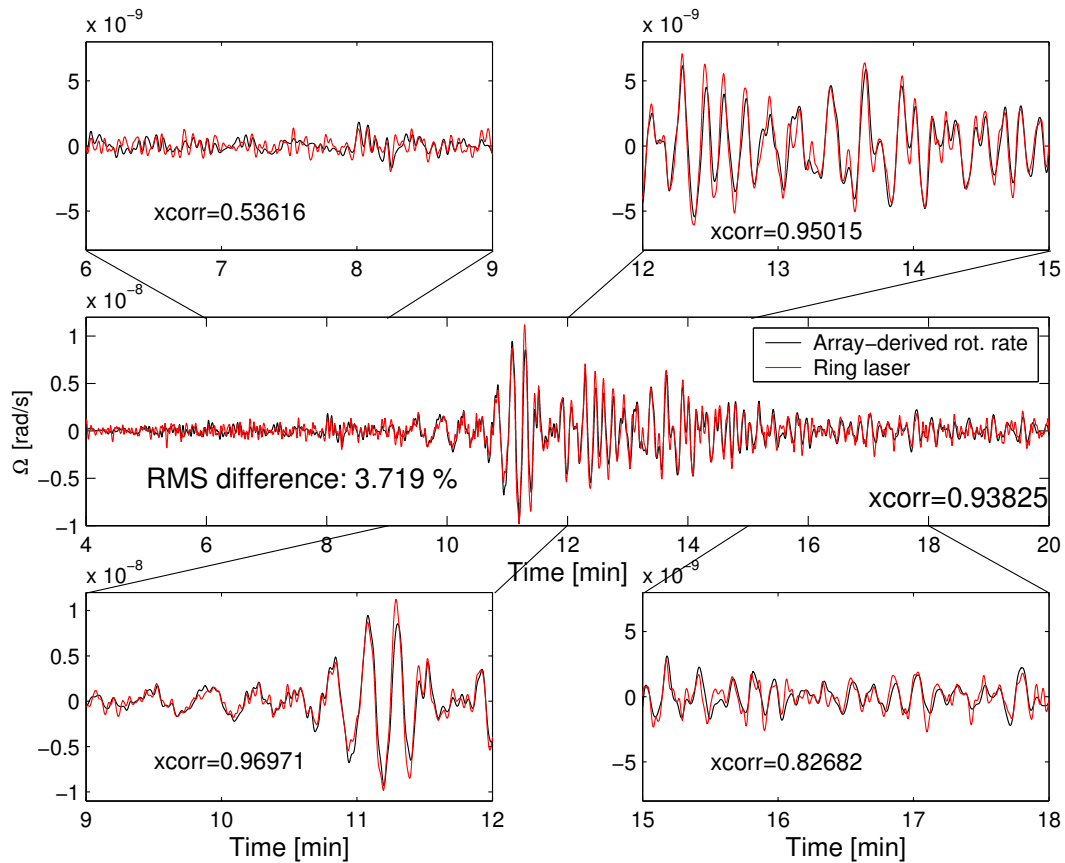


Figure 3.14: Vertical component of array-derived rotation rate from real array data set (gray line) superimposed with ring laser data (black line). Nine stations including the broadband data are used to calculate the array-derived rotational signal. Both traces are bandpass filtered from 0.03 Hz to 0.3 Hz

3.8 Array-derived rotation rate versus transverse acceleration

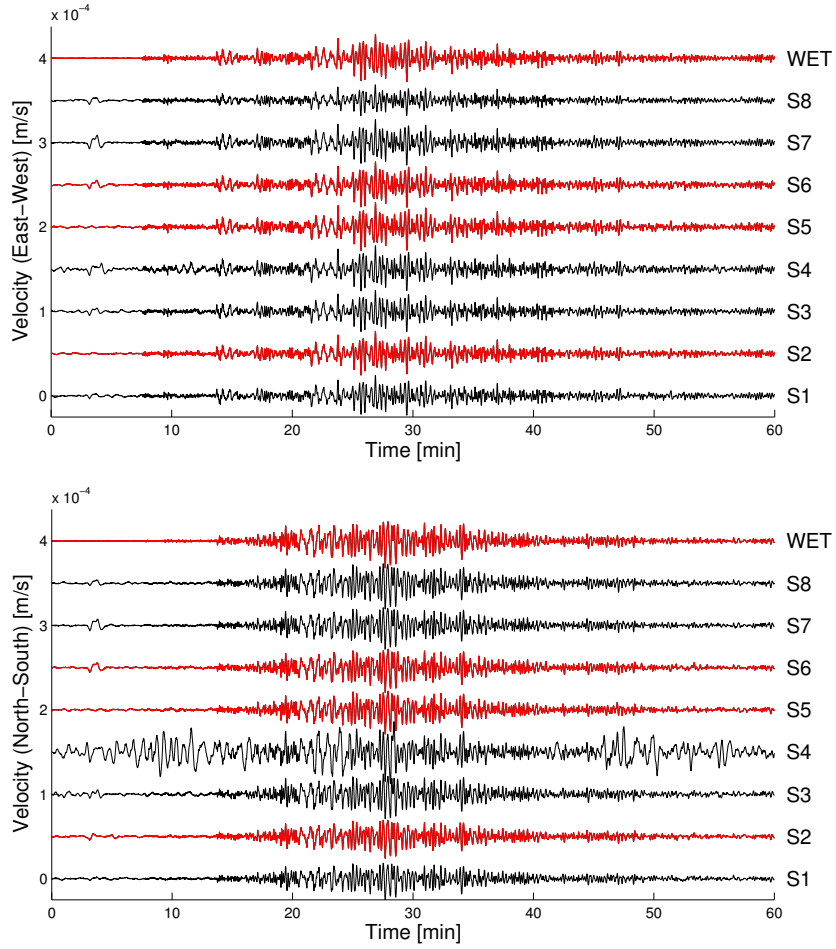


Figure 3.15: Horizontal component of the velocity recorded by the array seismometer for the December 26, 2003, Bam, Iran earthquake. The data from station S2, S5, S6 and broadband are used to derive the rotations. a) The East-West components, b) The North-South components.

3.8 Array-derived rotation rate versus transverse acceleration

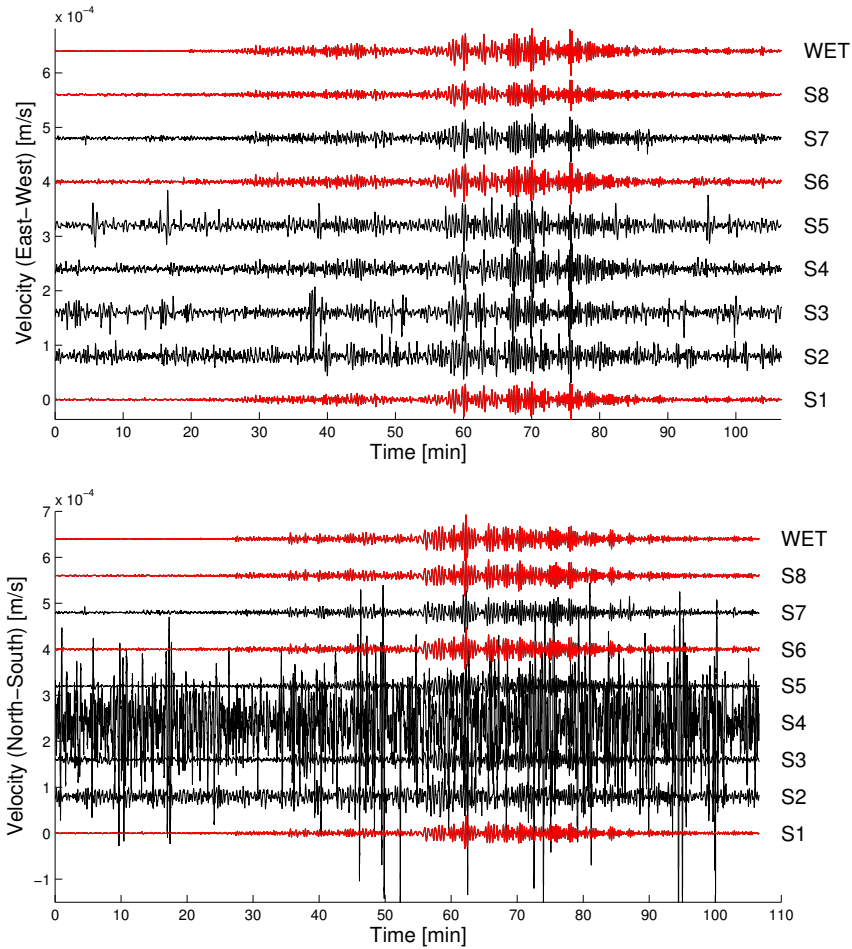


Figure 3.16: Horizontal component of the velocity recorded by the array seismometer for the 7 February 2004 Papua, Irian Jaya Indonesia earthquake. The data from station S2, S5, S6 and broadband are used to derive the rotations. a) The East-West components, b) The North-South components.

3.8 Array-derived rotation rate versus transverse acceleration

the data recorded by the broadband station, then we have four stations to derive the rotation rate. Since the direct measurement of vertical rotation rate was not available during this event (due to very low signal-to-noise ratio), we will compare the array-derived rotation rate with the transverse acceleration from broadband station.

In section 2.3.3 we have shown that assuming a plane wave propagation, transverse acceleration and the vertical component of rotational rate should be in phase and their ratio identical to twice to the horizontal phase velocity. The transverse acceleration is scaled (i.e., converted to rotation rate) by dividing by twice a constant phase velocity (5000 m/s as approximation for the local Love wave phase velocity). Figure 3.17 and Figure 3.18 show the computed time histories of the scaled transverse acceleration (red lines) superimposed with the vertical component of ground rotation rate (black lines) across the array for the Bam, Iran and Papua, Indonesia earthquake respectively. Their array-derived rotation rate match quite well with the transverse acceleration with cross correlation coefficient above >0.90 and >0.82 respectively. Figure 3.17 and 3.18 shows that the com-

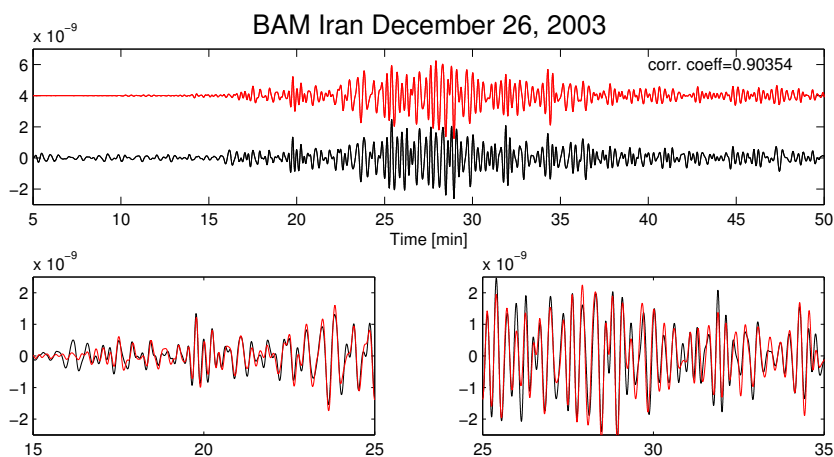


Figure 3.17: Comparison of collocated transverse acceleration (red lines) observed by GRSN broadband seismometer with array derived rotation rate (black lines) for the Bam, Iran earthquake.

parison between the array-derived rotation rate and transverse acceleration have

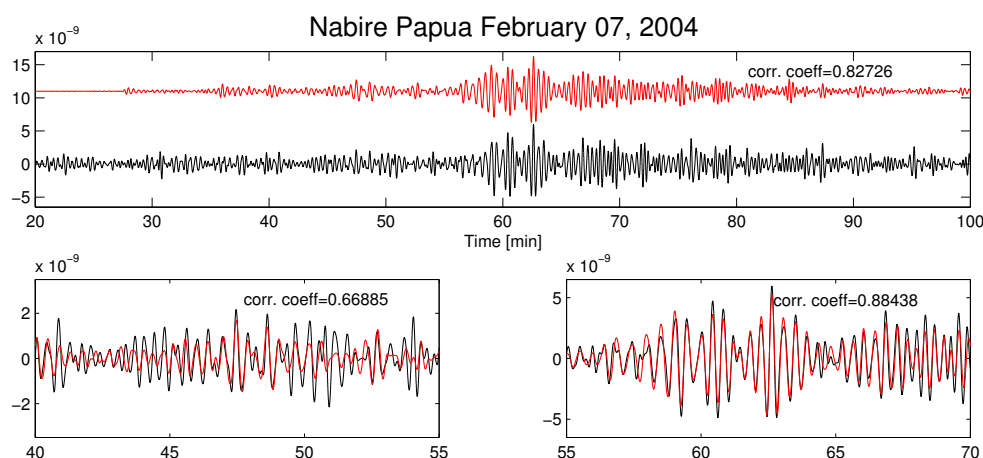


Figure 3.18: Comparison of collocated transverse acceleration (red lines) observed by GRSN broadband seismometer with array derived rotation rate (black lines) for the Papua, Indonesia earthquake.

a good agreement especially for time windows containing the surface wave trains. This suggest and further supports the conclusion that the array seismograms, the broadband sensor and the ring laser consistently provide the same information on the rotational part of the wave field.

3.9. Discussion and conclusions

As suggested by the theory, the vertical component of rotation rate can be derived from the horizontal components of seismic records. The accuracy of array-derived rotation rate is strongly dependent on the quality of the recorded translational seismograms. The application of the "seismo-geodetic" method (Spudich *et al.* (1995), Bodin *et al.* (1997)) to the derivation of the rotational component of the ground motion is flexible in that it can be used for arbitrary stations' configuration and number of stations (that is, more than three stations). The comparison between array derived rotation rate and ring laser data shows that the method is sufficient to model the rotational ground motion. It is shown in Figure 3.9b that using nine stations the phase error is reduced as the correlation coefficient is

greatly increased, compared to the two plots on the right hand side of Figure 3.9a.

Using ring-laser technology we present here the first comparison of seismic array-derived rotations with direct measurements. The goal of this study was (1) to quantify the accuracy with which rotations can be derived from seismic array data; (2) to investigate the effects of noise; and (3) to discuss issues concerning array versus direct measurements of rotations. The seismic array experiment that was carried out between December 2003 and March 2004 with a radius of ≈ 1.5 km around the ring laser instrument was to some extent sub-optimal because (1) the seismic equipment we used (LE3D-5s) is not designed for teleseismic studies and long-period signals, and (2) as far as the array geometry goes, the emphasis was on having a shape as close to a regular “finite-difference stencil” as possible resulting in heterogeneous site conditions (from muddy forest ground to outcropping granite boulders). These conditions and the high noise levels on the horizontal components resulted in a data set in which only very few large teleseismic events were usable for the rotation estimates.

Nevertheless, in the light of the experimental circumstances the fit between array-derived rotations and direct ring laser measurements (Figure 3.14) is stunning, given the observation of a wave field property (rotation around a vertical axis) with entirely different physical methodologies. We expected that errors in individual station observations play a stronger role particular when calculating spatial derivatives. The estimated noise level in the array seismograms was around 3% and it is interesting to note that a quantitatively similar misfit between array-derived rotation and direct measurements is observed for the most dominant signals (Love waves). These results indicate that – given accurate measurements of translational motions in an array of appropriate size and number of stations – the array-derived rotation rate may be very close to the “true” rotational signal that would be measured at the center of the array (or the specific reference station). However, it is important to note that – given the observations described in Figure 3.8 – it may be dangerous to use only the minimally required three stations as even relatively small noise levels may deteriorate the rotation estimates.

The influence of a random signal in the translational data gives more pronounced effects to the array derived rotation rate. Figure 3.10 shows that if the

noise level in the horizontal components of the seismograms is equal or superior to five percent, then the array-derived rotation rate is very inaccurate. One attempt to minimize this noise is to optimize the installation of the seismometers (adequate coupling and proper choice of site). As we can see from the random noise experiment (Figure 3.10), the effect of real noise of about 3% of the maximum amplitude of the velocity provided a RMS difference of about 3.6%. This is consistent with the data presented in Figure 3.10 since that RMS lies between the RMS difference of the one percent and five percent cases of synthetic noise. This suggests that the accuracy of the array-derived rotation rate from real data is adequate and should be comparable with the ring laser data.

Unfortunately this was the only earthquake event recorded by the ring laser instrument during the array experiment (Table 3.1). Nevertheless, when the ring laser data or other rotational sensor data are not available, it is still possible to compare the array-derived rotation rate with the collocated transverse acceleration (Figure 3.17 and 3.18) from broadband sensor assumes that the local horizontal phase velocity is known.

While the results suggest that the observation of array-derived rotations is feasible, it is important to note that we considered a fairly long-period signal in this study. Errors will certainly be more pronounced for earthquakes with shorter epicentral distances and higher-frequency wave fields. In the light of this, the necessity to develop field-deployable rotational sensors with the appropriate resolution for use in local and regional seismology remains an outstanding issue.

4. Love-wave dispersion from collocated measurements of rotation and translations

"This twisting displacement, at first appears to indicate a vorticose movement beneath each point thus affected; but this is highly improbable."

Darwin, 1845

In this chapter I present a specific application of rotational data to derive the local horizontal phase velocity and to determine the Love-wave dispersion curve. The Love-wave dispersion curve are then compared with the theoretical Love-wave dispersion curve calculated using the AK135 Earth model (Kennett *et al.*, 1995) based on the eigenvalue problem described by Friederich (1999).

4.1. Introduction

One of the key questions concerning rotational motion is, what information we can infer from rotational ground motions excited by earthquakes? Since rotation component around the vertical axis is sensitive to SH waves and not to $P - SV$ waves we will have more accurate data for arrival times of SH waves Takeo & Ito (1997). Furthermore, they have shown (based on a theoretical study) that the strain tensor and the spatial variation of slip velocity in the area of earthquake will be large at the edge of a fault plane due to spatially rapid changes of slip

on the fault and/or a formation of tensile fractures. It is also expected that the measure of rotations will allow to better constrain earthquake rupture histories (e.g. Takeo (1998)).

A representation of rotational data recorded by ring laser gyroscope have been reported by several investigators (e.g., McLeod *et al.*, 1998; Pancha *et al.*, 2000; Stedman *et al.*, 1995). Some important results that should be noticed here are the sensitivity of the ring laser being adequate to sensing rotational signals from earthquakes and the consistency of the ground rotation signal recorded by ring laser compared with transverse acceleration both in phase and amplitude. This consistency is based on the theoretical relation between transverse acceleration and rotation rate. They should - assuming plane wave propagation and transverse polarization - be in phase and their amplitude ratio proportional to horizontal phase velocity. In turn, this implies that estimates of horizontal phase velocities - particularly of Love-waves - should be possible with collocated point measurements of rotation and translations. Otherwise, this would only be possible with seismic array or additional strain measurements. Such point-measurements with additional rotational sensors may prove to be useful for very sparse or single-station networks (e.g. in planetary seismology).

The determination of frequency-dependent surface-wave phase velocities has for a long time been one of the most important tools to determine 3-D seismic velocity structure on regional and global scales (e.g., Nataf *et al.*, 1984; Snieder, 1988a,b). On small scales, near-surface low-velocity structures crucial for the estimation of hazard-relevant site effects can be determined using ambient noise measurements (e.g., Kind *et al.*, 2005; Milana *et al.*, 1996). Recently, it was shown that Rayleigh-wave dispersion curves can be derived by correlating long time series of ambient noise (micro-seismicity) and that the velocity structure thus derived can be used to image 3-D structures (e.g., Campillo & Paul, 2003; Shapiro & Campillo, 2004; Shapiro *et al.*, 2005). The aforementioned techniques require observations from seismic arrays to recover frequency-dependent propagation times (and thus phase velocities) across the array in the direction of propagation. Standard seismic observations are restricted to three components of translations, despite the fact that the recovery of the complete motion requires the observation of three additional components of rotations and six components of strain (e.g., Aki & Richards, 2002;

Trifunac & Todorvska, 2001). In the past years, rotation sensor technology has been improving in a way that may allow the development of routine sensors for three additional rotational motion components useful for seismological purposes (e.g., Schreiber *et al.*, 2005, 2006). Recent observations of local, regional and global wavefields using ring laser technology showed that the rotational measurements are fully consistent with collocated observations of translations (e.g., Cochard *et al.*, 2006; Igel *et al.*, 2005, 2007) following earlier observations of earthquake-induced rotational motions (e.g., McLeod *et al.*, 1998; Pancha *et al.*, 2000). Further confirmation of accurate measurements of the new observational component using ring laser technology came through comparison with rotational motions derived from seismic array data (Suryanto *et al.*, 2006) using a classical approach (e.g., Spudich *et al.*, 1995). A temporary array was installed around the ring laser instrument and direct and array-derived rotations compared for an event with high signal-to-noise ratio. The high correlation-coefficient (0.93) and almost identical amplitudes for the two independent rotation measurements observed with entirely different physical principles further indicate that the ring laser indeed measures the rotational motions accurately in a wide frequency range. A simple relationship between transverse acceleration and rotation rate (around a vertical axis) shows that both signals should be in phase and their ratio proportional to horizontal phase velocity. Igel *et al.* (2005) and Cochard *et al.* (2006) exploited this relationship to estimate horizontal phase velocities in sliding time windows along the observed time series. Comparison with synthetic traces (rotations and translations) and phase velocities determined in the same way showed good agreement with the observations. These initial results suggested that the determination of Love-wave dispersion curves (and thus information on local 1-D shear velocity structure) may be possible. It is worth noting that a similar relationship between strain and displacements can be used to determine horizontal phase velocities (e.g., Gomberg & Agnew, 1996; Mikumo & Aki, 1964). In this study we present a novel method for the determination of Love-wave phase velocities based on collocated measurements of translations (standard broadband seismometer) and rotations around a vertical axis (observed by a ring laser). Instead of determining phase velocities in the time domain (e.g., Cochard *et al.*, 2006; Igel *et al.*, 2005, 2007), we average spectral ratios of several earthquakes

4.2 Surface-wave Phase velocity determination

which allows us to directly determine frequency dependent Love-wave phase velocities and compare them with theoretical predictions for spherically symmetric Earth models. The results are supported by applying the same processing steps to complete 3-D synthetic seismograms for some of the observed events.

4.2. Surface-wave Phase velocity determination

The two types of surface waves that propagate along the surface of the Earth are Rayleigh waves and Love-waves. Rayleigh waves are resulting from an interaction of P (compressional waves) and vertically polarized S (shear waves) waves (SV) with the free surface, generating an elliptical retrograde (or prograde) ground displacement in a vertical plane. Love-waves are generated by interaction of horizontally polarized S waves with the free surface, producing a horizontally transverse motion. Love-waves propagate faster than Rayleigh waves as clearly shown in a seismogram.

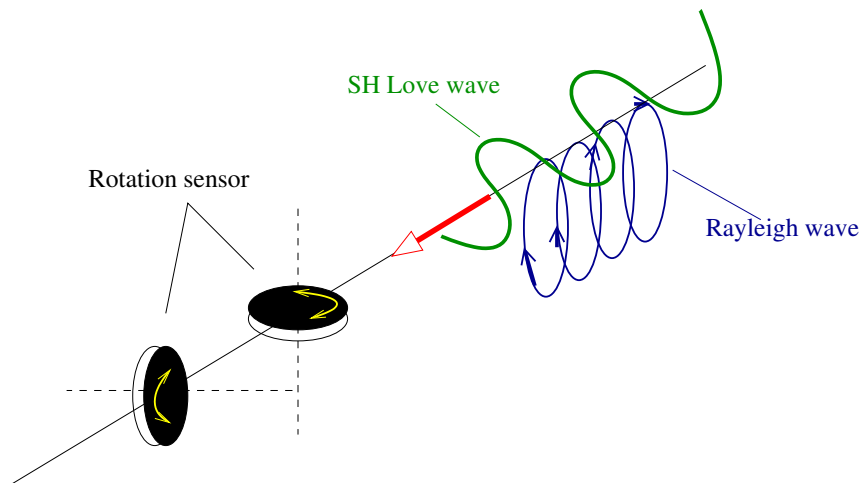


Figure 4.1: Rotational motion induced by Love and Rayleigh waves. Love-wave will trigger a vertical component of rotation, while a Rayleigh wave will induced a horizontal component of rotation on a rotation sensor.

Both Love and Rayleigh waves have a non-zero rotational component that will be recorded by rotation sensors of appropriate orientation (Figure 4.1). Surface

4.2 Surface-wave Phase velocity determination

waves are usually the dominant feature on the seismograms in the period range between 10-200 s and much of the reliable information on the long period part of seismic source spectra is obtained from surface waves (Aki & Richards, 2002).

Surface waves can be used to investigate the geological structure inside the Earth. For this purpose, based on the source that generate the observed signals, there are two types of surface wave experiments that can be done, namely active and passive methods. The active method is usually conducted for geotechnical applications, such as bedrock determination, seismic hazard assessment, and geological mapping. It uses an artificial high frequency vibration source. Hence, the depth of penetration is only several tens of meters. The passive method uses more a broad frequency band by recording ambient vibrations or microseismic data. Hence, it could be used for more regional scale application (Aki, 1965). The surface-wave data further provide important constraints on anisotropy in the uppermost mantle (Friederich & Huang, 1996).

The main attribute of the surface wave which is under investigation is their phase velocity. The phase velocity, c_p is defined by

$$c_p = \frac{\omega}{\kappa}, \quad (4.1)$$

where ω is the angular frequency and κ is the wavenumber.

Following Aki & Richards (2002), conventionally the phase velocity can be derived by assuming that the wave group consists purely of a single surface-wave mode, possessing a propagation velocity determined only by frequency. Suppose that the wave group propagates along the x -axis and is expressed as

$$f(x, t) = \frac{1}{2\pi} \int_{-\infty}^{\infty} |f(x, \omega)| \exp \left[-i\omega \left(t - \frac{x}{c_p(\omega)} \right) + i\phi(\omega) \right] d\omega \quad (4.2)$$

where $|f(x, \omega)|$ is the amplitude spectral density, $\phi(\omega)$ is the phase term due to factors others than propagation, and $c_p(\omega)$ is the phase velocity. The phase delay $\omega x/c(\omega)$ due to propagation can be obtained by Fourier analysis of the seimogram. The Fourier transform of the above equation can be written as

$$\int_{-\infty}^{\infty} f(x, t) \exp(i\omega t) dt = |f(x, \omega)| \exp \left[i\phi(\omega) + i \frac{\omega x}{c_p(\omega)} \right] d\omega \quad (4.3)$$

4.2 Surface-wave Phase velocity determination

The phase-velocity $c_p(\omega)$ can be obtained by taking the difference in phase spectra between two stations at distance x_1 and x_2 , which is $[\omega/c(\omega)](x_1 - x_2) \pm 2n\pi$. The unknown integer value n can be determined by an approximate a priori knowledge of $c(\omega)$, by measurement at more than two stations. The main property of surface waves is their dispersive behavior i.e. the velocity along the surface depends on the frequency.

The dispersion provides the information about the nature of the velocity as a function of depth. Stronger velocity gradient will produce more pronounced dispersion (Figure 4.2).

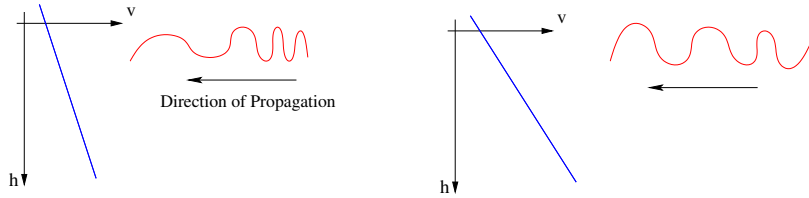


Figure 4.2: The dependence of the dispersion of surface waves on the velocity gradient in the vertical direction. A stronger vertical velocity gradient causes greater dispersion (Modified from Lay & Wallace (1995)).

Dispersion studies are carried out by analyzing the seismic data from a set of observation (seismic array).

4.2.1. Rotation rate and transverse acceleration

From Equation 2.2 it is clear that we can determine rotation from array measurements of displacement by taking derivatives. Based on this relation, further information can be obtained from collocated recordings of transverse and rotational components of the ground motion. Assuming a plane wave passing through the array along the x direction (1 Dimensional case), the y -component of the velocity can be written as

$$v = v_y \sin(kx - \omega t). \quad (4.4)$$

The transversal component of the acceleration is

$$a = -v_y \omega \cos(kx - \omega t). \quad (4.5)$$

4.3 Phase velocity determination in the time domain

With the use of equation (3.1), the z-component of rotation rate is defined as

$$\Omega_z = -\frac{1}{2}v_y k \cos(kx - \omega t). \quad (4.6)$$

Dividing Eq. 4.6 by Eq. 4.5 we will have

$$\frac{\Omega_z}{a} = \frac{1}{2} \frac{k}{\omega} = \frac{1}{2c_p}. \quad (4.7)$$

From Equation 4.7 it clear that the rotation rate should be in phase with the transverse acceleration and the amplitude differs with a factor of $\frac{1}{2} \frac{k}{\omega}$ or half of the phase-velocity, c_p below the measurement point.

Thus, providing a horizontal recording (E-W) and (N-S) of a seismometer plus a vertical component of rotation rate, a phase velocity below the measurement point can be estimated. This technique have been introduced by Igel *et al.* (2005) to estimate the phase velocity from a teleseismic event (Tokachi Oki, Japan) recorded by collocated broadband sensor and ring laser in Wetzell Germany. The quantity to measure the quality of the waveform matching of the transverse acceleration and rotation rate is the normalized cross-correlation coefficient (Igel *et al.*, 2005).

In order to have the transverse component of the ground motion, the horizontal component must be rotated along the great circle path toward the Earthquake source epicenter that should be known previously. We can turn the argument around and the back azimuth can be estimated searching the correct angle which give the maximum value of correlation coefficient between the transverse acceleration and rotation rate in a sliding time window.

4.3. Phase velocity determination in the time domain

The complete procedure to determine the phase velocity and back azimuth (BAZ) as a function of time from collocated measurements of rotation and translation is shown in the following procedure.

To estimate the horizontal phase velocity, I used the following step

- Read $E - W$, $N - S$ and R

4.3 Phase velocity determination in the time domain

- Resample $E - W$, $N - S$ and R
- Band pass filter $E - W$, $N - S$ and R
- FOR $i=1:\text{slidinglength}:\text{N-windowlength}$
 - FOR $\text{BAZ}=0:360$
 - Calculate Transverse (T) component from $E - W$ and $N - S$
 - Calculate the correlation coefficient of T and R
 - IF $\text{xcorr} \geq 0.9$
 - * save xcorr
 - * save $c_p = \frac{T}{2R}$
 - * save BAZ
 - END IF
 - END FOR BAZ
- END FOR i

Here the $E - W$, $N - S$ and R are the east-west, north-south and rotational component of the ground respectively.

We first illustrate the possibility of deriving phase velocities using the time-domain approach pursued by Igel *et al.* (2005, 2007). Figure 4.3, 4.4 and 4.5 show the estimated back azimuth and horizontal phase velocity for Hoceima, Papua and Hokkaido synthetic event. The synthetic data are low pass filtered up to 0.05 Hz according to their numerical simulation accuracy. Horizontal phase velocities are estimated by sliding a 10 s time window along the time series of rotation rate and transverse acceleration containing the Love-wave signal. As expected, the estimated back azimuth has a maxima (black shaded) along the time window containing the Love-wave arrivals. The maximum correlation coefficient of the back azimuth are in a good agreement with theoretical value, which is plotted in red line.

The estimated phase velocities are in general also in a good agreement with expected phase velocity for Love-wave. For a spherically symmetric earth model love phase velocities would be in the range of 3800 m/s (at period of 10 s) to 4500 m/s (at period of 50 s).

4.3 Phase velocity determination in the time domain

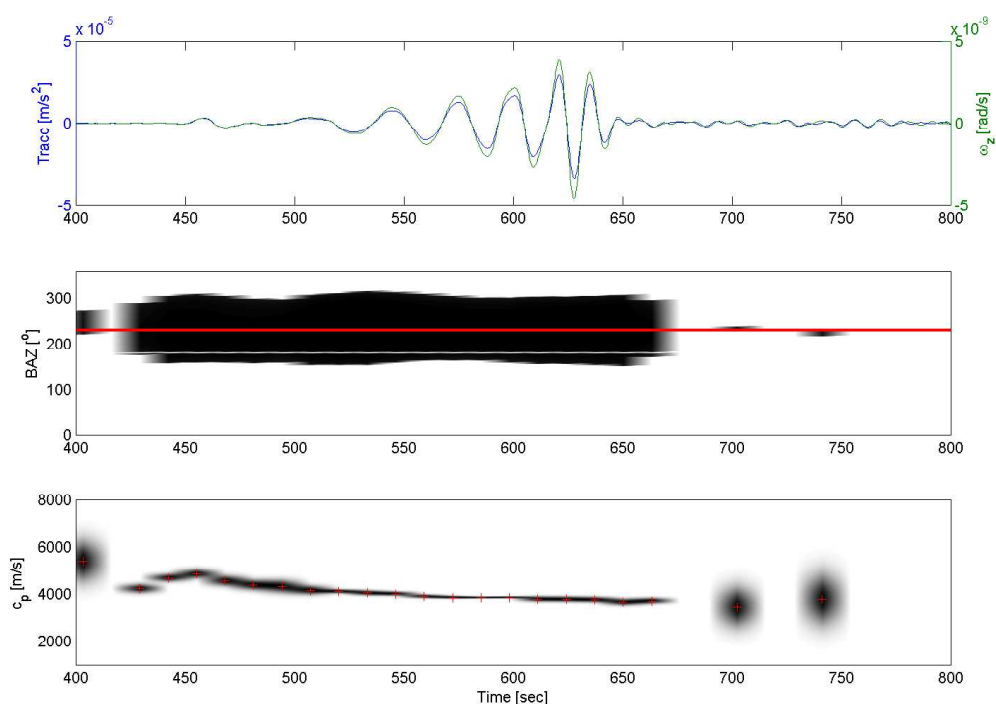


Figure 4.3: Point measurement analysis for synthetic data for Al Hoceima events (Figure 3.6). The transverse acceleration and rotation rate about a vertical axis in the reference station is plotted in the first upper figure, following by the estimated back azimuth and the phase velocity estimates. The actual back azimuth is represented by red line.

4.3 Phase velocity determination in the time domain

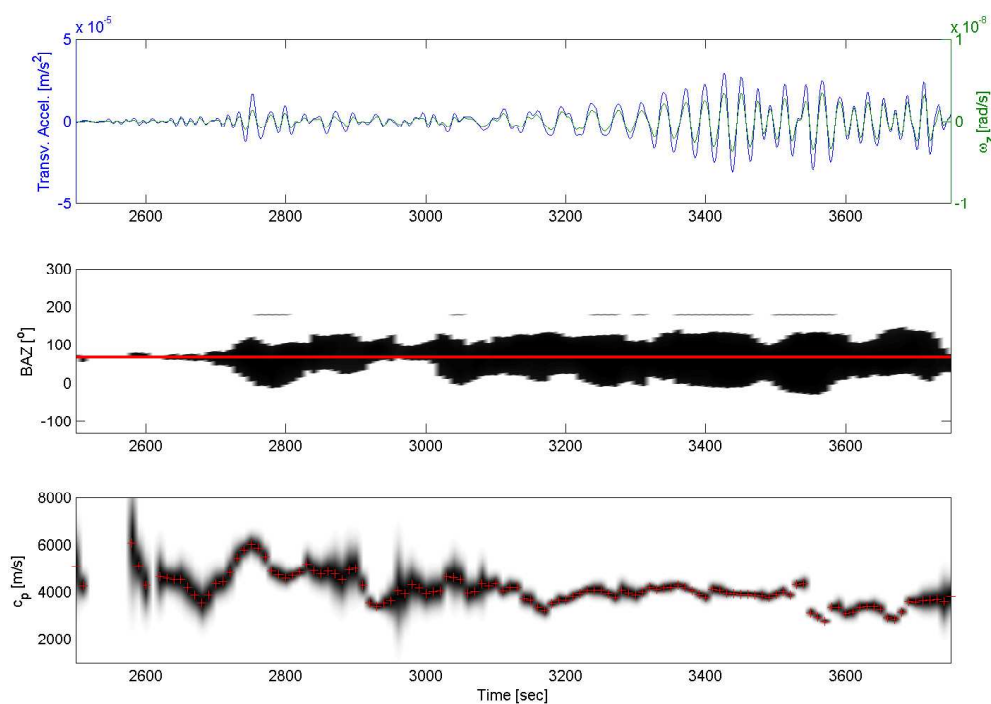


Figure 4.4: Phase velocity estimation of synthetic data for Papua, Irian Jaya events. The transverse acceleration and rotation rate about a vertical axis in the reference station is plotted in the first upper figure, following by the estimated back azimuth and the phase velocity estimates. The actual back azimuth is represented by red line.

4.3 Phase velocity determination in the time domain

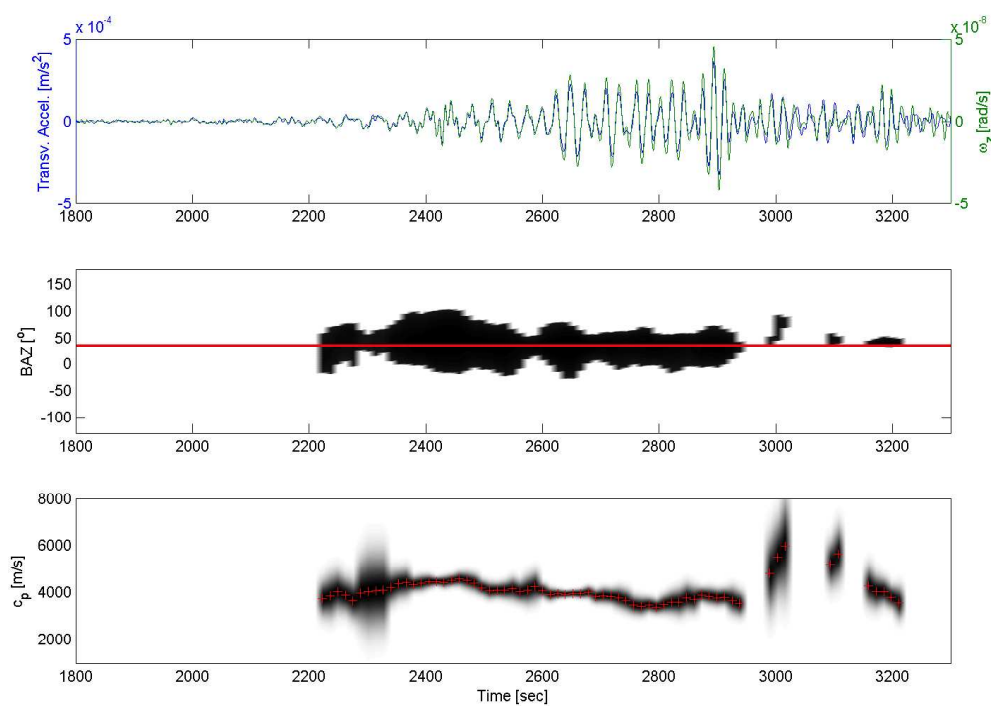


Figure 4.5: Phase velocity estimation of synthetic data for Hokkaido events. The transverse acceleration and rotation rate about a vertical axis in the reference station is plotted in the first upper figure, following by the estimated back azimuth and the phase velocity estimates. The actual back azimuth is represented by red line.

4.3.1. Observations and data analysis

We use translation data from station Wettzell (WET) of the German Regional Seismic Network (GRSN) located in Southern Germany ($12^{\circ}52'44''$ E, $49^{\circ}08'39''$ N). The station is equipped with an STS-2 broadband instrument with a flat response to ground velocity from 8.33 mHz (120 s) to 50 Hz. The data with a sampling rate of 80 Hz are corrected for instrument response, rotated into a local radial-transverse system, and differentiated to obtain transverse acceleration. The rotational data are measured by a ring laser instrument, called G, consisting of a He-Ne gas laser with an ultrahigh vacuum quality cavity enclosing an area of 16 m². The vertical component of rotation rate is recorded by this instrument with a sampling rate of 4 Hz. The instrumental sensitivity of ring lasers is limited by the scale factor and quantum noise processes. For the G ring laser rotation rates as small as 10⁻¹⁰ rad/s/Hz can be observed (Schreiber *et al.*, 2003). Further information on the ring laser instrument is given in Schreiber *et al.* (2005). The ring laser is mounted horizontally in the Geodetic Fundamentalstation Wettzell (about 250 m from the STS-2 seismometer). Given the frequency range (i.e., spatial wavelengths) considered below, we treat the two observations (rotations and translations) as collocated. From a growing event database with translations and rotations (see Igel *et al.* (2007)) we use several regional and global earthquakes in 2003 and 2004 with $M > 5.7$, listed in Table 4.1.

In Figure 4.6 and 4.7, time series of transverse acceleration (gray) and rotation rate (black) are shown for two events, the M6.3, Greece, 14 August, 2003, and the M6.7, Siberia, 1 October, 2003, respectively. The almost identical waveform fit between rotations and translations in both cases illustrate that the assumption of plane wave propagation is appropriate and that information on the horizontal phase velocity should be contained in the ratio between transverse acceleration and rotation rate. An appropriate measure of the fit between two presumably synchronous signals is the zero-lag normalized cross-correlation coefficient. We quantify the time-dependent similarity between rotation rate and transverse acceleration by sliding a time-window (10 s) along the time series and calculate the cross-correlation coefficient that is defined between 0 (no similarity) and 1 (perfect match). If the quality of the waveform fit in a given time window is

4.3 Phase velocity determination in the time domain

Table 4.1: Parameters of the observed earthquakes used for phase-velocity study.

Date	Time (UTC)	Lat. (deg.)	Lon. (deg.)	M_w	Location
21 May 2003	18:44:19	36.90°N	3.71°E	6.8	Northern Algeria
26 May 2003	09:24:32	38.90°N	141.45°E	7.0	Honshu, Japan
06 Jul. 2003	19:10:33	40.34°N	26.07°E	5.7	Turkey
14 Aug. 2003	05:14:55	39.19°N	20.74°E	6.3	Greece
25 Sep. 2003	19:50:06	41.77°N	143.90°E	8.3	Hokkaido, Japan
27 Sep. 2003	18:52:53	50.06°N	87.69°E	6.6	Southern Siberia
01 Oct. 2003	01:03:25	50.22°N	87.68°E	6.7	Southern Siberia
05 Feb. 2004	21:05:24	3.58°S	135.49°E	7.0	Irian Jaya, Indonesia
24 Feb. 2004	02:27:46	35.23°N	3.96°W	6.3	Gibraltar

above a threshold (0.95) we estimate a horizontal phase velocity for this time window by finding the best-fitting velocity in a least-squares sense, as well as the associated variance. These phase velocities and the associated uncertainties are shown for two particular earthquakes in the bottom plots of Figures 4.6 and 4.7 for time windows containing the fundamental Love-waves mode. In both cases, the estimated phase velocities are within the expected range of fundamental mode Love-wave phase velocities for spherically symmetric Earth models (3-5 km/s). However, the time-domain representation makes it difficult to extract the frequency dependent behavior of Love-waves. Therefore, we introduce an approach in which the phase velocities are directly estimated in the frequency domain.

4.3.2. Point measurements

The results above and those reported by Igel *et al.* (2007) and Cochard *et al.* (2006) indeed suggest that it should be possible to determine the phase velocities as a function of frequency (dispersion) by calculating the spectral ratios of transverse acceleration and rotation rate for time windows containing the Love-wave trains. For this purpose, the rotation rate is interpolated to the same sampling points as the transverse acceleration and the Love-wave train time window iso-

4.3 Phase velocity determination in the time domain

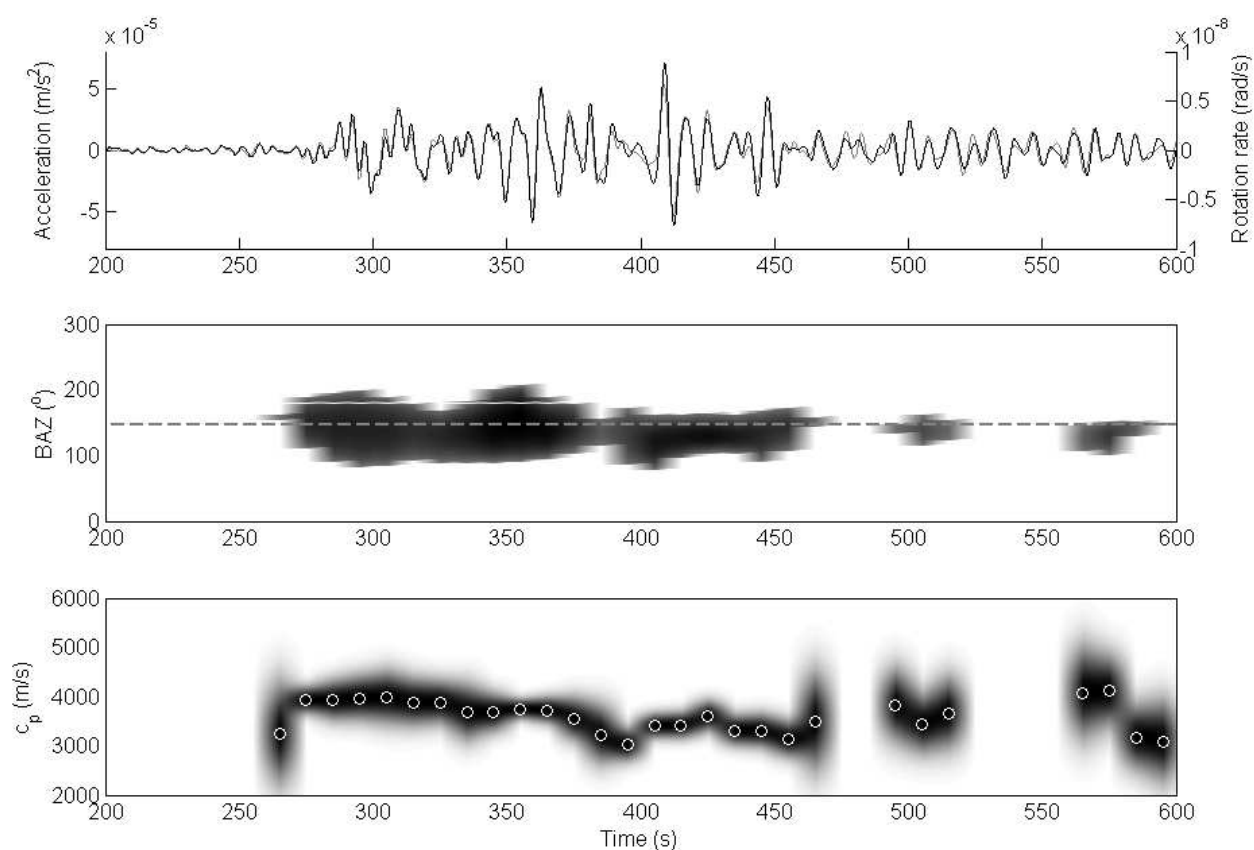


Figure 4.6: Upper trace: Transverse acceleration (gray, left axis) and rotation rate about the vertical axis (black, right axis) for the Greece event, M6.3, 14 August 2003. Bottom trace: Best-fitting horizontal phase velocities as a function of time in a 10 s sliding window.

4.3 Phase velocity determination in the time domain

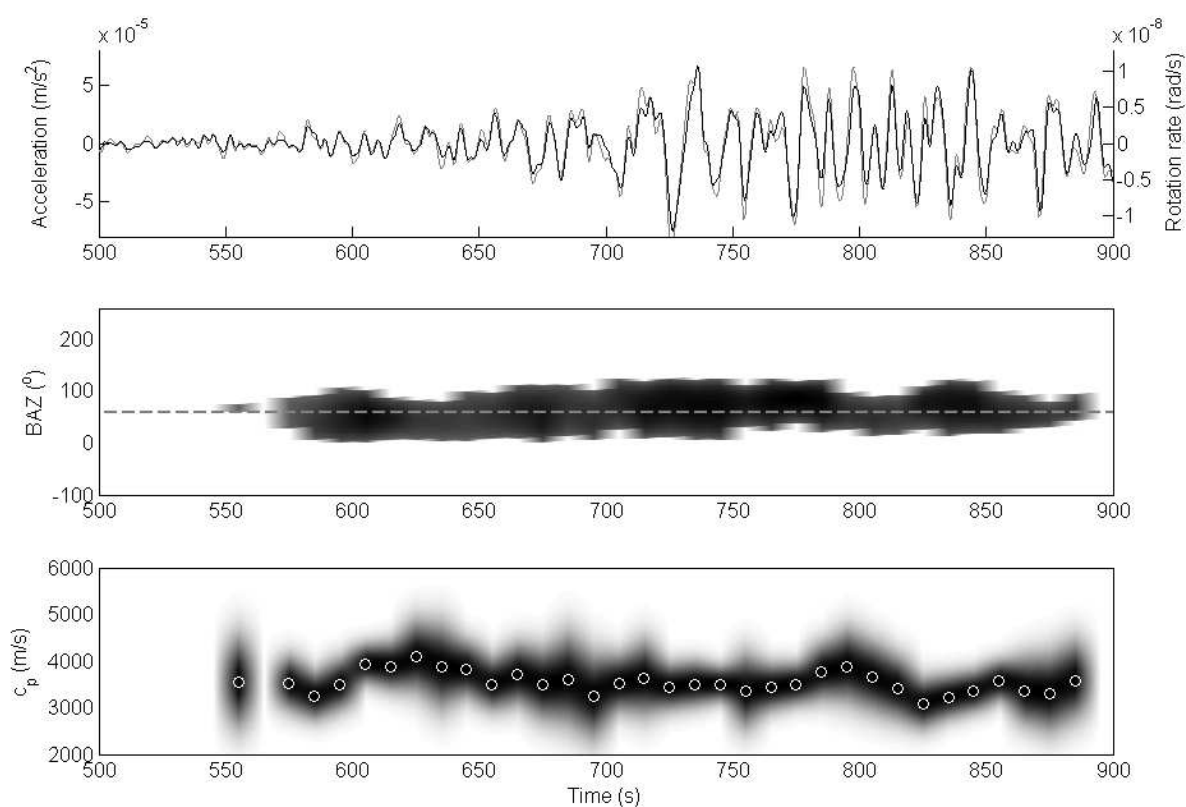


Figure 4.7: Upper trace: Transverse acceleration (gray, left axis) and rotation rate about the vertical axis (black, right axis) for the Siberia event, M6.7, 1 October 2003. Bottom trace: Best-fitting horizontal phase velocities as a function of time in a 10 s sliding window.

4.3 Phase velocity determination in the time domain

lated and attenuated at the edges with a Gaussian function. Both time series are transformed into the Fourier domain and the ratio of the spectra of rotations $\Omega(\omega)$ and transverse acceleration $a_T(\omega)$ leads to the frequency dependent phase velocities $c(\omega)$

$$\frac{a_T(\omega)}{\Omega(\omega)} = -c_p(\omega). \quad (4.8)$$

Because of the oscillatory nature of the individual spectra and spectral ratios we average the ratios from several events assuming that the resulting phase velocities are representative of the same subsurface volume. In addition, we smooth the ratios along the frequency axis using a Savitzky-Golay filter, a low pass filter also known as least square smoothing filter or DISPO (digital smoothing polynomial). The filter is defined as a weighted moving average with weights given as a polynomial of a certain degree; in this case we use degree two (Press *et al.* (2002)). We first test the methodology presented above on complete synthetic seismograms (rotations and translations) calculated for one regional (Gibraltar) and two global (Hokkaido and Papua) events using the spectralelement method (Komatitsch & Tromp (2002b), Komatitsch & Tromp (2002a)) employing a recent 3D tomographic model (Ritsema & Van Heijst (2000)) and the crust model by Bassin *et al.* (2000). The sources are modeled as point shear dislocations with source properties from the Harvard Catalogue [www.seismology.harvard.edu]. The resulting spectral ratios were averaged and processed as described above. The frequency-dependent phase velocities are shown in Figure 4.8 as Gaussians with mean value and variance for each period.

We superimpose theoretical predictions of Love-wave dispersion curves for the spherically symmetric AK135 Earth model (Kennett *et al.*, 1995) for the fundamental and the first three higher-order modes. Despite the small number of events the estimated Love-wave phase velocities seem to capture well those predicted for the fundamental modes in a spherically symmetric Earth model. The uncertainties decrease with increasing period. In the frequency (period) window considered, the largest deviation from the predicted values are 6.1% (at period 20s). We calculate stacked spectral ratios for the regional (Greece, Turkey, Gibraltar, Algeria) and global (all other) events listed in Table 4.1. The results are presented in Figure 4.9 in the same way as the synthetic data shown in Figure 4.8.

4.3 Phase velocity determination in the time domain

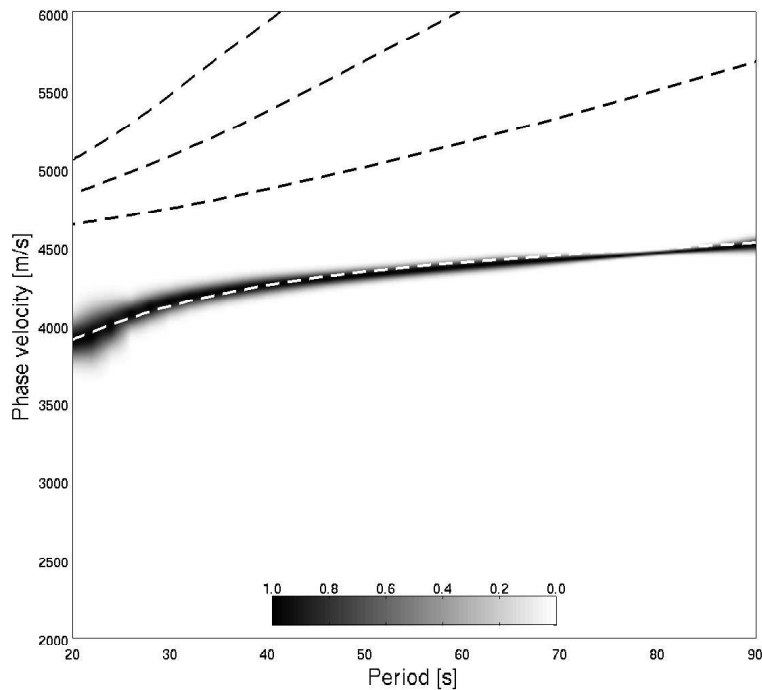


Figure 4.8: Frequency-dependent Love wave phase velocities from spectral ratios of synthetic seismograms calculated for the Gibraltar, Papua and Hokkaido events (see text for details) shown as mean values with variances as Gaussian uncertainties. The dashed lines indicate the theoretical fundamental- (lowest dashed line) and higher-mode Love-waves phase velocities (upper dashed lines) obtained for the ak135 Earth model.

4.3 Phase velocity determination in the time domain

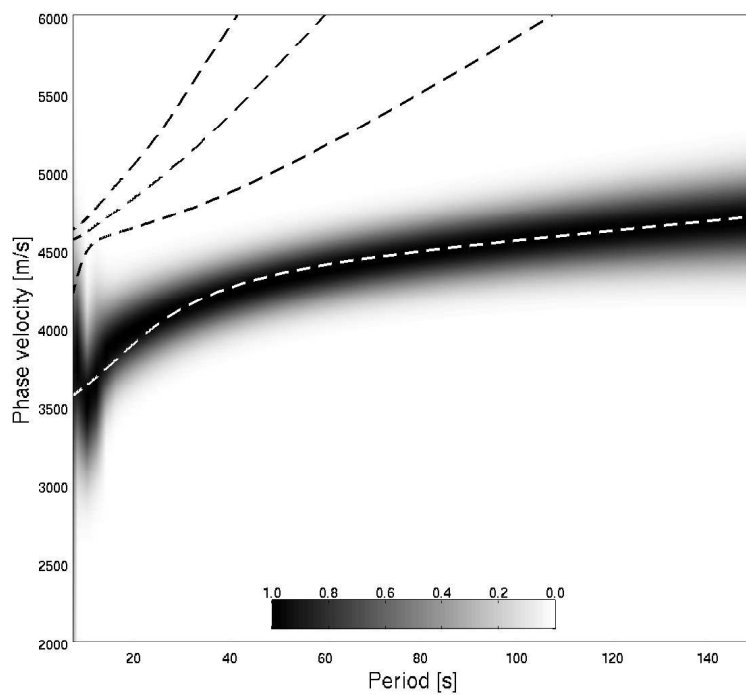


Figure 4.9: Love waves phase velocities derived from observed data shown as mean values (black) and associated uncertainties using grey shading (see text for details) for all event listed in Table 1. The dashed lines indicate fundamental- and higher-mode Love-waves phase velocities obtained for the ak135 Earth model.

Except in the period range around 10 s, the Love-wave phase velocities determined by the spectral ratios are close to the predicted values. The increase in phase velocities towards longer periods is well captured by the stacked global events, with almost constant uncertainty with period. The maximum deviations of the mean values are about 5.8 % (at period 100 s). The reasons for any discrepancies may be 3D heterogeneity, anisotropy, non-planar wavefronts, deviations from the great circle paths, or uncertainties in the observations of translations and rotations (e.g., site effects). To fully understand these potential sources of discrepancies will require a larger database, comparison with array-derived Love-wave dispersion curves and systematic synthetic studies.

4.4. Conclusion

In this chapter we present a novel methodology to derive Love-wave dispersion curves with point measurements of rotations (around a vertical axis) and translations. Frequency-dependent phase velocities are estimated by calculating the ratio between the spectra of transverse acceleration and rotation rate by stacking the ratios of several events. This approach was applied to 3-D synthetic data sets and several regional and global events observed by the collocated ring laser instrument measuring the rotation rate around a vertical axis and a standard broadband sensor located at Wettzell, SE-Germany.

Both synthetic and observed dispersion curves match well those predicted for the fundamental mode Love-waves. This indicates that plane-wave theory is appropriate and that the assumption of fundamental mode Love-wave propagation is approximately fulfilled, or that the energy of higher-mode Love-waves in the time-windows considered is low. The purpose of this study was primarily to illustrate the concept and show a first application to real observations. Love-wave dispersion curves can be used to derive local 1-D velocity structure and are therefore an important intermediate result for tomographic inversions. Whether the accuracy of the dispersion curves derived with the approach presented here is enough for tomographic purposes remains to be evaluated.

We intend to investigate these issues by systematic synthetic studies and analysis of a larger event database. Nevertheless, the results shown here indicate that

4.4 Conclusion

through additional measurements of accurate rotational signals, wavefield information is accessible that otherwise requires seismic array data. This may be of use when arrays are very sparse or consist of only one station (e.g., oceanography or planetary seismology). However, to make this methodology practically useful for seismology will require the development of an appropriate high-resolution six-component broadband sensor. Efforts are underway to coordinate such developments on an international scale (Evans *et al.*, 2006).

5. Horizontal components of rotation or tilt

".., but typically seismologist have been content with the rather arbitrary assumption that either acceleration or tilt dominates a particular signal."

Aki & Richards (2002)

In the previous section, we have shown the application of rotation rate about the vertical axis recorded by a rotation sensor (ring laser). In this section, I will focus on the rotation about the horizontal axis, i.e. the possibility to derive the rotation about the horizontal axis from an array of seismometers. In aeronautics, this term is known as Pitch and Roll (Figure 5.1). It should be noted that the rotation about a horizontal axis at the earth surface is known in geophysics as tilt. For the ring laser, it is standard to correct the ring laser's orientation change using tilt data. Therefore it is important to have an accurate tilt rate data in order to get the appropriate correction for the ring laser. For strong motion study it is also important to have an accurate tilt rate for correcting the seismometer's orientation. Ignoring tilt effects will introduce long period error, especially for calculation of permanent displacements.

5.1. Introduction

Observation of tilt on the earth surface was done since more than a century ago. In 1887 G. H. Darwin measured tilt that was caused by the earthquake that

happened in Ecuador. However, at that time, it was reported that the observation of tilt has no consistent pattern, and it was unclear how much they were caused by instrumental defects, how much by imperfect attachment to the ground, and how much by real tilting of the earth.

In the ensuing century, the development of tilt measurements was not as fast as the development of seismic wave measurement (Agnew, 1986). Tiltmeter and strainmeter are very appropriate for observing long-period seismic signals, seismic slip events on fault and for volcano monitoring. It may also be used to complement geodetic networks by providing continuous record (Gouly, 1976).

In recent years, varieties of optical and electronic tiltmeters became available, each with different resolutions and ranges. Based on the goal of the tiltmeter design, Agnew (1986) summarized the instrument property and the area of inquiry for which it is especially important (Table 5.1).

The effect of tilt is generally small but not negligible in seismology, especially in strong-motion earthquakes. It is well known that the tilt signal is most noticeable in the horizontal sensor. Ignoring the tilt effects leads to unreliable results, especially in the calculation of permanent displacements and long-period calculations (Graizer, 2005). It appears that full measurement of six components of the motion (three translations and three rotations) is necessary in the near-field study.

It is still an open question what technology is best suitable for measuring various components of rotation. For rotation along the vertical axis, as discussed previously in Chapter 2, results suggest that the optical devices are the way to go. Those optical devices could be advantageous compared to classical tiltmeters for the rotational motion about a horizontal axis as well (regardless of meteorological



Figure 5.1: Three components of torsional motions in aeronautics are known as Pitch, Roll and Yaw.

Table 5.1: Tiltmeter design properties and the area of interests (Agnew, 1986).

Property	Applicable Field
<i>Low Noise</i>	
High freq. ($T < 1$ hr.)	Seismic waves, coseismic offsets
Low freq. ($1 \text{ hr.} < T < 1$ week)	Earth tides, tectonic deformation
Very low freq. (> 1 week)	Tectonic motion
<i>Instrument response</i>	
Accurate and stable calibration	Earth tides
High dynamic range	Seismic waves
Immunity to high acceleration	Coseismic offsets
Linear response	Seismic waves, earth tides
No hysteresis	Coseismic offsets
Broadband response	Seismic waves
<i>Economic</i>	
Low operational cost	All
Ease of installation	All
Low capital cost	Volcano monitoring

characteristics - accuracy, sensitivity, etc - which remain to be assessed). Indeed, classical tiltmeters measure a change of angle with respect to the local vertical, determined by gravity; thus, they cannot discriminate between true rotation and pure change in the local gravity (e.g. due to mass redistribution).

It has been reported by several investigators that tilt signals can be used as earthquake precursors (Mortensen & Iwatsubo, 1986). They observed a tilt anomaly 40 hours before a pair of earthquakes ($M_L=4.2$ and $M_L=3.9$ 29 August 1978, in near San Jose, California) a gradual down-to-the-east tilting followed by rapid tilting down-to-the-north-northeast at a rate of $\frac{1}{2} \mu$ rad/hr. Although this phenomenon still needs further investigation it highlights the potential use of tilt measurements.

As discussed in the previous chapter, from collocated measurement of rotation rate about a vertical axis and transverse component of translations, we can extract the horizontal love wave phase velocity below the measurement point. This opens up a similar question: can we extract the Rayleigh wave phase velocity via collocated recordings of tilt and translational motions?

Another interesting subject we want to study in this thesis is the effectiveness of using tiltmeter for correcting the ring laser data. It is almost routine to correct the plane orientation of the ring laser basement with the help of tiltmeter data. However, as the tiltmeter is influenced by horizontal acceleration (not pure tilt effects), the tilt correction for the ring laser data may be faulty.

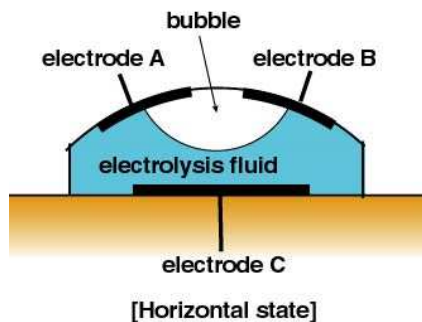


Figure 5.2: Bubble-tube tiltmeter in horizontal state.

5.2. The tiltmeter

In practice, tilt motions are usually observed at a single point with short baseline type instruments, in which the inclination of the plane is measured by a vertical or horizontal pendulum or bubble tiltmeter. The pendulum tiltmeters have been used extensively for measuring solid Earth tides

5.3 Tilt and horizontal accelerations

(Melchior, 1983). For vertical pendulums, the boom holding the mass is suspended vertically, and the relative variation of boom inclination with respect to a reference axis fixed to the ground that was mounted along the surface normal, is measured (Zadro & Braitenberg, 1999).

A bubble tiltmeter is a compact instrument that does not necessitate particularly sheltered housing. It consists of an electrolysis fluid and an air bubble held in glassware. Three electrodes A, B and C are set in the glassware as shown in Figure 5.2. When the ground is inclined as shown in Figure 5.3, the bubble in the glassware moves so that the electrode A becomes more covered by the electrolysis fluid, and the electrode B becomes more covered by the bubble. This results in the reduction and the increase of the electric conductivity between the electrodes B and C and between the electrodes A and C, respectively. We can detect the change in the ground tilt in this way. However, short base tiltmeters are inherently susceptible to local site effects, which are very difficult to quantify (Aki & Richards, 2002) and become unstable for long term use because of large drift related to the liquid content.

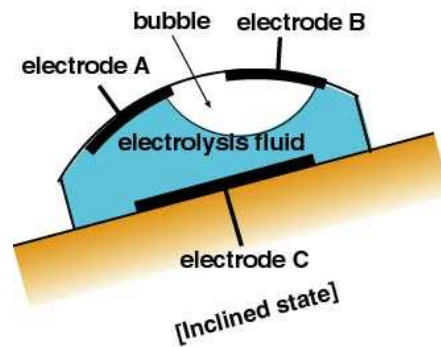


Figure 5.3: Bubble-tube tiltmeter in inclined state.

Another instrument that may be useful for tilt monitoring is a ring laser gyroscope. As mentioned in chapter 2 a ring laser is not susceptible to translational motions. Then, this instrument can be used for discriminating the tilt effects from ground acceleration (e.g., Farrell, 1969). The ring laser G0 installed on a wall of the underground cavern at Cashmere, Christchurch New Zealand measures the horizontal component of rotations (Dunn *et al.*, 2002). However these observations have not yet been analyzed in a systematic way.

5.3. Tilt and horizontal accelerations

Seismometers mostly use a pivot-pendulum or linear-pendulum type and therefore will be sensitive to tilt, especially for horizontal components. For small

5.3 Tilt and horizontal accelerations

angles, tilt and horizontal acceleration are directly proportional with a factor of g (gravitational forces). An attempt to separate the effects of tilt and horizontal acceleration was made by Farrell (1969) by using a gyroscope.

Below, I plot the observed three components of rotations for Al Hoceima event, both synthetic (left side) and observed (right side) in radians (Figure 5.4).

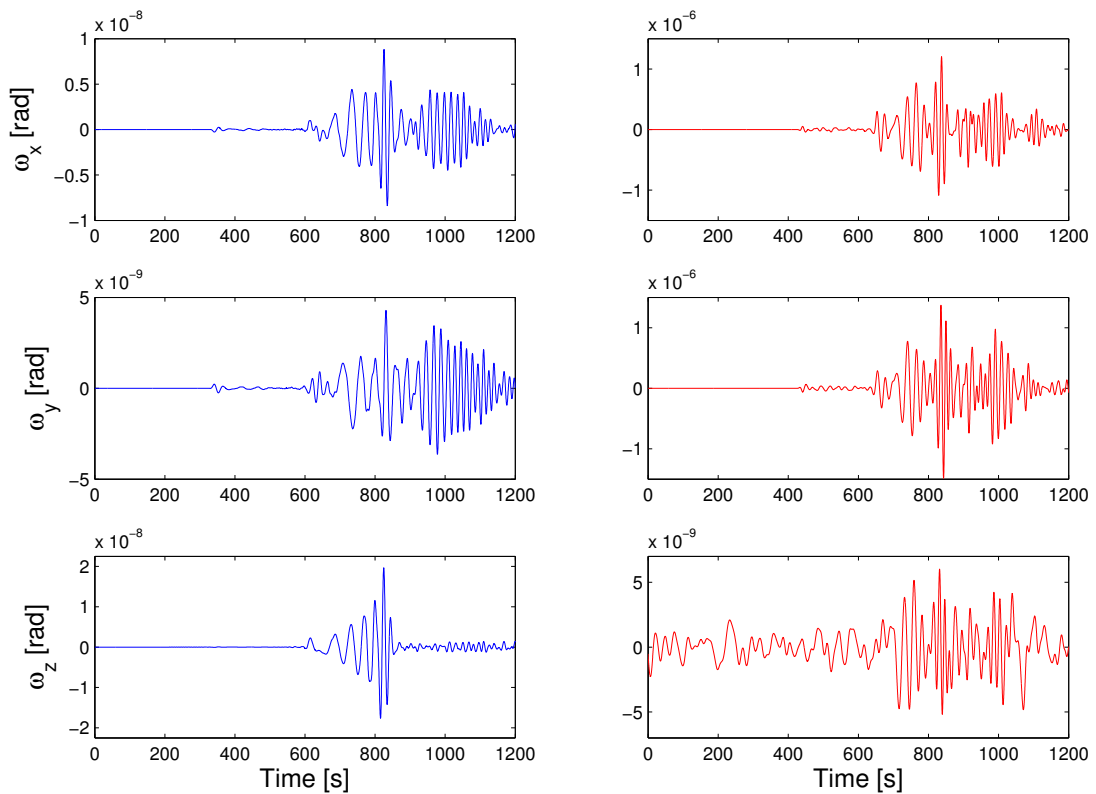


Figure 5.4: Three components of rotation from Al Hoceima earthquake event. Left side is for synthetic data and Right side is observed. See text for more details

The observed rotations along the horizontal axis are obtained by tiltmeter and the rotation about the vertical axis with a ring laser, respectively. The two-axis tiltmeter is a LGM Lippmann instrument with a very high angular resolution of 0.5 nrad. It measures the two components (N-S and E-W) with a sampling

5.3 Tilt and horizontal accelerations

rate of 5 Hz. From Figure 5.4 it can be seen that the observed tilt values are larger (by a factor of about 250 times) than the rotation about the vertical axis. Theoretically, as seen on the simulation result, the tilt is expected to be of the same order of magnitude than the rotation about the vertical axis.

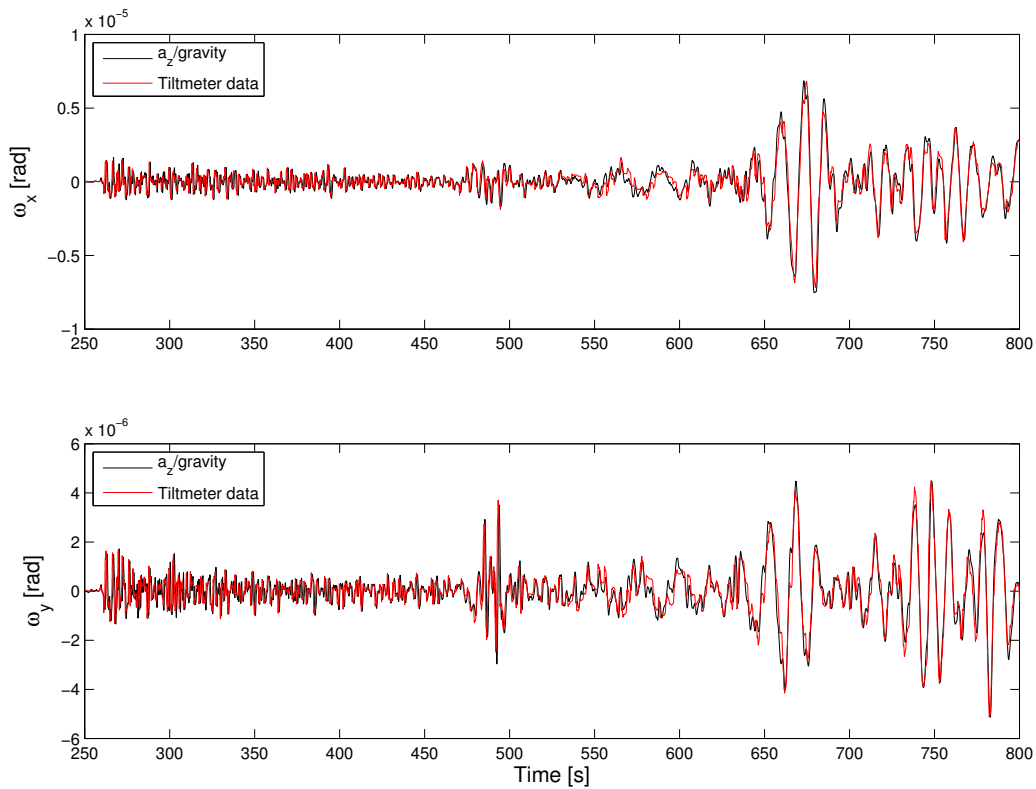


Figure 5.5: Superimposed plot between tilt and acceleration divided by a factor of g in x and y component.

It clearly shown from Figure 5.5 that tilt data measured by the tiltmeter in the surface wave frequency range is dominated by the horizontal acceleration divided by g . Note that Figure 5.5 is a superimposed plot from two different kind of instruments, i.e. the Lippmann tiltmeter (red line) and the STS-2 seismometer (black line), in the frequency range below 1 Hz.

Figure 5.6 and 5.7 clearly shows that at a period longer than 20 s, the tilt

5.3 Tilt and horizontal accelerations

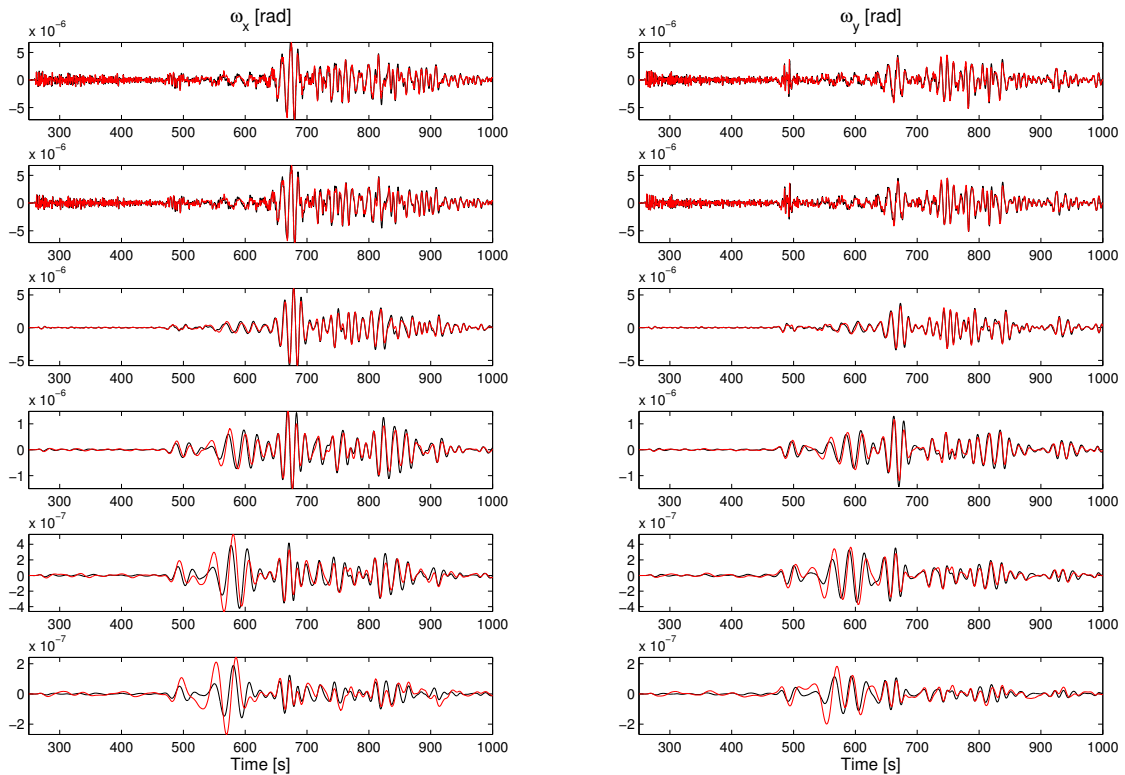


Figure 5.6: Superimposed plot between tilt and acceleration in x and y component low pass filtered at various cut off frequencies. The first upper figure is unfiltered, followed by cut off period of 1 s, 10 s, 20 s, 30 s, and 40 s.

5.3 Tilt and horizontal accelerations

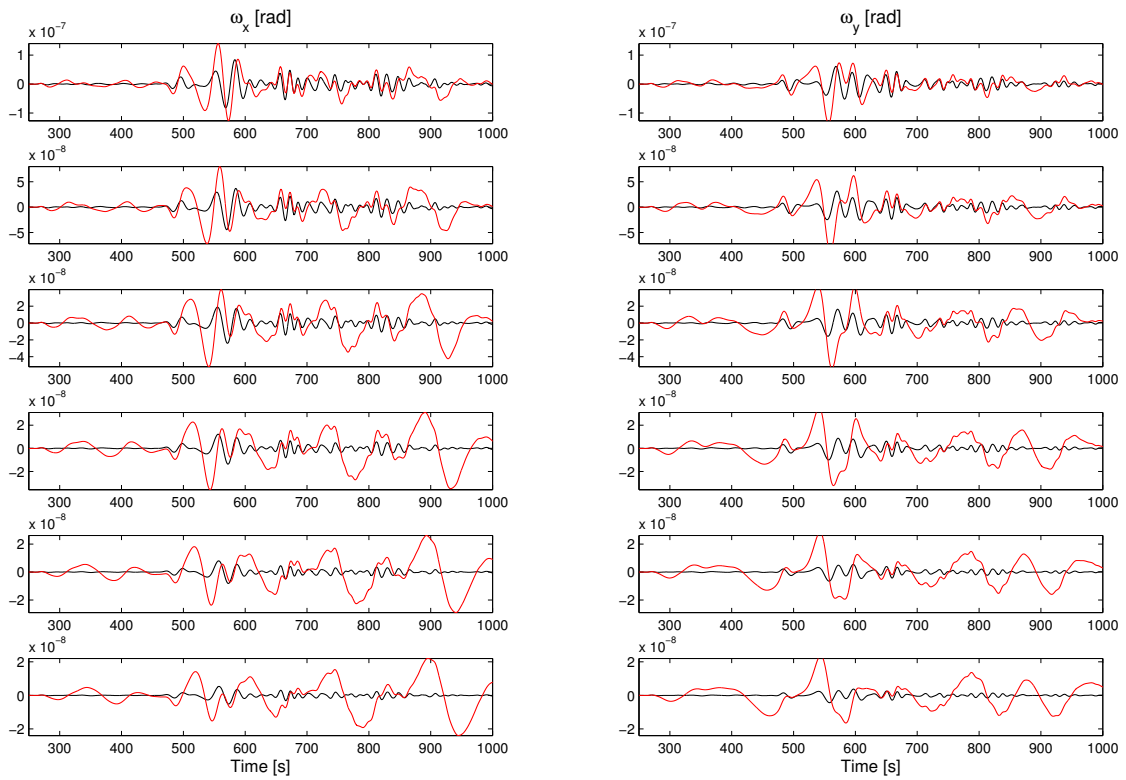


Figure 5.7: Similar than Figure 5.6 but with cut off frequencies of 50 s, 60 s, 70 s, 80 s, 90 s, and 100 s.

5.4 Array-derived horizontal components of rotations

signal from the tiltmeter is more pronounced (the amplitude is higher) than the horizontal acceleration (from seismometer) signal. For periods lower than 20 s, the tiltmeter will behave like an accelerometer. With this kind of tiltmeter, it is recommended to use in analyze long period signal such as earth tides or tectonic deformation studies. However, since seismologist need a more broad band tilt signal (especially in the higher frequency), a tilt sensor that can measure only the pure tilt signal is desirable.

Another question that will arise based on the results above is whether it is worth to use tiltmeters for correcting the ring laser data, since the real data needed for correction is tilting rate and not acceleration. Further discussion about this issue will be carried out in the last Section in this Chapter.

5.4. Array-derived horizontal components of rotations

In this section, I present a study about derivation of tilt from an array of translational data. The theoretical basis for deriving tilt from arrays has been presented before in Chapter 3. Both synthetic and real data will be analyzed.

5.4.1. Synthetic study of array derived tilt rate

For synthetic data, I use three events from Gibraltar, Hokkaido and Irian Jaya. Those event parameters were listed previously in Table 4.1. The station configuration is represented by Figure 5.8, which consists of eight stations and one reference station at the center of the array. Equation 3.2 was used to derive the horizontal components of rotations. The theoretical seismograms for translations and rotations were calculated by using the 3-D mantle model S20RTS (Ritsema & Van Heijst, 2000) combined with the global crust model CRUST2.0 (Bassin *et al.*, 2000), and a point-source approximation for the Gibraltar event and a finite-source (Ji, 2004) for Hokkaido and Irian Jaya event. Figure 5.9 shows the three components of rotation from theory superimposed with array-derived rotation from the Gibraltar event. Although they have a similar waveform, the

5.4 Array-derived horizontal components of rotations

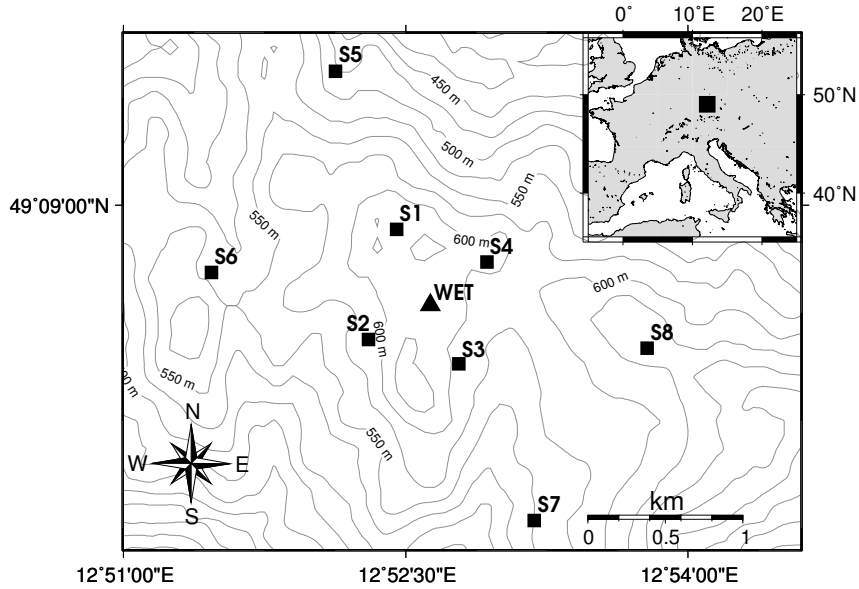


Figure 5.8: The array station setup. WET is the reference station located at the center of the array.

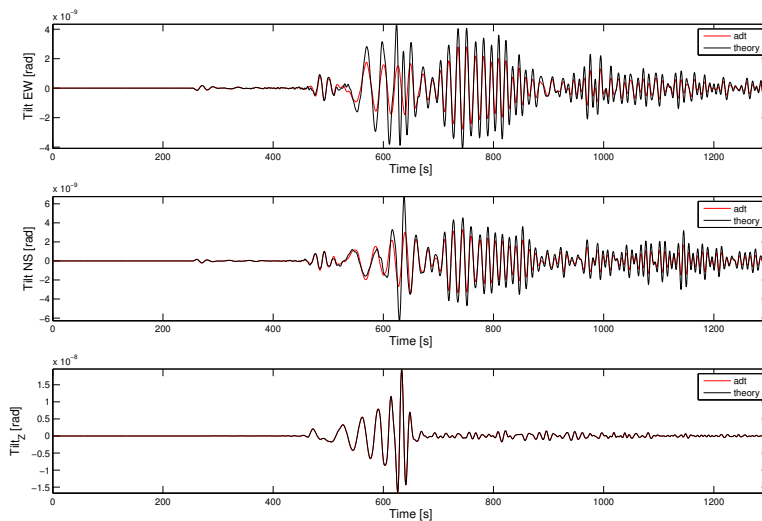


Figure 5.9: Three components of rotation from Gibraltar synthetic data. The red line is synthetic rotation calculated in the array center (WET) using nine stations including the reference station and the black line is array-derived rotation.

5.4 Array-derived horizontal components of rotations

array-derived rotation about the horizontal axis (in x component and y component) have a lower amplitude compared with theoretical data. The same characteristics are found also for Hokkaido (Figure 5.10) and for Irian Jaya event (Figure 5.11). Even though they have smaller discrepancies, one can still recognize that the amplitude from theoretical calculation does not match well the array-derived tilt. The source of this discrepancy is currently is currently not understood. Particularly given the fact that the vertical component of rotation matches perfectly well.

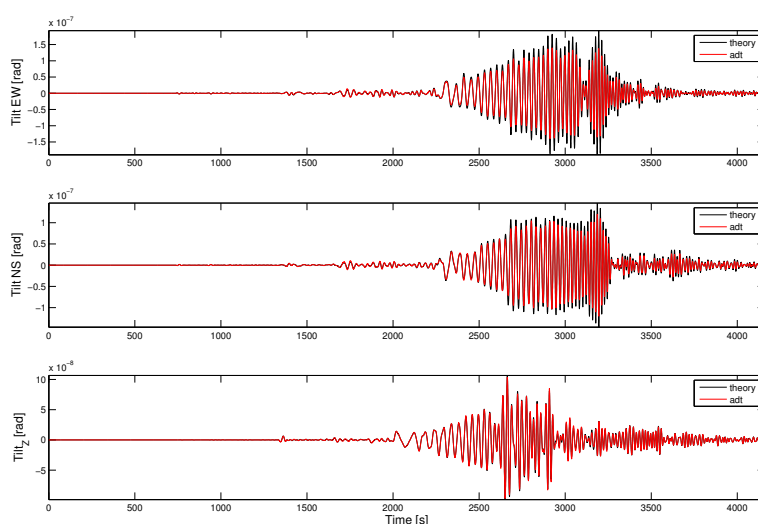


Figure 5.10: Three components of rotation from Synthetic Hokkaido data. The red line is synthetic rotation calculated in the array center (WET) using nine stations including the reference station and black line is array-derived rotation.

5.4.2. Array-derived tilt rate from observed data

The same exercise is then applied to real data, in this case the M6.6 Bam, Iran event and the M7.0 Irian Jaya event. Figure 5.12 shows the array derived tilt (left) and observed tilt (right) from Bam, Iran event, 26 December 2003. As mentioned in Section 5.3, the observed tilt has higher values compared with the array-derived tilt due to the influence of the horizontal acceleration. Moreover,

5.4 Array-derived horizontal components of rotations

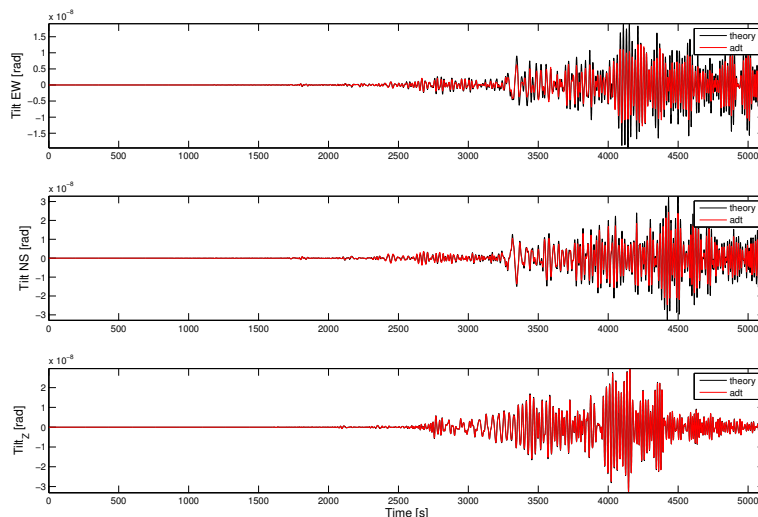


Figure 5.11: Three components of rotation from Synthetic Papua Irian Jaya data. The red line is synthetic rotation calculated in the array center (WET) using nine stations including the reference station and black line is array-derived rotation.

we can not directly compare those two observations as in the case of rotation about the vertical axis which is recorded by the ring laser data.

However, as will be discussed in more detail in the next Section that - assuming plane wave propagation - the radial component of acceleration should be in phase with the transverse component of tilt, we may compare the array-derived tilt with radial acceleration recorded by the broadband sensor. The superimposed plot of the radial component of acceleration and transverse array derived tilt for the observed Bam, Iran event is shown in Figure 5.13. Those events are filtered with a narrow band filter having a central period of 20 s. While some waveform match seems to occur in part of the seismograms, this match is much less pronounced than the one described for rotation around a vertical axis in Chapter 4.

The same exercise is applied to the Irian Jaya event (Figure 5.14). Again, the array derived tilt is smaller than the observed tilt. Figure 5.15 shows the array-derived tilt (green line) in the transverse component superimposed with radial acceleration (red line) bandpass filtered using a narrow band with a central period of 30 s. Here we find again some similarity in the waveform especially for the

5.4 Array-derived horizontal components of rotations

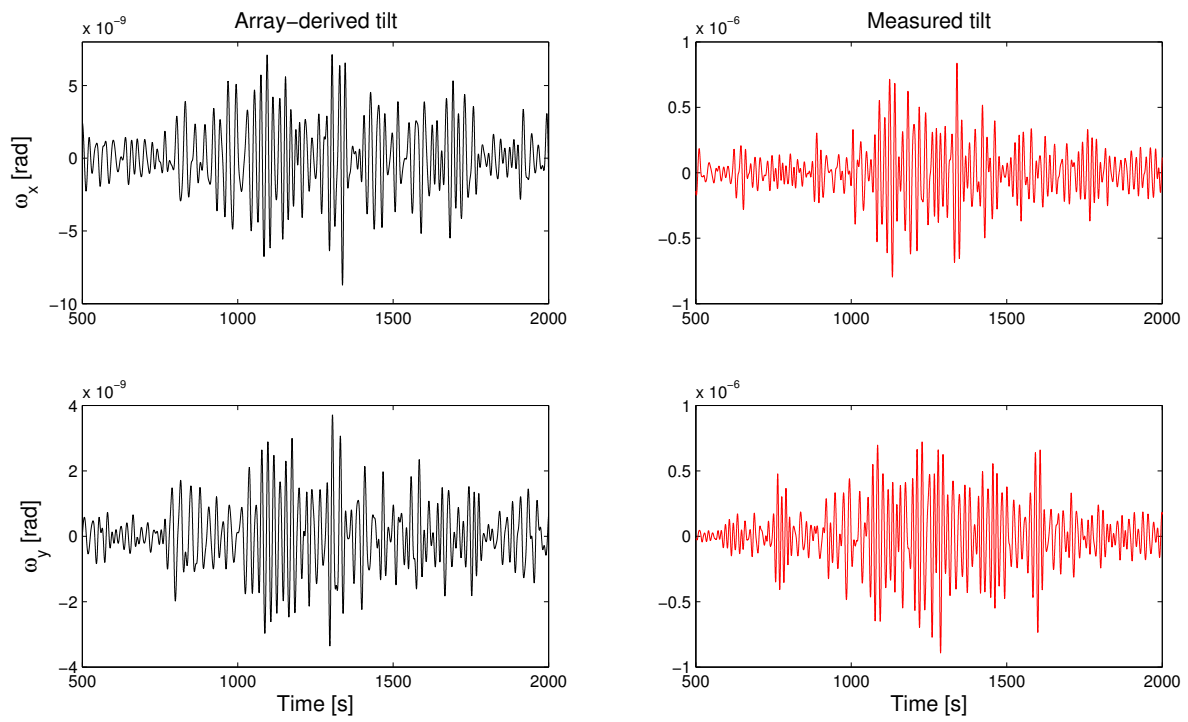


Figure 5.12: The horizontal components of rotation from Bam, Iran event. Left: The array-derived rotation (black). Right: Observed tilt recorded by the tiltmeter (red).

5.5 Rayleigh-Wave Phase velocity from collocated measurements

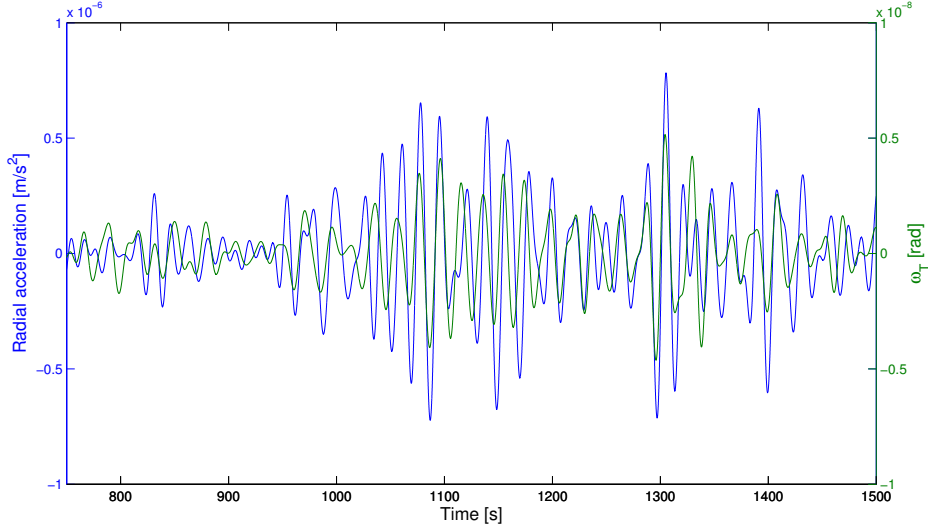


Figure 5.13: Superimposed plot of radial component of acceleration (blue line) versus transverse array-derived tilt (green line) for Bam, Iran event.

Rayleigh wave time window.

As mentioned earlier the amplitude of array-derived tilt and the exact tilt are not the same, at least we find a similarity in the waveform between those two signals. These waveform similarities are supported by the fact that they match with the radial acceleration in the Rayleigh wave time window for a certain frequency band as suggested by the theory. Further analysis especially on the period dependencies are discussed in the next chapter.

5.5. Rayleigh-Wave Phase velocity from collocated measurements

In Chapter 4, it has been shown based on the plane wave assumption that the transverse acceleration and rotation rate are proportional to two times the Love-wave phase velocity. With the same assumption we can do the same exercise for a Rayleigh wave case.

For a simple half-space Poisson solid, the Rayleigh wave displacements are

5.5 Rayleigh-Wave Phase velocity from collocated measurements

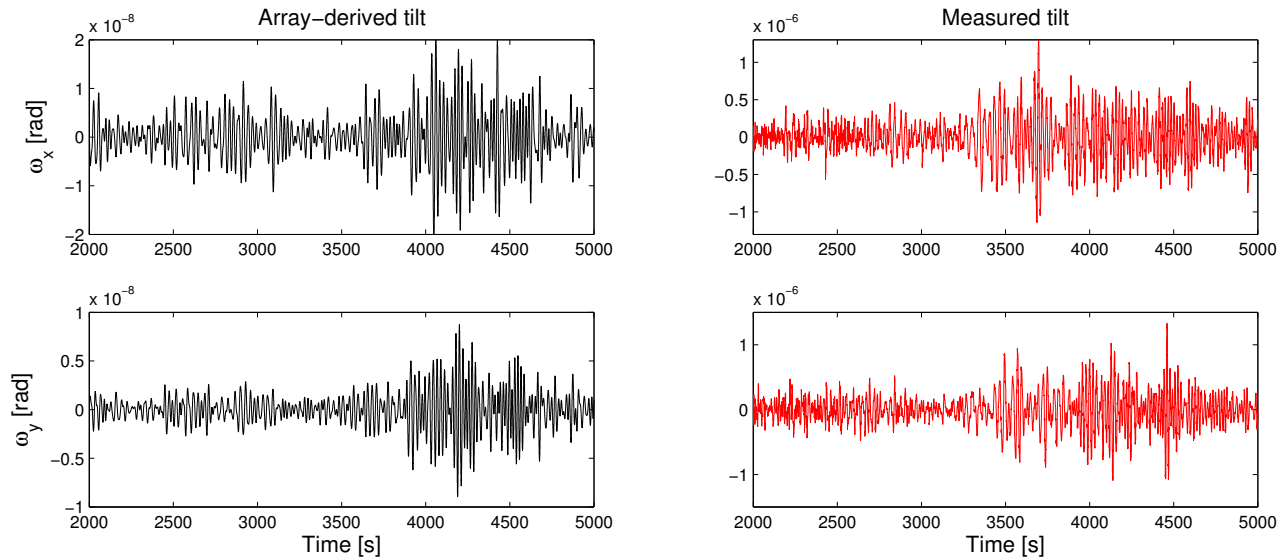


Figure 5.14: Three components of rotation from Irian Jaya event. Left: The array-derived rotation (black). Right: Observed tilt recorded by the tiltmeter (red).

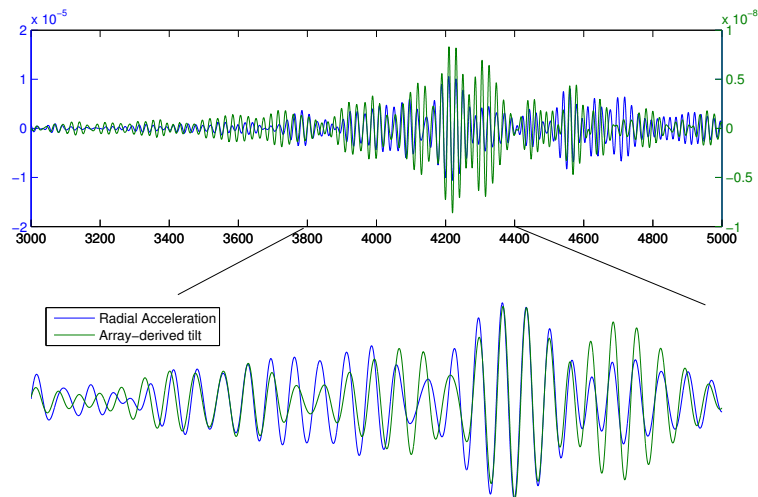


Figure 5.15: Superimposed plot of radial component of acceleration (blue line) versus transverse array-derived tilt (green line) for Papua, Irian Jaya earthquake.

5.5 Rayleigh-Wave Phase velocity from collocated measurements

given by (e.g., Lay & Wallace, 1995):

$$u_x = -0.42Ak \sin(kx - \omega t), \quad u_z = 0.62Ak \cos(kx - \omega t), \quad (5.1)$$

where k is the Rayleigh wavenumber. The acceleration along x is then

$$a_x = 0.42Ak\omega^2 \sin(kx - \omega t). \quad (5.2)$$

With the use of equation (3.1), the y -component of rotation is defined by

$$\Omega_y = -0.31Ak^2 \sin(kx - \omega t). \quad (5.3)$$

Dividing Eq. 5.3 by Eq. 5.2 we then have

$$\frac{a_x}{\Omega_y} = -1.35484 \frac{\omega^2}{k} = -1.35484 c_P \omega. \quad (5.4)$$

From Equation 5.4 it is clear that the transverse rotation should be in phase with the radial acceleration and the amplitude differs by a factor of $c_P \omega$ plus the effects of the medium below the observation point. For a layered or vertically inhomogeneous structure, the Rayleigh wave is dispersive. To study the behavior of the phase velocity (c_P) of the Rayleigh wave as a function of frequency, we can superimpose the radial acceleration and transverse tilt (rotation) for a certain narrow frequency band and calculate the ratio that corresponds to the phase velocity (Equation 5.4). Unfortunately we have no information about tilt rate data, as we have shown that our tiltmeter mainly records horizontal acceleration. Nevertheless, we can do the exercise with synthetic data. Here we will show three synthetic events from Gibraltar, Irian Jaya and Hokkaido.

The experiment result are shown in Figure 5.16, 5.17 and 5.18. In those figures the transverse rotation and radial acceleration are superimposed after filtering with a narrow bandpass (zero-phase Butterworth with corner frequencies $0.85*1/T$ Hz and $1.15*1/T$ Hz, where T is the dominant period in seconds). The appropriate phase velocity (given at the top of each trace pair) is obtained by dividing the peak amplitudes with a scaling of about 1.35484 times the dominant frequency.

A good fit is observed especially in the range above period of 40 s. We also observe that the estimated phase velocities have tendencies toward higher values

5.5 Rayleigh-Wave Phase velocity from collocated measurements

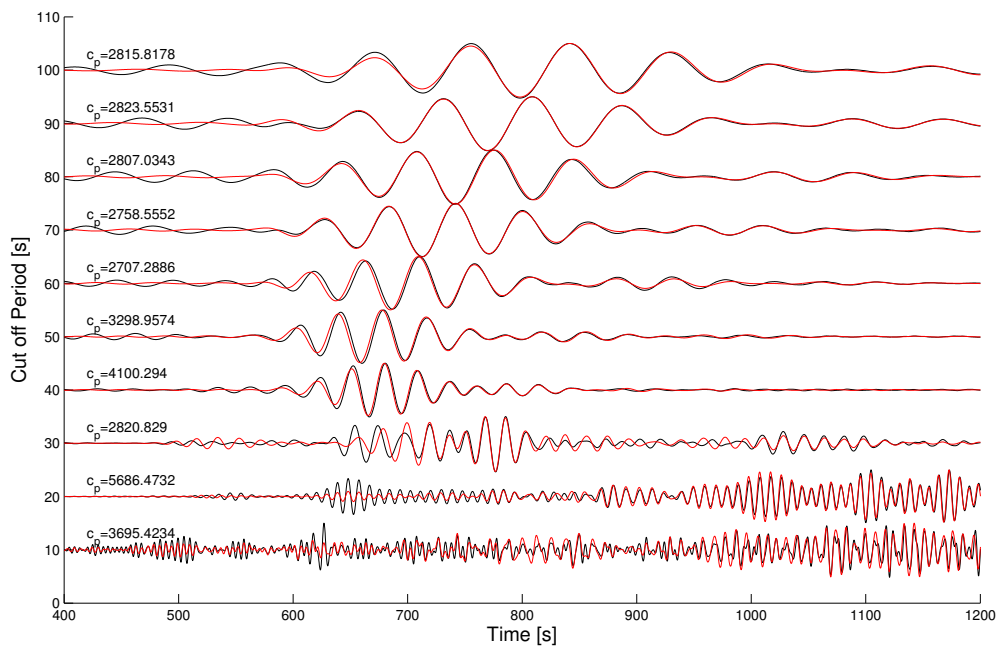


Figure 5.16: Superposition of radial acceleration (black) and transverse tilt (red) and determination of rayleigh wave phase velocities as a function of dominant period after narrow-band filtering (see text for details). The phase velocities given for each trace pair were determined by dividing the peak radial acceleration by the peak tilt rate (and corrected for the factor of the cut off period). Synthetic event in Gibraltar, M6.3, 24 February, 2004.

5.5 Rayleigh-Wave Phase velocity from collocated measurements

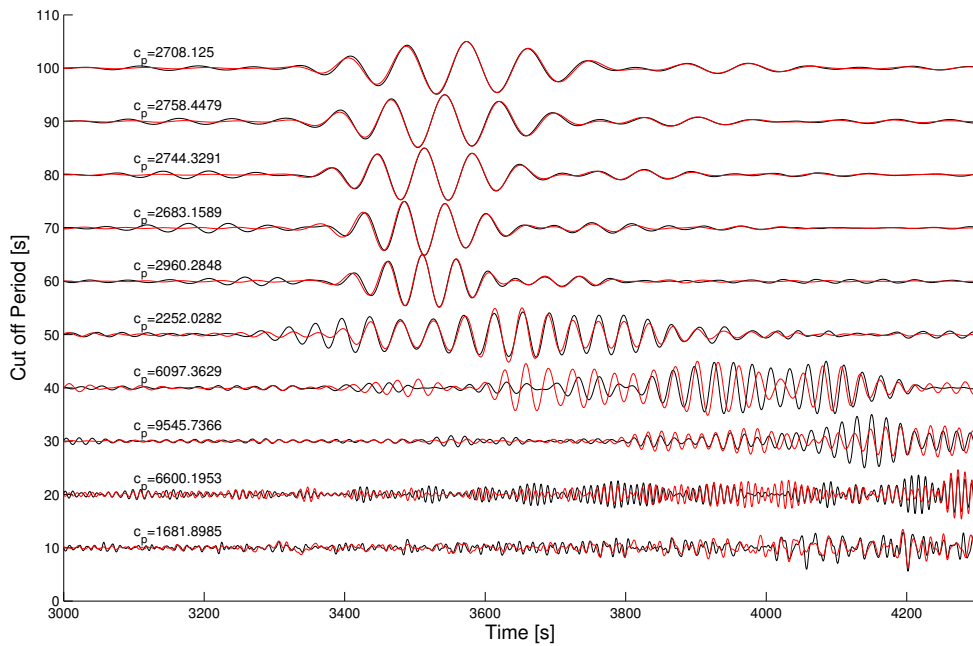


Figure 5.17: Superposition of radial acceleration (black) and transverse tilt (red) and determination of rayleigh wave phase velocities as a function of dominant period after narrow-band filtering (see text for details). The phase velocities given for each trace pair were determined by dividing the peak radial acceleration by the peak tilt rate (and corrected for the factor of the cut off period). Synthetic event in Irian Jaya, M7.1, 07 February, 2004.

as the period gets larger. From those figures, we observe a strong evidence of a potential application of measuring the rotation about the horizontal axis (tiltI) to study the dispersive behavior of Rayleigh wave using single station analysis. For realdata, we may do the same exercise with the array-derived tilt since we have no observed exact tilt data. As discussed in Chapter 3, during the array experiment we captured at least three events which are simultantly recorded by the seismometers and ring laser (Table 3.1). Here we will use those three events to estimate the phase velocity using collocated measurements of radial acceleration. Note that we use the signal after corection with the broadband's instrument sensor. Therefore we may only possible to analyze the signal with the frequency greater than 0.03 Hz, since we highpass filtered the signal during the processing with a cut off frequency of 0.03 Hz.

The experiment results are shown in Figure 5.19, 5.20, 5.21. We use the same narrow bandpass filter as used in the synthetic studies. The waveform match especially in the Rayleigh wave time window and at the cut off period of around 20 s - 30 s. For higher periods, although the waveform seems to be similar, they are out of phase. The estimated phase velocity are found around 5000 m/s. This result suggest the importance of having an acceleration-free-type of tiltmeter with a broadband dynamic range.

5.6. Tilt-corrected ring laser data

In Section 2.3.3 we have shown that based on Equation 2.15, the variation in the orientation of the ring laser basement will generate a signature in the ring laser data. Therefore, tilt data are needed for correction of the rotational data because this orientation changes. Those changes can be converted to the equivalent rotation according to the expression (e.g., Schreiber *et al.*, 2005)

$$\Omega_{TILT} = (\Omega \cdot \sin(\varphi) \cos(T_{NS}) - \Omega \cdot \cos(\varphi) \sin(T_{NS})) \cdot \cos(T_{EW}), \quad (5.5)$$

where Ω_{TILT} is the tilt equivalent rotation rate, Ω is the rotation rate biased by the Earth rotation, φ is the ring laser location latitude, T_{NS} and T_{EW} are instrument tilt in North-South and East-West directions respectively. Since the East-West tilt components is part of the cosine function, which is usually very

5.6 Tilt-corrected ring laser data

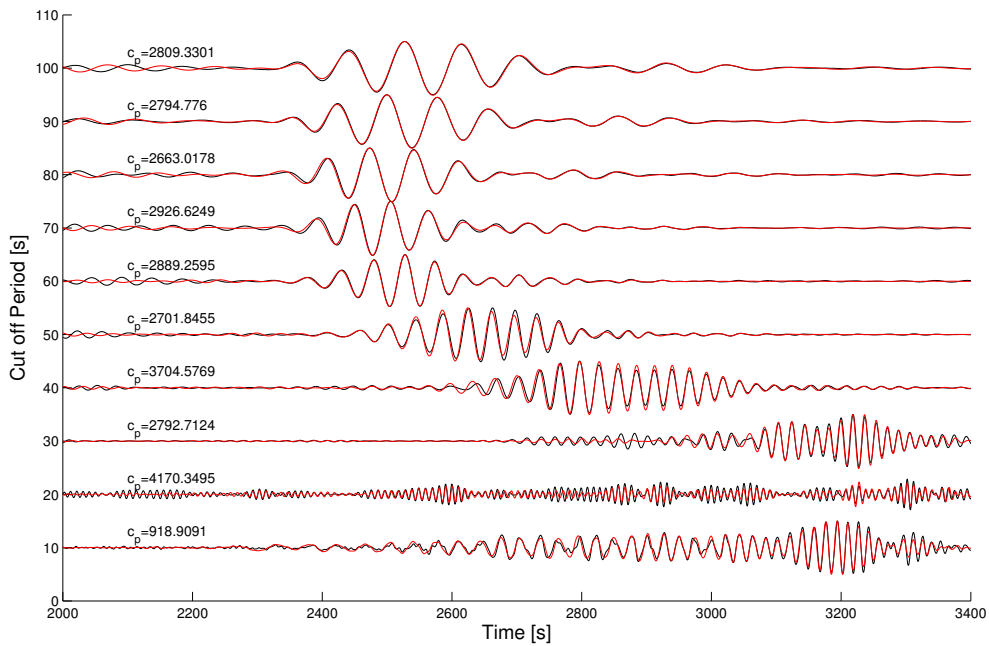


Figure 5.18: Superposition of radial acceleration (black) and transverse tilt (red) and determination of rayleigh wave phase velocities as a function of dominant period after narrow-band filtering (see text for details). The phase velocities given for each trace pair were determined by dividing the peak radial acceleration by the peak tilt rate (and corrected for the factor of the cut off period). Synthetic event in Hokkaido, M8.3, 25 September, 2003.

5.6 Tilt-corrected ring laser data

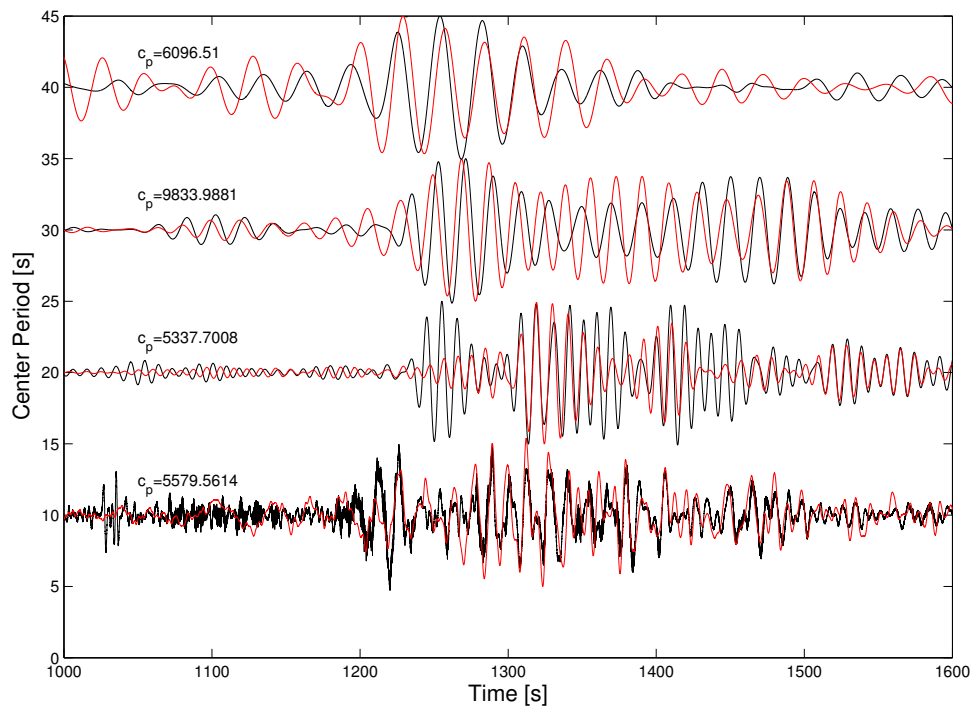


Figure 5.19: Superposition of radial acceleration (black) and transverse tilt (red) and determination of Rayleigh wave phase velocities as a function of dominant period after narrow-band filtering (see text for details). Al Hoceima event, M6.3, 24 February 2004.

5.6 Tilt-corrected ring laser data

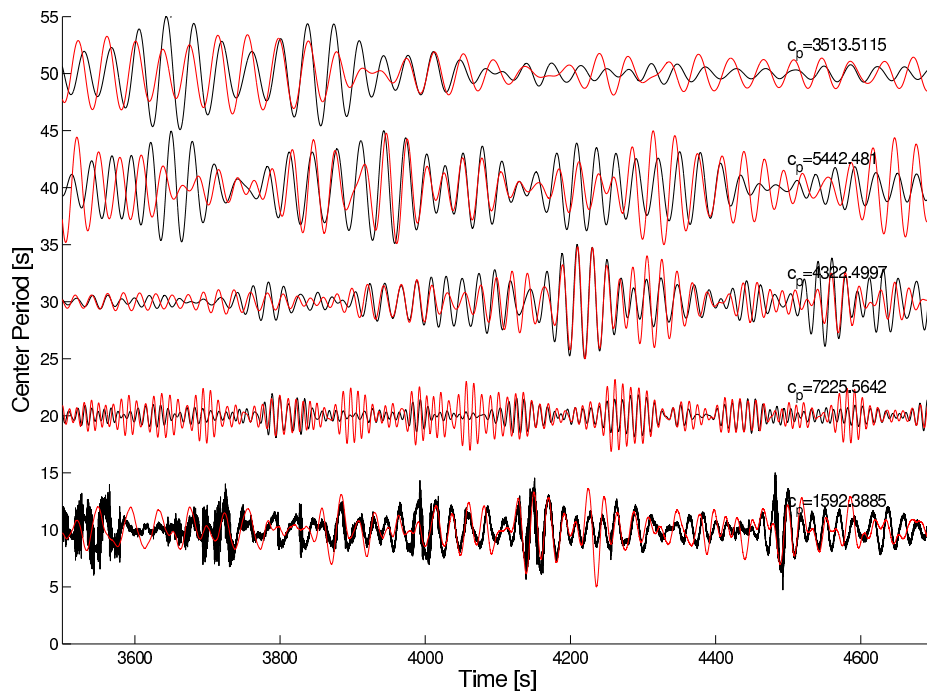


Figure 5.20: Superposition of radial acceleration (black) and transverse tilt (red) and determination of Rayleigh wave phase velocities as a function of dominant period after narrow-band filtering (see text for details). Papua, Irian Jaya event, M7.3, 7 February 2004.

5.6 Tilt-corrected ring laser data

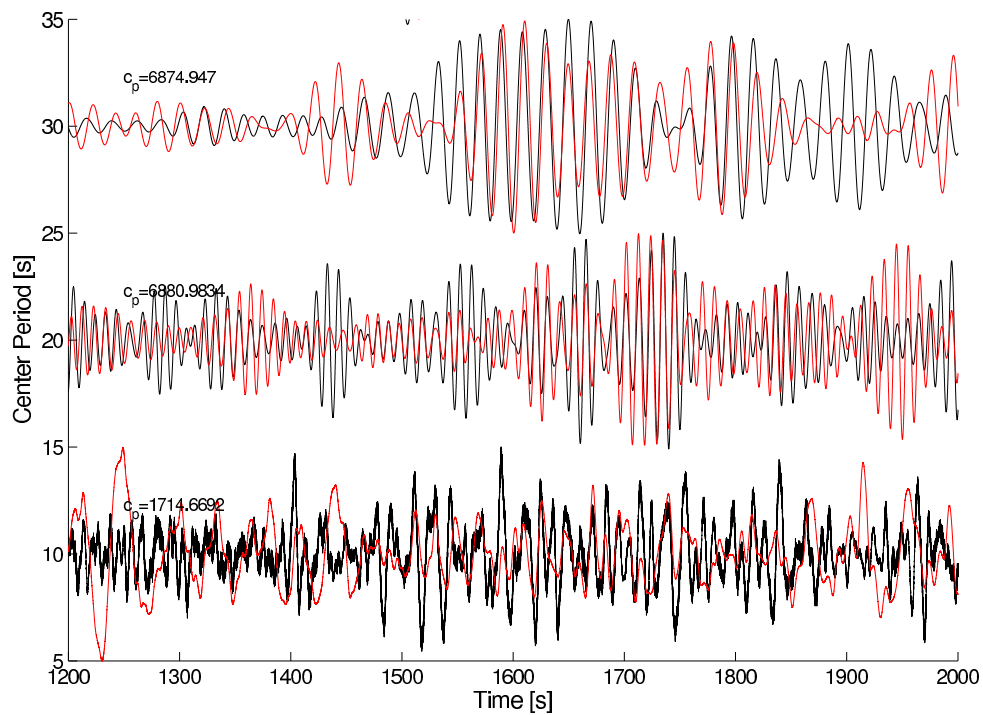


Figure 5.21: Superposition of radial acceleration (black) and transverse tilt (red) and determination of Rayleigh wave phase velocities as a function of dominant period after narrow-band filtering (see text for details). Bam, Iran event, M6.3, 26 December 2003.

5.6 Tilt-corrected ring laser data

small, it can be ignored for all practical purpose, therefore the previous expression reduces to

$$\Omega_{TILT} = \Omega \sin(\varphi - T_{NS}) \quad (5.6)$$

As was shown in a previous Section, that tiltmeter data recorded in Wettzell are dominated by the horizontal accelerations, the tilt correction will be substantially overestimated. A simple experiment will show those assumptions and quantify the effects of horizontal acceleration to the tilt correction. I will use two synthetic data from Hokkaido and Papua events to doing those exercises. From Equation 5.6, we may calculate the tilt correction using real exact tilt and tilt as is recorded by a tiltmeter (i.e. horizontal acceleration divided by gravity). The two plots of tilt correction for the Hokkaido event is shown in Figure 5.22. The upper part of Figure 5.22 shows the tilt corrections if we use tiltmeter data and the lower part is if we use the exact tilt rate data. The same procedure was applied to

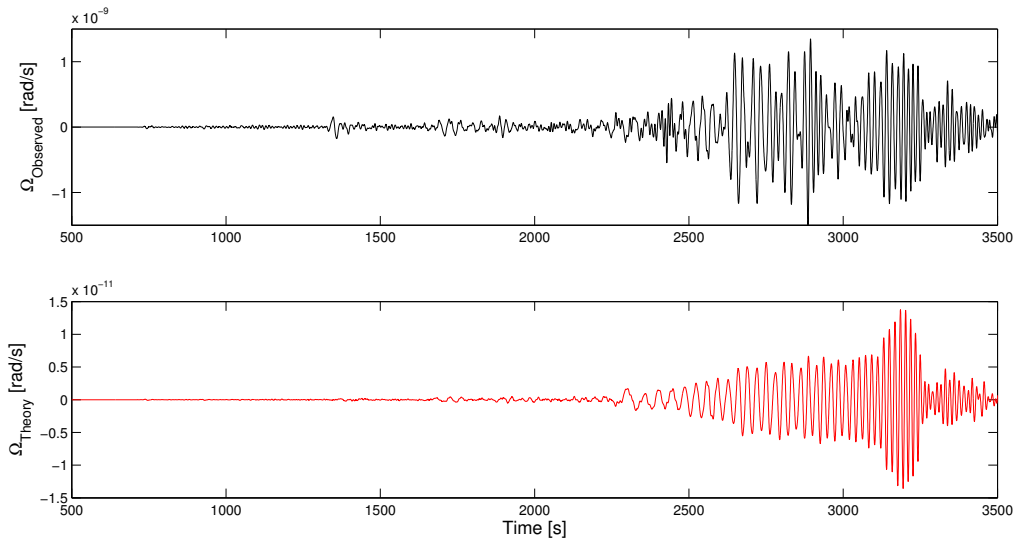


Figure 5.22: Tilt correction for Hokkaido synthetic event. Upper plot: tilt correction assumed tilt rate was obtained with tiltmeter, lower part: tilt correction using pure tilting rate.

the Irian Jaya synthetic event (Figure 5.23). As in the previous case, the upper part of Figure 5.23 shows the tilt corrections if we use tiltmeter data and the

lower part is if we use the exact tilt rate data. From those two examples it is

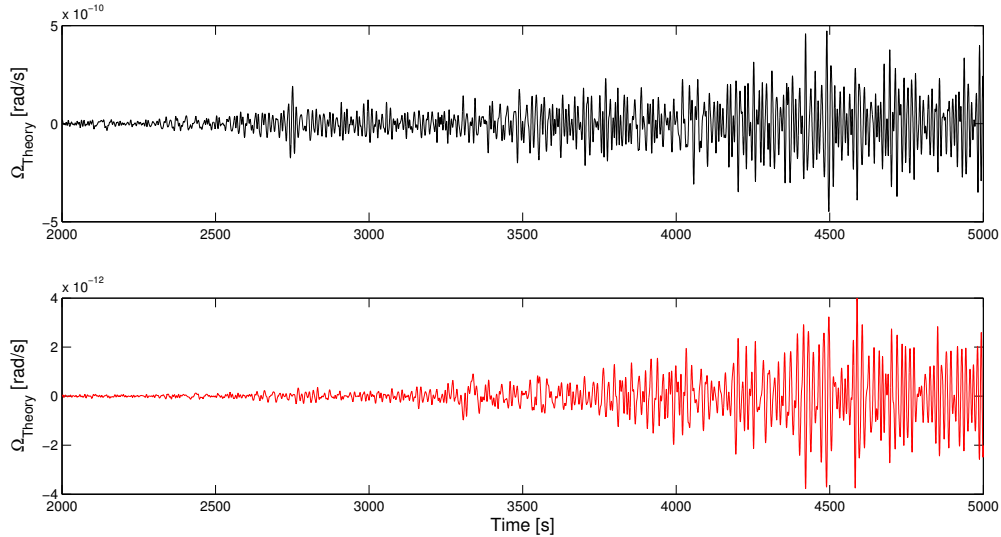


Figure 5.23: Tilt correction for Irian Jaya synthetic event. Upper plot: tilt correction assumed tilt rate was obtained with tiltmeter, lower part: tilt correction using pure tilting rate.

clear that the tilt correction calculated using tilt rate recorded by tiltmeter will causes an overestimated calculation by a factor of about 100 times larger. Many reports or papers on ring laser mentioned that the effects of tilt on the ring laser data is about 5% (e.g., Schreiber *et al.*, 2005, 2006). As demonstrated here the actual effects may be more than 100 times smaller. Since the tilt correction is very small, it may be unnecessary to apply a tilt correction except for very large events or in strong motion studies. However, from an instrumental point of view, it will open up a new discussion about how to remove the tilt effect on the ring laser instruments.

5.7. Conclusion

The effect of tilt is generally small but not negligible in seismology, especially in strong-motion earthquakes. It is well known that the tilt signal is most noticeable

in the horizontal components of the seismometer. Ignoring the tilt effects leads to unreliable results, especially in the calculation of permanent displacements and long-period motions. It appears that full measurement of six components of the motion (three translations and three rotations) is necessary in the near-field study.

It is still an open question what technology is best suitable for measuring various components of rotation. The optical devices could be advantageous compared to classical tiltmeters for the rotation about a horizontal axis as well (regardless of meteorological characteristics- accuracy, sensitivity, etc-which remain to be assessed). Indeed, classical tiltmeters measure a change of angle with respect to the local vertical, determined by gravity; thus, they cannot discriminate between true rotation and pure change in the local gravity (e.g. due to mass redistribution).

A study of deriving tilt data from array data show that there may be a fundamental relation we do not really know yet, that must be included in the array-derived tilt calculation. Although in the overall time series, the array-derived tilt and the theoretical tilt waveform match quite well, an amplitude discrepancy is shown especially for the regional event (in this case Gibraltar event).

An interesting result concerning tilt study is the possibility to derive the Rayleigh wave phase velocity and potentially Rayleigh wave dispersion curve from collocated measurement of tilt rate and translational motions. Synthetic studies show that there is a frequency dependent phase velocity determined from collocated radial acceleration and transverse tilt. Further analysis including real data with many earthquake events and comparison with another technique such as array study will be necessary.

Tilt correction for ring laser data leads to an effect about 100 times larger when using tilt records from the tiltmeter. This is because the tiltmeter, which is a pendulum type sensor, is susceptible to horizontal accelerations. Since there is a very small value of tilt effects on the ring laser data especially for teleseismic event, the tilt correction procedure seems not necessary to be applied.

6. Conclusions and Outlook

”Three different types of sensor are needed in seismology: the inertial sensor, which is sensitive to acceleration; the strainmeter, which measures strain in the Earth beneath it; and various sensor for measuring rotation.”

Aki & Richards (2002)

6.1. Conclusions

This thesis intends to study the relevance of rotational ground motion in seismology. The rotational part of earthquake-induced ground motion has basically been ignored in the past decades, compared to the substantial research in translational ground motion. Even though there are theoretical considerations that suggest that the observation of rotational motions may indeed be useful and provide additional information.

In this thesis we successfully show that rotational motions can be derived from array of seismometers by comparing directly the array-derived rotation rate (about a vertical axis) with ring laser data.. We also noted that deriving rotation rate using minimally required three stations might give a wrong result due to the noise effects. In this case, a direct rotation sensor are needed to record the ground rotation rate induced by earthquake. Compared to other types of rotational sensors, the optical device (i.e. ring laser) is the way to go. For the near future, it is important to continue improving the rotational sensors, especially reducing the instrument size but keeping the appropriate resolution for use in local and regional seismology.

The potential applications of rotational data are also studied during this thesis. The most important contribution is the possibility to derive the phase velocity dispersion curve below the observation point using spectral ratio from collocated measurements of translations and rotations. From collocated measurements it is also possible to determine the direction of wave propagation and the phase velocity in the time domain that usually only accessible through array data. Further research to invert the dispersion curve to obtain the structure below the observation point will be carried out in the future.

For tilt data, we show that in the frequency range of earthquake, the pendulum based tiltmeter was recording mainly the horizontal accelerations. Therefore, we will get bigger tilt signal than the actual tilt signal. For consequences, if we use this tilt data to correct the ring laser data, it will make the correction is about 100 times larger than the actual correction. This is a strong statement since several papers on ring laser observations so far mentioned that the effect of tilt on the ring laser data is about 5%. Although in theory there is a possibility to derive the tilt rate using array data, we have difficulties to obtain the array-derived tilt with exactly the same amplitude with the theoretical tilt.

6.2. Outlook

Based on this study there are many open questions remaining. The ring laser has provided a fully consistent data for seismological application. However, it is still not possible to be used as a mobile instrument especially because its size. A fiber optic gyro may become an alternative choice to reduce the size of the instrument. The array-derived rotation rate, at least for the component about the vertical axis can be used for calibrating any of new rotational sensors. With a more proper array setup, the accuracy of the rotational motion may be increased.

It has been shown in this thesis that from collocated measurement of rotations and translations we can determine the dispersion curve below the observational point. Nevertheless, further verification in a more systematic way is needed. It is also interesting to study the possibility to analyze higher frequency signals

to mapping the more shallow velocity structure. This may be useful for the earthquake engineering field.

Our study will give an impact to other research fields such as strong motion seismology, earthquake source studies or earthquake engineering studies. They should also include rotational motion in their observations. This will be possible especially when a more compact three components rotational sensor is available.

A. Contents of the Attached DVDs

- /
- CODE Script used for processing the data
 - mathematica Analytical solutions
 - matlab useful scripts for processing
- DATA Tarballs of the data
 - OBS Tarballs of observed data:
 - Hokkaido event
 - Gibraltar event
 - Papua, Irian Jaya event
 - SH-AXI SH AXI Symmetry synthetic data
 - SYN SPECFEM-3D data

References

- AGNEW, D.C. (1986). Strainmeters and tiltmeters. *Reviews of Geophysics*, **24**, 579–624. 32, 81, 82
- AKI, K. (1965). A note on the use of microseisms in determining the shallow structures of the earth's crust. *Geophysics*, **30**, 665–666. 64
- AKI, K. & RICHARDS, P. (2002). *Quantitative Seismology – Second Edition*. University Science Books, Sausalito, California. 7, 9, 11, 12, 61, 64, 80, 84, 107
- AWAD, A.M. & HUMAR, J.L. (1984). Dynamic response of buildings to ground rotational motions. *Canadian Journal of Civil Engineering*, **11**, 48–56. 1
- BASSIN, C., LASKE, G. & MASTERS, G. (2000). The current limits of resolution for surface wave tomography in north america. *EOS Trans. AGU*, F897. vi, 41, 42, 75, 89
- BENNETT, R.A., RODI, W. & REILINGER, R.E. (1996). Global positioning system constraints on fault slip rates in southern California and northern Baja, Mexico. *J. Geophys. Res.*, **101**, 21,943–21,960. 28
- BODIN, P., GOMBERG, J., SINGH, S.K. & SANTOYO, M. (1997). Dynamic deformation of shallow sediments in the valley of Mexico, part i: Three-dimensional strains and rotations recorded on a seismic array. *Bull. Seism. Soc. Am.*, **87**, 528–539. 4, 32, 40, 57
- BOUCHON, M. & AKI, K. (1982). Strain, tilt, and rotation associated with strong ground motion in the vicinity of earthquake faults. *Bull. Seism. Soc. Am.*, **72**, 1717–1738. 1
- CAMPILLO, M. & PAUL, A. (2003). Long range correlations in the diffuse seismic coda. *Science*, **299**. 61
- COCHARD, A., IGEL, H., SCHUBERTH, B., SURYANTO, W., VELIKOSELTSEV, A., SCHREIBER, U., WASSERMANN, J., SCHERBAUM, F. & VOLLMER, D. (2006). Rotational motions in seismology:theory, observation, simulation. In

References

- R. Teisseyre, M. Takeo & E. Majewski, eds., *Earthquake source asymmetry, structural media and rotation effects*, Springer Verlag, Berlin Heidelberg. 7, 62, 72
- DAVIDSON, C. (1927). *The Founders of Seismology*. Cambridge university press. 1
- DUNN, R.W., SHABALIN, D.E., THIRKEELE, R.J., MACDONALD, G.J., STEDMAN, G.E. & SCHREIBER, K.U. (2002). Design and initial operation of a 367-m rectangular ring laser. *Applied Optic*, **41**, 1685–1688. 84
- EVANS, J.R., COCHARD, A., GRAZIER, V., HUANG, B.S., HUDNUT, K.W., HUTT, C.R., IGEL, H., LEE, W.H.K., LIU, C.C., NIGHBOR, R., SAFAK, E., SAVAGE, W.U., SCHREIBER, U., TRIFUNAC, M., WASSERMANN, J. & WU, C.F. (2006). A workshop on rotational ground motion. *Seismol. Res. Lett. (Submitted)*. xx, 79
- FARRELL, W.E. (1969). A gyroscopic seismometer: Measurements during the Bortego earthquake. *Bull. Seism. Soc. Am.*, **59**, 1239–1245. 84, 85
- FRIEDERICH, W. (1999). Propagation of seismic shear and surace waves in a laterally heterogeneous mantle by multiple forward scattering. *Geophys. J. Int.*, **136**, 180–204. 60
- FRIEDERICH, W. & HUANG, Z.X. (1996). Evidence for upper mantle anisotropy beneath southern germany from love and rayleigh wave dispersion. *Geophys. Res. Lett.*, **23**, 1135–1138. 64
- GHAYAMGHAMIAN, M.R. & MATOSAKA, M. (2003). The effects of torsional and motion coupling in site response estimation. *Earthquake Engng. Struct. Dyn.*, **32**, 691–709. 29
- GOMBERG, J. & AGNEW, D. (1996). An evalutation using strainmeter and seismometer data from Pinon flat Observatory. *Bull. Seism. Soc. Am.*, **86**, 212–220. 62
- GORDON, D.W., BENNETT, T.J., HERRMANN, R.B. & ROGERS, A.M. (1970). The south-central Illionis earthquake of November 9, 1968: Macro-seismic studies. *Bull. Seism. Soc. Am.*, **60**, 953–971. iv, 2
- GOULTY, N.R. (1976). Strainmeters and tiltmeters in geophysics. *Tectonophysics*, **34**, 245–256. 81
- GRAIZER, V.M. (2005). Effects of tilt on strong motion data processing. *Soil Dyn. Earthquake Eng.*, **25**, 197–204. 4, 81

- GUTENBERG, B. (1959). *Physics of the Earth's Interior*. Academic Press. 1
- HAO, H. & DUAN, X.N. (1995). Seismic response of asymmetric structures to multiple ground motions. *Journal of structural engineering*, **121**, 1557–1564. 28
- HART, G.C., DIJULIO, R.M. & LEW, M. (1975). Torsional response of high-rise buildings. *ASCE, Journal of the Structural Division*, **101**, 397–415. 1
- HOBBS, W.H. (1907). *Earthquakes*. Appleton. 1
- HUANG, B.S. (2003). Ground rotational motions of the 1999 Chi-Chi, Taiwan earthquake as inferred from dense array observations. *Geophys. Res. Lett.*, **30**, 1307–1310. 4, 33, 40
- HUDNUT, K., BEVIS, M., BRZEZINSKA, D.G., JI, C., KENDRICK, K., SAFAK, E., SANCHEZ, R. & TOTH, C. (2004). Mapping and detection of fault slip and structural damage. In *2nd International Workshop on Remote Sensing for Post-Disaster Response*. 28
- IGEL, H., SCHREIBER, U., FLAWS, A., SCHUBERTH, B., VELIKOSELTSEV, A. & COCHARD, A. (2005). Rotational motions induced by the m8.1 Tokachi-Oki earthquake, September 25, 2003. *Geophys. Res. Lett.*, **32**, L08309. xix, xx, 3, 4, 30, 33, 62, 66, 67
- IGEL, H., COCHARD, A., WASSERMANN, J., FLAWS, A., SCHREIBER, U., VELIKOSELTSEV, A. & NGUYEN, P.D. (2007). Broadband observations of earthquake induced rotational ground motions. *Geophys. J. Int.*. xix, 26, 62, 67, 71, 72
- IMAMURA, A. (1937). *Theoretical and Applied Seismology*. Maruzen. 1
- Ji, C. (2004). <http://gps.caltech.edu/~jichen>. 89
- KENNETT, B.L.N., ENGDAHL, E.R. & BULAND, R. (1995). Constraints on seismic velocities in the Earth from travel-times. *Geophys. J. Int.*, **122**, 108–124. 60, 75
- KIND, F., FÄH, D. & GIARDINI, D. (2005). Array measurements of s-wave velocities from ambient vibrations. *Geophys. J. Int.*, **160**, 114–126. 61
- KOMATITSCH, D. & TROMP, J. (2002a). Spectral-element simulations of global seismic wave propagation -II. 3D models, oceans, rotation, and self gravitation. *Geophys. J. Int.*, **150**, 303–318. vi, 41, 42, 75

-
- KOMATITSCH, D. & TROMP, J. (2002b). Spectral-element simulations of global seismic wave propagation-I. Validation. *Geophys. J. Int.*, **149**, 390–412. vi, 41, 42, 75
- LAY, T. & WALLACE, T.C. (1995). *Modern Global Seismology*. Academic Press, San Diego, Calif. viii, 65, 96
- LEGRAND, D. (2003). A short note on the selection of the fault plane, the seismic moment tensor, the strain and rotational tensor, and the gradient of displacement. *Bull. Seism. Soc. Am.*, **93**, 946–947. 30
- LI, H., SUN, L. & WANG, S. (2001). Improved approach for obtaining rotational components of seismic motion. In *Transactions, SMiRT16*, Washington DC. 1, 4
- LYONS, S. & SANDWELL, D. (2003). Fault creep along the southern San Andreas from InSAR, permanent scatterers, and stacking. *J. Geophys. Res.*, **108**, 2047–2071. 28
- MCLEOD, D.P., STEDMAN, G.E., WEBB, T.H. & SCHREIBER, U. (1998). Comparison of standard and ring laser rotational seismograms. *Geophys. J. Int.*, **88**, 1495–1503. 3, 30, 61, 62
- MELCHIOR, P. (1983). *The Tides of the planet Earth*. Pergamon, New York. 84
- MIKUMO, T. & AKI, K. (1964). Determination of local phase velocity by inter-comparison of seismograms from strain and pendulum instruments. *J. Geophys. Res.*, **69**, 721–731. 62
- MILANA, G., BARBA, S., DEL PEZZO, E. & ZAMBONELLI, E. (1996). Site response from ambient noise measurements: new perspectives from an array study in central italy. *Bull. Seism. Soc. Am.*, **86**, 320–328. 61
- MORIYA, T. & MARUMO, R. (1998). Design for rotational seismometers and their calibration. *Geophys. Bull. Hokkaido Univ.*, 99–106. xiii, 18
- MORTENSEN, C.E. & IWATSUBO, E.Y. (1986). Short-term tilt anomalies preceding local earthquakes near san jose, california. *Bull. Seism. Soc. Am.*, 2221–2228. 83
- NATAF, H.C., NAKANISHI, I. & ANDERSON, D.L. (1984). Anisotropy and shear velocity heterogeneities in the upper mantle. *Geophys. Res. Lett.*, **11**, 109–112. 61

-
- NEWMARK, N.M. (1969). Torsion in symmetrical buildings. *Proc. Fourth World Conference on Earthquake Engineering, Santiago, Chile*, **3**, 19–32. 1, 28
- NIAZI, N. (1986). Inferred displacements velocities and rotations of a long rigid foundation located at El Centro differential array site during the 1979 Imperial Valley, California earthquake. *Earthquake Eng. Struct. Dyn.*, **14**, 531–542. 4
- NIGBOR, R.L. (1994). Six degree - of - freedom ground - motion measurements. *Bull. Seism. Soc. Am.*, **84**, 1665–1669. xviii, 3, 21, 30
- OLIVEIRA, C.S. & BOLT, B.A. (1989). Rotational components of surface strong ground motion. *Earthquake Eng. Struct. Dyn.*, **18**, 517–526. 4
- PANCHA, A., WEBB, T.H., STEDMAN, G.E., MCLEOD, D.B. & SCHREIBER, U. (2000). Ring laser detection of rotations from teleseismic waves. *Geophys. Res. Lett.*, **27**, 3553–3556. 3, 30, 61, 62
- POST, E.J. (1967). Sagnac effect. *Review of Modern Physics*, **39**, 475–493. 3
- PRESS, W.H., TEUKOLSKY, S.A., VETTERLING, W.T. & FLANNERY, B.P. (2002). *Numerical Recipes in Fortran 90, The Art of Scientific Computing*. Cambridge University Press, Cambridge, 2nd edn. 75
- RICHTER, C.F. (1958). *Elementary Seismology*. W.H. Freeman and Company, San Francisco. 1
- RITSEMA, J. & VAN HEIJST, H.J. (2000). Seismic imaging of structural heterogeneity in the Earths mantle: evidence for large-scale mantle flow. *Sci. Progr.*, **83**, 243–259. vi, 41, 42, 75, 89
- SANDERS, G.A., PRENTISS, M.G. & EZEKIEL, S. (1981). Passive ring resonator method for sensitive inertial rotational measurements in geophysical and relativity. *Optic Letters*, **6**, 569–571. 3
- SCHERBAUM, F. & JOHNSON, J. (1992). *Programmable Interactive Toolbox for Seismological Analysis (PITSA)*. IASPEI Software Library, 5. 36
- SCHREIBER, K.U., KLÜGEL, T. & STEDMAN, G.E. (2003). Earth tide and tilt detection by a ring laser gyroscope. *J. Geophys. Res.*, **108**, 2132. 27, 35, 71
- SCHREIBER, U., IGEL, H., COCHARD, A., VELIKOSELTSEV, A., FLAWS, A., SCHUBERTH, B., DREWITZ, W. & MÜLLER, F. (2005). *Geotechnologies-book*. Springer Verlag. 23, 26, 35, 62, 71, 99, 105

-
- SCHREIBER, U., STEDMAN, G.E., IGEL, H. & FLAWS, A. (2006). Rotational motions in seismology: theory, observation, simulation. In R. Teisseyre, M. Takeo & E. Majewski, eds., *Earthquake source asymmetry, structural media and rotation effects*, Springer Verlag, Berlin Heidelberg. 62, 105
- SCHUBERTH, B., IGEL, H., WASSERMANN, J., COCHARD, A. & SCHREIBER, U. (2004). Rotational Motions from Teleseismic Events - Modelling and Observations. *AGU Fall Meeting Abstracts*, B1057. 41
- SHAPIRO, N.M. & CAMPILLO, M. (2004). Emergence of broadband rayleigh wave from correlations of the ambient seismic noise. *Geophys. Res. Lett.*, **31**, L07614, doi:10.1029/2004GL019491. 61
- SHAPIRO, N.M., CAPILLO, M., STEHLY, M. & RITZWOLLER, H. (2005). High-resolution surface wave tomography from ambient seismic noise. *Science*, **307**, 1615–1618. 61
- SINGH, S.K., SANTOYO, M., BODIN, P. & GOMBERG, J. (1997). Dynamic deformations of shallow sediments in valley of Mexico, part ii: Single-station estimates. *Bull. Seism. Soc. Am.*, **87**, 540–550. 4
- SNIEDER, R. (1988a). Large scale waveform inversion of surface waves for lateral heterogeneity, 1, theory and numerical examples. *J. Geophys. Res.*, **93**, 12055–12065. 61
- SNIEDER, R. (1988b). Large scale waveform inversion of surface waves for lateral heterogeneity, 2, application to surface waves in europe and mediterranean. *J. Geophys. Res.*, **93**, 12067–12080. 61
- SOLARZ, L., KRAJEWSKI, Z. & JAROSZEWICZ, L. (2004). Analysis of seismic rotations detected by two antiparallel seismometers: spline function approximation of rotation and displacement velocities. *Acta Geophys. Pol.*, **52**, 197–217. v, xiii, 18, 19
- SPUDICH, P., STECK, L.K., HELLWEG, M., FLETCHER, J.B. & BAKER, L.M. (1995). Transient stresses at Parkfield, California, produced by the M7.4 Landers earthquake of June 28, 1992: Observations from UPSAR dense seismograph array. *J. Geophys. Res.*, **100**, 675–690. 4, 33, 40, 41, 57, 62
- STEDMAN, G.E. (1997). Ring laser tests of fundamental physics and geophysics. *Rev. Progr. Phys.*, **60**, 615–688. 22
- STEDMAN, G.E., LI, Z. & BILGER, H.R. (1995). Sideband analysis and seismic detection in large ring laser. *Appl. Opt.*, **34**, 7390–7396. xix, 3, 23, 30, 61

-
- STICH, D., DE LIS MANCILLA, F., BAUMONT, D. & MORALES, J. (2005). Source analysis of the M_w 6.3 2004 Al Hoceima earthquake (Morocco) using regional apparent source time functions. *J. Geophys. Res.*, **110**, B06306, doi:10.1029/2004JB003366. 38
- SURYANTO, W., IGEL, H., WASSERMANN, J., COCHARD, A., VOLLMER, D., SCHERBAUM, F., VELIKOSELTSEV, A. & SCHREIBER, U. (2006). First comparison of array-derived rotational ground motions with direct ring laser. *Bull. Seism. Soc. Am.*, **96**. 32, 62
- TAKEO, M. (1998). Ground rotational motions recorded in near-source region of earthquakes. *Geophys. Res. Lett.*, **25**, 789–792. xviii, 21, 61
- TAKEO, M. & ITO, H.I. (1997). What can be learned from rotational motions excited by earthquake? *Geophys. J. Int.*, **129**, 319–329. 60
- TEISSEYRE, R., SUCHCICKI, J., TEISSEYRE, K.P., WISZNIOWSKI, J. & PALAGIO, P. (2003). Seismic rotation waves: basic elements of theory and recording. *Annals. of Geophys.*, **46**, 671–685. xiii, 18, 19, 20
- TRAMPERT, J., PAULSEN, H., VAN WETTUM, A., RITSEMA, J., CLAYTON, R., CASTRO, R., REBOLLAR, C. & PEREZ VERTITI, A. (2003). New array monitors seismic activity near the Gulf of California in Mexico. *EOS Trans AGU*, **84**, 29–32. 28
- TRIFUNAC, M.D. & TODORVSKA, M.I. (2001). A note on usable dynamic range of accelerographs recording translation. *Soil Dyn. Eng.*, **21**, 275–286. 4, 62
- ZADRO, M. & BRAITENBERG, C. (1999). Measurements and interpretations of tilt-strain gauges in seismically active area. *Earth-Science Review*, **47**, 151–187. 84
- ZERVA, A. & ZHANG, O. (1997). Correlation patterns in characteristics of spatially variable seismic ground motions. *Earthquake Eng. Struct. Dyn.*, **26**, 19–39. 1

Acknowledgments

During my enjoyable stay at Geophysik Institute Ludwig-Maximilians-Universität München, I have got the chance not only to learn the cutting-edgy sciences and technologies but also to know many out-standing researchers.

First of all, I would like to sincerely thank my advisors: Professor Heiner Igel for his support, guidance and tolerance during my Ph.D. study and also Prof. Dr. Ing-habil Ulrich Schreiber. Special thanks to Dr. Alain Cochard, who has been virtually my mentor for years on both analytic and non analytic issues. Dr. Joachim Wassermann shared with me his useful experience in array technique and signal processing. In Geophysik Sektion, I have made many friends and from them, I learned a lot. I would like to thank Erika Vye, Markus Treml and his Family, Toni Kraft, Tobias Metz, Falko Bethmann, Bernhard Schuberth, Haijiang Wang, Gilbert Brietzke, Michael Ewald and the entire seismology group. Special thanks to Markus Treml, Aryoko "Kossy" Prakoso, Susanne and "Nino" for making my *Zusammenfassung* readable.

I am very fortunate to have my wife, Ningsih Wijayanti at my side when I was fighting to survive here at Munich. She offered me support, encouragement and *Makan Enak*. Thanks for your patience and love. Our lovely children, Ramadhantika Fauziyyah, Haidar Pramudito and Ahmad Nur Aziz. I would also like to thank my parents and parents-in-law in Indonesia who have been helping and supporting me and my family in Indonesia.

Financial support of this work is provided by the IQN Georisk Project and Elite Netzwerk Bayern through THESIS Graduate College.

Lebenslauf

Persönliche Daten

Name Wiwit Suryanto
Anschrift Moosacherstr 81/225 München, 80809
Geburtsdatum 26 Januar 1974
Geburtsort Magelang, Indonesien
Familienstand verheiratet, 3 Kinder

Schulausbildung

1981-1986 Grundschule, Panca Arga Magelang
1986-1989 Grundschule, SMP N 2 Magelang
1989-1992 Gymnasium, SMA N 1 Magelang

Hochschulausbildung

1992-1998 Doktorandus (Geophysik), Universitas Gadjah Mada Yogyakarta
1999-2002 Master (Physik), Universitas Gadjah Mada Yogyakarta